

# CADS: A Comprehensive Anatomical Dataset and Segmentation for Whole-Body Anatomy in Computed Tomography

Murong Xu<sup>1,2,†,\*</sup>, Tamaz Amiranashvili<sup>1,7,†</sup>, Fernando Navarro<sup>1,†</sup>, Maksym Fritsak<sup>3,4</sup>, Ibrahim Ethem Hamamci<sup>1,2</sup>, Suprosanna Shit<sup>1,2</sup>, Bastian Wittmann<sup>1</sup>, Sezgin Er<sup>6</sup>, Sebastian M. Christ<sup>3</sup>, Ezequiel de la Rosa<sup>1</sup>, Julian Deseoe<sup>1,5</sup>, Robert Graf<sup>8,9</sup>, Hendrik Möller<sup>8,9</sup>, Anjany Sekuboyina<sup>1,8</sup>, Jan C. Peeken<sup>10,11,12</sup>, Sven Becker<sup>13,14</sup>, Giulia Baldini<sup>13,14</sup>, Johannes Haubold<sup>13,14</sup>, Felix Nensa<sup>13,14</sup>, René Hosch<sup>13,14</sup>, Nikhil Mirajkar<sup>18,19</sup>, Saad Khalid<sup>19</sup>, Stefan Zachow<sup>20</sup>, Marc-André Weber<sup>15</sup>, Georg Langs<sup>16</sup>, Jakob Wasserthal<sup>17</sup>, Mehmet Kemal Ozdemir<sup>6</sup>, Andrey Fedorov<sup>21</sup>, Ron Kikinis<sup>21</sup>, Stephanie Tanadini-Lang<sup>3</sup>, Jan S. Kirschke<sup>8</sup>, Stephanie E. Combs<sup>10,11,12</sup>, and Bjoern Menze<sup>1</sup>

<sup>1</sup> Department of Quantitative Biomedicine, University of Zurich, Zurich, Switzerland

<sup>2</sup> ETH AI Center, ETH Zurich, Zurich, Switzerland

<sup>3</sup> Department of Radiation Oncology, University Hospital and University of Zurich, Zurich, Switzerland

<sup>4</sup> Faculty of Medicine, University of Zurich, Zurich, Switzerland

<sup>5</sup> Department of Neurology and Clinical Neuroscience Center, University Hospital Zurich and University of Zurich, Zurich, Switzerland

<sup>6</sup> International School of Medicine, Istanbul Medipol University, Istanbul, Turkey

<sup>7</sup> School of Computation, Information and Technology, Technical University of Munich, Munich, Germany

<sup>8</sup> Department of Diagnostic and Interventional Neuroradiology, School of Medicine and Health, Technical University of Munich, Munich, Germany

<sup>9</sup> Institut für KI und Informatik in der Medizin, Klinikum rechts der Isar, TUM School of Medicine and Health and School of Computation, Information and Technology, Germany

<sup>10</sup> Department of Radiation Oncology, TUM University Hospital Rechts der Isar, TUM School of Medicine and Health, Technical University of Munich, Munich, Germany

<sup>11</sup> Institute of Radiation Medicine (IRM), Helmholtz Zentrum München (HMGU)

<sup>12</sup> German Consortium for Translational Cancer Research (DKTK), Partner Site Munich, Munich, Germany

<sup>13</sup> University Hospital Essen, Institute of Interventional and Diagnostic Radiology and Neuroradiology, Essen, Germany

<sup>14</sup> University Hospital Essen, Institute for Artificial Intelligence in Medicine, Essen, Germany

<sup>15</sup> Institute of Diagnostic and Interventional Radiology, Pediatric Radiology and Neuroradiology, University Medical Center Rostock, Rostock, Germany

<sup>16</sup> Department of Biomedical Imaging and Image-guided Therapy, Medical University of Vienna, Vienna, Austria

<sup>17</sup> Department of Radiology, University Hospital Basel, Basel, Switzerland

<sup>18</sup> Department of Radiology, Cambridge University Hospitals NHS Foundation Trust, Cambridge, UK

<sup>19</sup> Labelata GmbH, Zurich, Switzerland

<sup>20</sup> Visual and Data-Centric Computing, Zuse Institute Berlin (ZIB), Berlin, Germany

<sup>21</sup> Brigham and Women's Hospital, Boston, Massachusetts, USA

†These authors contributed equally to this work. \*Corresponding author: {murong.xu@uzh.ch}.

**Abstract.** Accurate delineation of anatomical structures in volumetric Computed Tomography (CT) scans is crucial for diagnosis and treatment planning. While AI has advanced automated segmentation, current approaches typically target individual structures, creating a fragmented landscape of incompatible models with varying performance and disparate evaluation protocols. Foundational segmentation models designed to process more organs address these limitations by providing a holistic anatomical view through a single model. Yet, robust clinical deployment demands comprehensive training data, which is lacking in existing whole-body approaches – both in terms of data heterogeneity and, more importantly, anatomical coverage. In this work, rather than pursuing incremental optimizations in model architecture, we present CADS, an open-source framework that prioritizes the systematic integration, standardization, and labeling of heterogeneous cross-institutional and cross-vendor data sources for whole-body CT segmentation. At its core is a large-scale dataset of 22,022 CT volumes with complete annotations for 167 anatomical structures, representing a significant advancement in both scale and coverage, with 18 times more scans than existing collections and 60% more distinct anatomical targets. Building on this diverse dataset, we develop the CADS-model using established architectures for accessible and automated full-body CT segmentation. Through comprehensive evaluation across 18 public datasets and an independent real-world hospital cohort, we demonstrate advantages over state-of-the-art approaches. Notably, thorough testing of the model's performance in segmentation tasks from radiation on-

cology validates its direct utility for clinical interventions. By making our large-scale dataset, our segmentation models, and our clinical software tool publicly available, we aim to advance robust AI solutions in radiology and make comprehensive anatomical analysis accessible to clinicians and researchers alike.

## Introduction

Computed Tomography (CT) provides detailed three-dimensional views of internal body structures, rendering it indispensable for various clinical applications from cancer diagnosis to emergency trauma assessment. The clinical adoption of CT has grown substantially over the past decade – in the European Union alone, annual examinations increased from 41.9 million in 2013 to 66.4 million in 2022 [1]. Despite this widespread utilization, the wealth of information within these CT scans remains largely under-explored.

Whole-body CT segmentation refers to the delineation of anatomical structures across the entire body and represents a crucial step toward fully leveraging imaging data. This analysis serves multiple clinical purposes: precise radiation planning in radiation oncology [2]; region-specific abnormality detection to support rapid diagnosis, triage, and mortality risk assessment [3]; automated localization of metastases [4]; body composition analysis through tissue quantification [5], and beyond. Furthermore, it can provide comprehensive anatomical context for specialized analysis tools targeting specific regions or organs, enhancing their performance. However, achieving accurate whole-body segmentation presents significant challenges, and has long been an active area of research in medical image processing. Early approaches based on atlas registration and statistical shape models [6,7,8,9] pioneered automated multi-organ segmentation, but struggled with registration errors and poor generalization at whole-body scale. Subsequent developments introduced learning-based techniques such as decision forests [10,11], which improved efficiency but still relied heavily on hand-crafted features. The establishment of benchmarks like VISCERAL [12] further highlighted the persistent challenges in large-scale annotation and cross-protocol evaluation.

Recent advances in artificial intelligence (AI) emerge as promising solutions for medical image analysis [13,14]. Early AI-based segmentation relied on training separate models for individual anatomical structures [15,16,17]. This approach faces three key limitations: (1) extensive manual annotation requirements for each structure; (2) inconsistent performance across models trained on different imaging protocols; and (3) complex post-processing needs to merge predictions for whole-body analysis. These limitations motivated the recent development of unified segmentation approaches, aiming at segmenting arbitrary structures in a zero-shot manner: interactive zero-shot segmentation [13,18,19] and in-context learning [20,21]. While both approaches provide test-time flexibility, in-context learning requires case-by-case user prompts, limiting large-scale clinical deployment, and in-context learning generally achieves lower accuracy than supervised learning. Consequently, efficient, high-quality, and fully-automated whole-body segmentation remains an unresolved challenge in clinical practice.

Recognizing that medical image segmentation typically involves a predetermined set of anatomical structures, recent efforts have shifted towards supervised whole-body foundational models. These models primarily adopt a data-centric approach, focusing on curating comprehensive training data rather than exploring novel architectures, annotating as many anatomical structures as possible. Evidence suggests that established frameworks like nnU-Net [22] are architecturally mature, with performance and generalization primarily limited by the scale, diversity, and quality of available training datasets. Unlike natural image datasets from RGB cameras that can contain millions of samples [23,24,25,26], medical datasets face two key limitations: they are orders of magnitude smaller and rarely annotated. Our analysis of 40 diverse sources reveals that only 21% of publicly available CT scans contain any annotations, with annotations typically confined to a single organ system (Table 1). Recent efforts such as TotalSegmentator [27] have pioneered large-scale whole-body segmentation and demonstrated the feasibility of AI-assisted dataset creation, enabling various architectural advances [28,29,30]. Yet current resources face several fundamental constraints that limit the performance ceiling of models trained on them.

These challenges include: *Limited anatomical coverage* – many approaches focus on specific regions or restricted structures, falling short of comprehensive whole-body analysis [31,32]; *Insufficient data diversity* – models developed on small-scale or single-source datasets show limited generalizability across institutions, populations, and imaging protocols [27,32,33,30,34]; *Inconsistent annotation quality* – existing automated labeling approaches introduce known systematic errors in complex anatomical structures like ribs and vertebrae [27], which models trained on such data learn and propagate; *Human-dependent workflows* – current approaches often rely on human-in-the-loop revisions during model training and dataset construction, limiting scalability and increasing operational costs [33,31]; *Inadequate validation* – evaluations are mostly conducted on internal or same-distribution datasets, with limited external testing, leaving real-world robustness unexplored [32,33,30,34]; *Limited availability* – some solutions remain

closed-source in models and deliverables, hindering reproducibility and wider adoption [32,30]; *Accessibility barriers* – the absence of user-friendly tools creates obstacles for healthcare practitioners without technical expertise, impeding the integration of AI solutions into clinical workflows.

To address these challenges, we present *CADS* (Figure 1), an open-source framework for whole-body CT segmentation. Our approach investigates how comprehensive, diverse training data impact segmentation performance when combined with well-established architectural frameworks. *CADS* therefore comprises two main components.

*CADS-dataset*: A large-scale collection of 22,022 CT volumes with full annotations for 167 anatomical structures, establishing the most extensive whole-body CT dataset to date and exceeding current state-of-the-art collections [27] in both scale (18 times more CT scans) and anatomical coverage (60% more distinct anatomical targets). Our automated annotation methodology is grounded in pseudo-labeling, allowing us to use images with no annotations, a single annotated structure, or multiple ones. We employ self-training through iterative model refinement, shape-guided quality control of segmentations, and fusion of the best-performing annotations from multiple segmentation approaches. This innovative pipeline aggregates diverse CT data from over 40 sources, including public archives (*e.g.*, TCIA [35] and medical challenges [36,37]), along with hospital cohorts. In addition to these sources, we contribute two new datasets: 484 newly acquired head CTs and 586 newly released triphasic contrast-enhanced abdominal CT scans, further enriching the collection. The collection spans more than 100 imaging facilities across 16 countries, capturing a wide spectrum of clinical variability.

*CADS-model*: A robust, fully automated segmentation model suite trained on the *CADS-dataset* and thoroughly validated, capable of segmenting 167 structures from head to knee across diverse anatomical systems. To our knowledge, this represents the most comprehensive open-source whole-body segmentation model to date, achieving enhanced performance compared to existing state-of-the-art methods through evaluation across 18 public datasets and an independent, unbiased real-world hospital cohort. Beyond quantitative metrics, expert radiation oncologists thoroughly evaluate and endorse the predicted segmentations as clinically reliable, validating their direct utility for precision therapeutic planning. Our systematic validation across diverse scanners, protocols, and pathologies confirms the effectiveness of our data-centric approach. Furthermore, to facilitate practical adoption, we provide our model as a user-friendly plugin within 3D Slicer [38]. This tool is designed for both clinicians and researchers, offering simple installation, one-click inference, and segmentation results presented according to the SNOMED-CT terminology standard [39], with full access to the trained models and source code.

By combining anatomical scope, data diversity, and modular design, *CADS* contributes to progress in whole-body CT segmentation. The comprehensive nature of *CADS* enables various research directions beyond segmentation. On the technical side, it can support anatomical landmark detection, cross-modality registration, and anatomy-guided synthesis. For clinical applications, it enables a wide range of uses including longitudinal organ tracking, personalized anatomical modeling, radiation treatment planning, and large-scale population studies. Through sharing our models<sup>1</sup>, data<sup>2</sup>, and the tool<sup>3</sup>, we aim to support the development of robust AI solutions in radiology and make comprehensive anatomical analysis accessible to both clinicians and researchers.

<sup>1</sup> <https://github.com/murong-xu/CADS>

<sup>2</sup> <https://huggingface.co/datasets/mrmrx/CADS-dataset>

<sup>3</sup> <https://github.com/murong-xu/SlicerCADS>

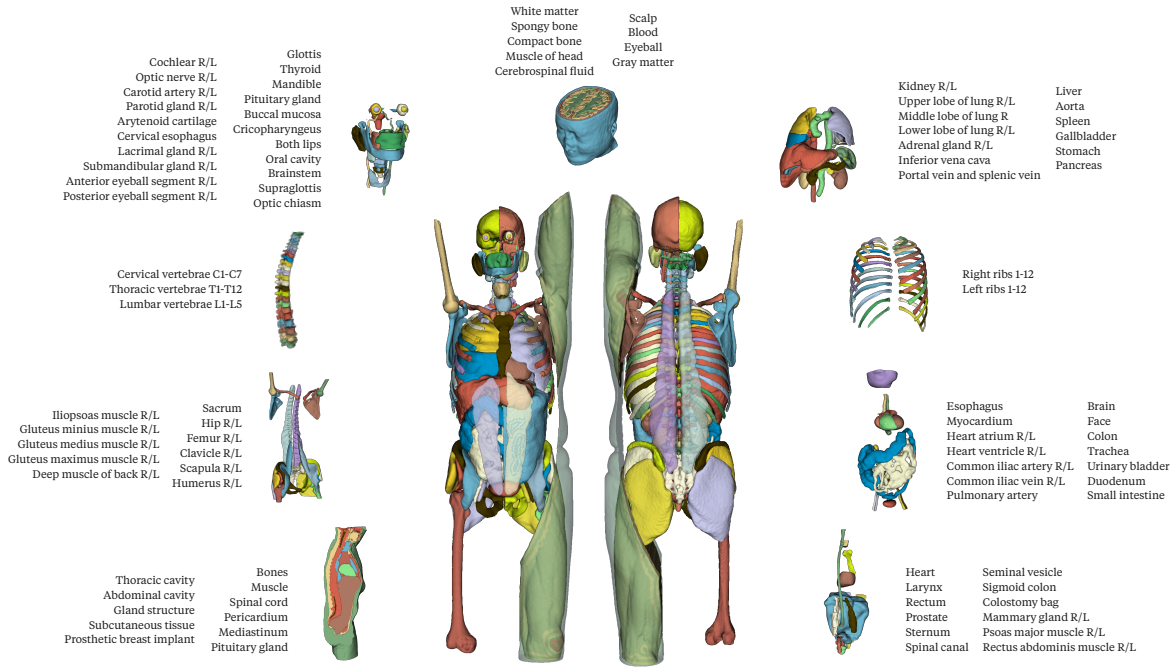


**Fig. 1: Overview of CADS framework's anatomical coverage.** Comprehensive visualization of 167 anatomical targets segmented by the CADS framework, spanning from head to knees. These clinically relevant structures are organized into nine anatomical groups: (1) major abdominal organs, primary thoracic organs (lungs), and major abdominal vasculature; (2) complete set of individual vertebrae from cervical to lumbar regions; (3) various thoracic and abdominal organs (including heart components, GI tract), brain, major pelvic vessels, and face; (4) major bones of the appendicular skeleton (upper/lower limbs, shoulder/pelvic girdles), sacrum, and associated large muscle groups; (5) complete set of individual ribs, both left and right; (6) miscellaneous structures including spinal canal, larynx, whole heart, specific lower GI/pelvic organs, mammary glands, sternum, and anterior abdominal wall muscles; (7) intracranial tissues and fluids, scalp, eyeball, general bone tissue classifications, and muscles of the head; (8) detailed head and neck anatomical structures, including specific arteries, cartilages, components of the aerodigestive tract, sensory organs (eye, ear), and various glands; and (9) general tissue types, major body cavities, broad anatomical categories (bones, glands as a whole), and specific structures like pericardium and spinal cord. This anatomically-driven organization guides the CADS-model's architectural design, with specialized models dedicated to each group to optimize segmentation performance.



## Results

In this section, we present an evaluation of our CADS framework: the CADS-dataset and the CADS-model. Our validation approach emphasizes clinical relevance through a multi-faceted assessment with three key features: (1) validation using expert-verified ground truth annotations, addressing the limitation that existing methods have often been evaluated solely on algorithm-generated labels that may contain errors; (2) testing across 18 diverse public datasets to evaluate generalization capabilities across varying imaging protocols and patient demographics; (3) real-world clinical performance assessment combining quantitative metrics with qualitative expert review by radiologists, focusing particularly on oncology cases – a critical application in clinical practice.

We evaluate model performance through three complementary analyses. The first one examines structure-level accuracy across all 167 anatomical targets (in Section ‘Anatomical precision across the body: Structure-level performance analysis’). The second analysis assesses adaptability across diverse dataset sources (in Section ‘Cross-dataset versatility: Dataset-level performance analysis’). The third one validates clinical utility using 2,864 oncology patients from University Hospital Zurich (in Section ‘From bench to bedside: CADS-model’s validation in real-world clinical settings’). This systematic evaluation provides evidence for the clinical viability of the CADS framework.

### CADS-dataset: A multi-source CT collection for comprehensive whole-body segmentation

The CADS-dataset aggregates 22,022 CT volumes from 40 diverse sources, representing one of the most comprehensive repositories for medical image analysis to date (Table 1). As the foundation of our CADS framework, this large-scale collection features voxel-level annotations covering 167 anatomical structures, serving dual purposes: enabling the development of the whole-body segmentation CADS-model and supporting further research in medical imaging. All annotations are publicly available in their original image formats.

Our data collection strategy systematically consolidates CT scans and annotations from three main sources: (1) large-scale public archives including TotalSegmentator [27] (1,203 annotated volumes with comprehensive coverage of 104 anatomical structures), which provides a foundational basis for whole-body segmentation, along with the National Lung Screening Trial (NLST [40], 7,172 scans), CT-RATE [41] (3,134 scans), and AbdomenCT-1K [42] (1,062 scans); (2) specialized annotation collections from medical imaging challenges (via Grand Challenge [36] and MICCAI [37]) and focused research studies (such as Han-Seg [43] for head-and-neck OARs, SAROS [44] for broad body context structures, and various oncology studies from TCIA [35]); and (3) newly contributed images and annotations, comprising manual annotations of critical OARs on the VISCERAL [12] dataset, 484 newly acquired anonymized head CTs, and 586 triphasic contrast-enhanced abdominal CT scans, which together strengthen coverage of cranial anatomy and multi-phase contrast imaging. This systematic integration unifies previously dispersed public datasets from medical imaging challenges and research initiatives, creating a unified resource that standardizes annotations while contributing new clinical data to the community.

The geographic diversity of the dataset spans 16 countries across multiple continents, integrating data from over 100 medical centers collected between 2007 and 2024. This broad representation captures varied clinical practices and patient populations, spanning both healthy subjects and various pathological conditions from oncological diseases (carcinomas, lymphomas, and metastases) to COVID-19, traumatic injuries, and rare disorders. The dataset includes varying imaging protocols (contrast-enhanced and non-contrast acquisitions) and covers multiple anatomical regions through different fields of view: whole-body, head-and-neck, chest, abdomen, pelvis, and spine.

Starting with a diverse collection of 22,022 CT volumes, where only 4,695 (21%) contain partial annotations from public sources, we develop a systematic approach to generate annotations for all 167 whole-body structures. Our annotation methodology (Figure 2, detailed explanations available in Online Methods) first standardizes the data by aligning all images to consistent orientation and 1.5 mm isotropic resolution. We then implement a multi-stage annotation process. First, we organize the 167 target structures into nine anatomical groups and develop specialized models for each group, leveraging high-quality annotations from established datasets. These specialized models then perform whole-body pseudo-labeling to propagate annotations across the remaining unlabeled scans (Figure 2, step 1) – leveraging each dataset’s strengths while addressing the impracticality of manual annotation at this scale. To ensure annotation quality, we implement two key safeguards: automated outlier detection of pseudo-labels in shape space using neural implicit functions [45,46] (step 2), and multi-strategy label generation through an ensemble selection mechanism that optimizes structure-specific segmentation strategies by combining complementary models trained with different data quality-quantity trade-offs (step 3). Detailed methodology in Online Methods Section.

To ensure clinical accuracy, we implement structure-specific quality controls and refinements. A representative example is our rib segmentation correction process, which accurately preserves the costovertebral joints, *i.e.*, anatomical details that are very commonly missing in public datasets. Rather than reproducing existing dataset conventions, these refinements ensure our annotations align with established anatomical standards for clinical validity. The resulting CADS-dataset captures real-world clinical variability across diverse settings, patient demographics, equipment specifications, and institutional protocols, providing a foundation for developing robust AI tools with consistent performance.

## CADS-model: Engineering AI for whole-body segmentation across 167 anatomical structures

The CADS-model provides whole-body segmentation coverage for 167 clinically important anatomical targets from head to knees (Figure 1). This approach enables unified segmentation across the entire body while maintaining generalization capabilities in different clinical settings.

Architecturally, we adopt the proven design principles of nnU-Net [22], implementing region-specific U-Nets [15] that optimize both computational efficiency and anatomical specialization. This configuration effectively manages memory constraints and preserves anatomical details during high-resolution whole-body processing, while supporting focused learning of region-specific patterns.

Existing whole-body segmentation approaches like [27] achieve full-body coverage by assembling separate models, each trained on distinct image sources for different anatomical systems. In contrast, our implementation builds all components upon a common foundation, *i.e.*, the 22,022-volume CADS-dataset with annotations from a systematic labeling pipeline (described in the ‘CADS-dataset: A multi-source CT collection for comprehensive whole-body segmentation’ section). This unified approach enables learning anatomical patterns from a shared, diverse data distribution across all 167 structures, naturally reducing sensitivity to dataset-specific characteristics while maintaining consistent development protocols throughout. To support practical deployment, we provide the CADS-model as a plugin tool in 3D Slicer [38] (Supplementary Figure A.6), offering an accessible, ready-to-use solution for practitioners.

## Anatomical precision across the body: Structure-level performance analysis

To evaluate the CADS-model’s capabilities, we conduct a detailed analysis across individual anatomical structures. We utilize 18 public datasets for evaluation (data partitioning details in Supplementary Table A.3), each providing ground truth annotations for specific target structures. By evaluating each structure across multiple independent sources, we assess the model’s ability to generalize across diverse imaging protocols and patient populations. Figure 3 presents a radar plot visualizing structure-wise Dice scores across all 167 anatomical structures compared to existing approaches. Scores increase radially from center (0, poorest) to periphery (1, optimal).

To isolate the impact of training data from architectural differences, we select TotalSegmentator [27] as our primary baseline, as it employs the same nnU-Net framework [22] and allows direct comparison of dataset contributions. This comparison is relevant as alternative whole-body segmentation algorithms, such as MONAI Label [28] and other recent approaches [29,30], have been intensively developed using the TotalSegmentator dataset. As our baseline model for multi-organ segmentation, we use TotalSegmentator’s latest version (v2.4.0) with the most robust parameter settings (more compute and longer processing time) to ensure fair comparison. For additional comparison, we include results from winning methods of organ-specific segmentation challenges (shown as plus symbols in the radar plot), using their originally reported performance metrics. These provide benchmarks from specialized models optimized for different segmentation tasks. For each structure, we calculate performance metrics exclusively on test samples with consistent anatomical definitions and ground truth annotations.

Results demonstrate the advantages of training on the larger, more diverse CADS-dataset over models limited to the TotalSegmentator dataset. For the 119 mutual targets, the CADS-model achieves a mean Dice score of 90.52% (95% CI: 88.12%-92.41%; median: 92.33%), while the baseline model with similar nnU-Net architecture trained on the limited dataset achieves 88.09% (95% CI: 85.18%-90.48%; median: 90.13%) (Figure 4a). Furthermore, training on the CADS-dataset results in improved performance in 71 structures, with 44 showing statistically significant improvements ( $p < 0.05$ ). On the other hand, challenge leaderboard results show performance fluctuations across anatomical structures, reflecting methods trained on single-source or limited datasets with different optimization focuses from earlier years. Training on the large-scale, diverse CADS-dataset demonstrates more consistent performance across the anatomical spectrum. This consistency indicates that multi-source training data effectively reduces performance variability compared to approaches using constrained datasets, highlighting the direct influence of dataset scale, diversity, and annotation quality on model performance.

Analysis across major anatomical systems further underscores the importance of training on the larger and more comprehensive CADS-dataset. For cardiovascular structures, we observe significant average Dice improvements in myocardium (+9.2%), pulmonary artery (+7.5%), and heart chambers (+5.3-8.3%). Skeletal structures demonstrate high precision in both sequential and individual elements: ribs achieve 89.6-97.2% with improvements in 22/24 structures (mean +2.9%), while vertebrae reach 85.8-92.7% with improvements in 17/24 structures. Individual bones show similar trends, with notable improvements in sacrum (+11.3%), sternum (+2.0%), and humerus (+3.3-4.9%). In traditionally challenging areas with low contrast or small size, we achieve substantial improvements for the brainstem (+23.7%) and optic nerves (+9.8-15.3%).

The CADS-model extends beyond these mutual targets to segment 48 additional structures (shown by green cross markers in Figure 3), including critical sensory organs, body cavities, and reproductive structures. Across all 167 target structures, the CADS-model achieves an overall Dice score of 85.87% – slightly lower than the mutual structures comparison due to three categories of challenges involved in segmenting the 48 new targets: (1) limited training data for certain structures (*e.g.*, buccal mucosa appears in less than 1,000 scans with only 30 ground-truth annotations, compared to well-represented structures in over 10,000 scans with several hundred ground-truth annotations, Supplementary Table A.5); (2) very small organs (volumes below 0.5 mL) where standard CT resolution limits and partial volume effects impact accuracy, such as the arytenoid cartilage; (3) anatomically complex structures, particularly small glands. These challenges identify directions for future refinement. Complete performance metrics beyond Dice scores are provided in Online Method Section 5.4.

Through systematic evaluation, the CADS-model trained on the CADS-dataset demonstrates consistent performance across diverse anatomical structures, with robust generalization across clinical settings. This validation confirms the effectiveness of our data-centric approach for practical clinical deployment.

## Cross-dataset versatility: Dataset-level performance analysis

We evaluate the CADS-model’s performance across individual data sources using heterogeneous test sets (Figure 4b). We use two primary metrics: Dice coefficient for volume overlap and 95% Hausdorff Distance (HD95) for boundary precision, while additional performance measures are detailed in Online Method Section 5.4.

Across the 18 test datasets, the CADS-model shows improved performance compared to baseline TotalSegmentator in most cases, achieving better Dice scores in 15 datasets and improved HD95 metrics in 16 datasets. On average, CADS-model demonstrates consistent improvements with 2.40% higher Dice scores and 3.94 mm lower HD95 values across all test datasets. Notable improvements in boundary precision are observed in anatomically complex regions, with substantial HD95 reductions in BTCV-Cervix (42.21 mm) and HaN-Seg (14.18 mm).

Our evaluation on the TotalSegmentator dataset, which provides reference annotations for 104 structures, reveals inaccuracies in these ground-truth labels across many structures, particularly evident in ribs and vertebrae segmentations (Figure 5a), with additional examples documented in Supplementary Figure A.7. This finding emphasizes the need to re-evaluate existing works that use the TotalSegmentator dataset, both to obtain accurate segmentation scores and to retrain models with corrected annotations, as their reported results may be affected by these annotation inconsistencies. To avoid these annotation quality concerns in the CADS-dataset, we create an expert-verified subset for more reliable benchmarking. On this curated test set, our model trained on the CADS-dataset achieves a Dice score of 93.15%, accurately delineating structures like costovertebral joints where original labels contained errors (Figure 5a). This improvement demonstrates how training data quality impacts model generalization.

For a more nuanced evaluation, we stratify our analysis into two cohorts: (1) a primary cohort with complete ground truth annotations across all structures, which are heavily involved in the model development process and represent an optimal benchmark for accuracy assessment under ideal conditions; and (2) a secondary cohort with incomplete or selective labels, reflecting real-world scenarios where annotations often cover only specific structures of interest. Training on CADS-dataset yields consistent improvements across both cohorts, with Dice score increases (primary: +2.29%, secondary: +2.11%, full dataset: +2.40%) and HD95 metric improvements (reductions of 2.42 mm, 3.10 mm, and 3.02 mm respectively). This consistent improvement across differently annotated datasets suggests enhanced adaptability to varying levels of ground truth completeness, which is particularly relevant for clinical deployment. These results support the proposition that comprehensive training datasets enhance model generalization capabilities across clinical environments.

## From bench to bedside: CADS-model’s validation in real-world clinical settings

While automated segmentation shows promise on curated public datasets, its clinical value ultimately depends on performance with pathological cases commonly encountered in daily hospital practice. To assess real-world utility, we evaluate our model on 2,864 subjects from the Radiation Oncology Department at University Hospital Zurich, representing an independent cohort with unknown data distribution. This cohort spans 35 anatomical structures with diverse pathological conditions including kidney and liver tumors, lung cancer, and other malignancies, representing the typical challenges that deployed AI systems face in clinical practice. Detailed characteristics of this evaluation cohort are provided in Online Method Section 5.3.

Performance comparison in this real-world setting (Figure 4c, visualized as a bubble chart where bubble size reflects Dice score differences) shows that training on the CADS-dataset yields improved results across most structures. Notably significant improvements appear in regions critical for radiation therapy planning: brainstem (+43.8%), larynx (+23.08%), and parotid glands (left: +19.40%, right: +21.02%). The accurate delineation of these structures directly impacts radiation dose planning and patient outcomes.

To evaluate clinical relevance beyond quantitative metrics, we conduct a systematic expert review led by an experienced radiation oncologist (5.5 years in practice). For each structure, the expert assessed three representative cases around the median Dice score – one at median level and two at adjacent performance levels – ensuring unbiased evaluation. The detailed review feedback is presented in Figure 5. Expert assessment confirms that segmentations from the CADS-model meet clinical standards for anatomical structure delineation in radiation therapy planning across most structures (Figure 5b, lower part). Clinical acceptability was determined through a systematic, slice-by-slice review of the 3D segmentation masks by a clinical radiation oncologist. Each contour was evaluated for geometric accuracy, anatomical completeness, and adherence to the consensus organ-at-risk delineation practices as described in [47]. The model demonstrates particular strength in traditionally challenging regions like the parotid deep lobe, mandible, and complex lung areas (Figure 5b, upper part). While some areas present opportunities for improvement, such as brain mask definition and vessel delineation (Figure 5c), these limitations do not compromise the overall clinical utility. The segmentations remain suitable for radiation therapy planning, with applicability varying based on specific treatment requirements and tumor proximity to regions of interest.

Validated through both quantitative metrics and expert visual assessment, the results demonstrate the clinical viability of our data-centric approach for radiation therapy planning. The overall performance of both AI models indicates that machine learning-based medical image segmentation has matured toward reliable clinical solutions, with comprehensive, high-quality datasets playing an increasingly important role alongside architectural advances.

Various platforms and tools, including 3D Slicer [38], OHIF [48], and MONAI Label [28], have introduced user-friendly interfaces enabling clinicians to leverage AI algorithms with minimal technical expertise. To facilitate accessibility, we release a 3D Slicer plugin that implements the CADS-model trained on CADS-dataset (Supplementary Figure A.6), supporting clinical adoption and research applications. This plugin provides access to comprehensive whole-body segmentation capabilities within a familiar interface used by many healthcare practitioners, supporting the integration of AI solutions into clinical workflows.

## Discussion

The field of AI-based whole-body CT analysis has reached a pivotal juncture where technical advancements increasingly align with clinical needs. However, progress in whole-body segmentation remains hindered by fragmented data, limited anatomical coverage, and insufficient clinical validation. The key barrier is the lack of comprehensive anatomically annotated datasets, which impedes the development of robust, clinically viable segmentation models.

The CADS framework addresses these challenges through an extensive data-centric approach. Rather than pursuing incremental optimizations in model architecture, we prioritize the systematic integration, standardization, and labeling of heterogeneous data sources. The resulting CADS-dataset comprises 22,022 CT volumes annotated across 167 structures (Figure 1), with diversity spanning continents, protocols, and pathologies. This comprehensive dataset provides a foundation for developing models with robust cross-institutional generalization. Using the well-established nnU-Net architecture, we demonstrate that training on this extensive dataset yields substantial performance improvements over models constrained by limited data or interactive approaches that create deployment bottlenecks. Through our open-source



3D Slicer plugin (Supplementary Figure A.6), we make these capabilities accessible to clinicians in familiar environments, while SNOMED-CT terminology integration ensures seamless incorporation into existing healthcare infrastructures.

Our validation extends beyond conventional metrics to include clinical insights. Through expert medical review, we identify and correct significant label quality issues in existing widely-used public datasets, particularly evident in complex structures like ribs and vertebrae where anatomical boundaries are challenging to delineate, highlighting potential risks of error propagation in models trained or evaluated on such data. Comprehensive evaluation across public challenges and real-world hospital data, validated through both quantitative metrics and independent radiologist assessment (Figure 3, 4 and 5), confirms the clinical viability of our data-centric approach.

Importantly, CADS should be viewed not as competing with recent algorithmic innovations, but as a synergistic foundation to enhance their impact. Many state-of-the-art models [49,50,51,52] have been developed or evaluated on datasets with the limitations identified in our analysis, constraining their performance potential. The CADS-dataset offers an immediate opportunity to unlock their full potential through training on comprehensive, high-quality data.

Our large-scale automated annotation approach aims to balance the inherent trade-off between precision and scalability. Its primary advantage lies in mitigating variance-driven errors, which are prevalent and often dominant in pseudo-labeling and label propagation settings with limited labeled data [53,54]. In particular, our pseudo-labeling pipeline enables wide coverage of anatomical variability. Common sources of variance error, such as boundary ambiguity, protocol heterogeneity, and inter-annotator inconsistency, can be effectively reduced through integration of multi-source data, large-scale model training, and our ensemble selection mechanism that optimizes structure-specific segmentation strategies [55]. This variance reduction aligns with central limit theorem principles, wherein aggregation across diverse instances leads to more stable and reliable predictions [56]. Similarly designed to alleviate such variance errors, our shape-based outlier detection identifies and removes random or abnormal segmentations from the training process. The consistent improvements across 18 different test datasets (Figure 4) demonstrate benefits of this variance-reduction approach. Beyond addressing these statistical variations, we also tackle systematic bias errors through targeted anatomical refinements, such as the costovertebral joint retrieval process that improves systematic omissions in existing datasets.

Despite these methodological advantages and our framework’s capabilities, we identify several directions for future research and development. (1) A primary limitation of our approach concerns the exclusion strategy in our shape-based quality assessment. By directly excluding segmentations identified as low-quality from the training process, we potentially eliminate cases involving pathological conditions that present atypical anatomical variations. This exclusion may limit the model’s ability to learn clinically important edge scenarios. While manual correction of these challenging cases would represent the optimal solution for maintaining annotation quality, such intervention becomes prohibitively resource-intensive at our dataset scale of 22,022 volumes. Hence, our current strategy of automated exclusion rather than correction represents a necessary trade-off between dataset scale and annotation precision. Future work should explore hybrid quality control frameworks that integrate automated filtering with targeted manual intervention, aiming to preserve scalability while recovering valuable but difficult training instances. (2) While CADS spans from head to knees, future work can extend to additional regions (*e.g.*, hands, feet) and achieve finer segmentation of anatomical substructures, particularly within the central nervous, musculoskeletal, and vascular systems, where vascular structures are often absent in current datasets due to annotation complexity. (3) Several regions require refinement: the brain mask currently includes all central nervous components within the skull, which may be too inclusive for certain applications; the optic chiasm tends to be under-segmented; the heart segmentation omits superior portions; and the rectum appears shorter than its anatomical extent. Structures like the trachea (currently limited to air content without surrounding tracheal wall) and vena cava need more precise delineation. (4) Due to privacy considerations, facial features are intentionally anonymized, limiting applications requiring detailed facial analysis. Such applications would need complementary datasets or hybrid approaches. (5) Our modular design with specialized models balances efficiency and coverage, but future research could explore unified architectures handling all structures simultaneously. (6) The rich anatomical hierarchies in CADS annotations can enable the development of novel context-aware segmentation strategies leveraging organ positional relationships. (7) While our current focus has been on segmentation, the CADS-dataset creates opportunities for broader medical image analysis: anatomical landmark detection for automated measurements, cross-modality registration for CT-MRI fusion and PET-CT alignment, and anatomy-guided image reconstruction for radiation dose reduction, and beyond.

By sharing the entire CADS framework publicly with its CADS-dataset, CADS-model, and ready-to-use tools, we aim to accelerate innovation and promote AI adoption in medical image analysis. CADS’ clinical potential spans multiple domains: in radiation oncology, it can streamline treatment planning through rapid organ delineation; in diagnostic radiology, it can enable automated organ volume quantifi-

cation and detection of subtle anatomical changes; and for research applications, it can facilitate large-scale studies across diverse populations and conditions. The CADS framework thus serves as a bridge between technical capabilities and clinical applications, contributing to the development of AI-integrated healthcare workflows.



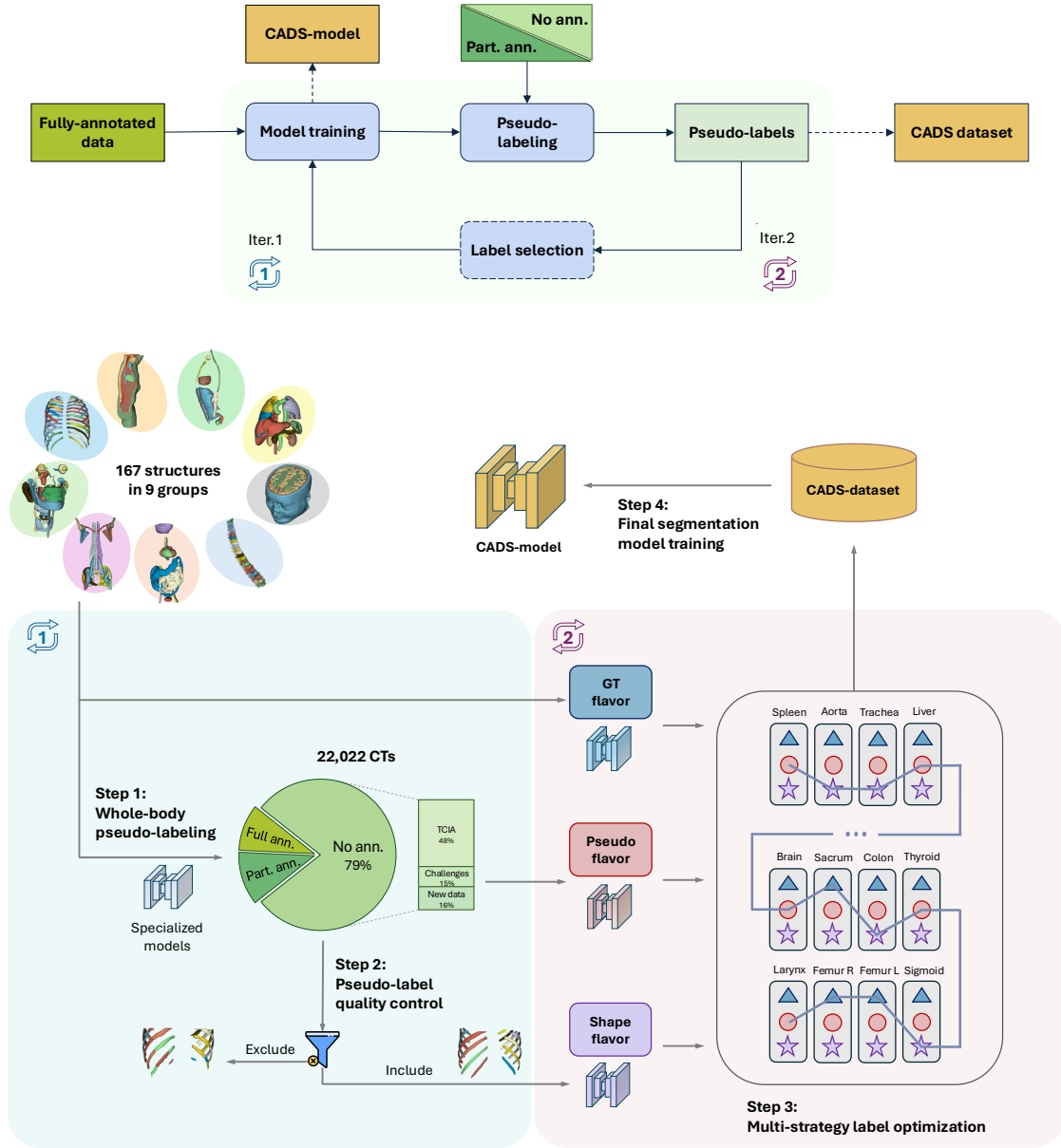
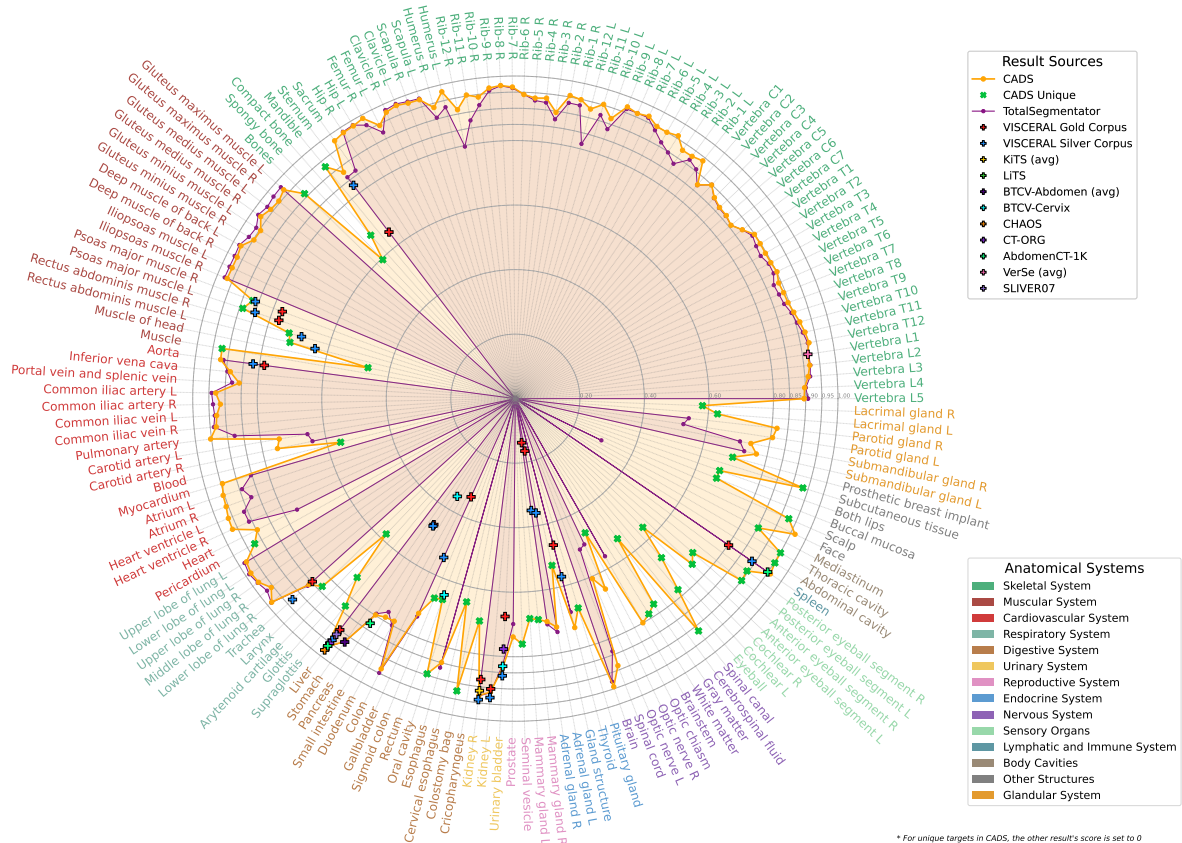


Fig. 2: **Overview of the multi-stage development process for whole-body CT segmentation CADS-model.** The pipeline consists of four key stages: (1) initial region-specific model training and pseudo-label generation across 22,022 CT volumes, utilizing specialized models for nine anatomical regions covering all 167 target structures; (2) automated quality control employing neural implicit functions and shape priors to filter unreliable pseudo-labels; (3) multi-strategy label generation through an ensemble selection mechanism that optimizes structure-specific segmentation by combining three complementary models ("flavors") trained with varying data characteristics to create the assembled CADS-dataset; and (4) final CADS-model training with customized class balancing strategies. This data-centric approach enables efficient processing of region-specific anatomical patterns while maintaining consistent labeling conventions across the entire framework.



**Fig. 3: Structure-level performance analysis.** Visualization of segmentation performance across 167 anatomical structures grouped by anatomical systems. The radar plot presents Dice scores (increasing radially from 0 at center to 1 at periphery) for the CADS-model compared against existing approaches, evaluated on diverse validation sets from 18 public datasets. Performance is shown for CADS-model (orange), TotalSegmentator (purple), and challenge-winning methods (plus symbols) where available. Challenge results marked with (avg) represent composite scores across multiple structures. Green cross markers indicate 48 additional structures uniquely segmented by the CADS-model, extending beyond existing capabilities. This results demonstrates the CADS-model's comprehensive coverage and robust performance across the full range of anatomical targets, while highlighting its expanded capabilities in previously unsupported regions.



**Fig. 4: Clinical evaluation of CADS-model performance.** Multi-faceted analysis of segmentation performance across different validation scenarios: (a) Comparison between CADS-model and baseline model TotalSegmentator on mutual anatomical targets, evaluated across primary (complete annotations) and secondary (partial annotations) test cohorts. Additional analysis presents the CADS-model’s performance across its full range of 167 structures, including unique targets not covered by existing methods. (b) Dataset-specific performance analysis across 18 test sources, demonstrating the CADS-model’s consistent superiority in both volumetric accuracy (Dice) and boundary precision (HD95) across diverse data sources with varying annotation styles and imaging protocols. (c) Clinical validation using a large real-world hospital cohort of oncology patients, visualized through a bubble chart. Results demonstrate significant improvements in structures critical for radiation therapy planning, validating the model’s effectiveness in real-world clinical scenarios.

Data Source	#Vols	# Ann. Vols	# Ann. Struct.	Body Reg.	Ann. Method	#Cent.	Countries	Contrast	Pathology	License
VISCERAL Gold Corpus [12]	40	40	20	WB, VR	Human	3	AT, DE, ES	Mix	Pathologic: Bone Marrow Neoplasm, Lymphoma	-
VISCERAL Gold Corpus-Extra	-	40	22	WB, VR	Human	3	AT, DE, ES	Mix	Pathologic: Bone Marrow Neoplasm, Lymphoma	-
VISCERAL Silver Corpus	127	127	20	WB, VR	Algorithm/	3	AT, DE, ES	Mix	Pathologic: Bone Marrow Neoplasm, Lymphoma	-
KiTS [57]	300	300	1	AB	Human	1	US	Contrast-enhanced	Pathologic: Kidney Tumor	CC BY-NC-SA 4.0
LiTS [58]	201	201	1	AB	Human	7	DE, NL, CA, IL, FR	Contrast-enhanced	Pathologic: Liver Tumor (Primary & Metastasis)	CC BY-NC-SA 4.0
BTCV-Abdomen [59]	50	30	13	AB	Human	1	US	Contrast-enhanced	Pathologic: Colorectal Cancer, Hernia	CC BY 4.0
BTCV-Cervix	50	30	3	PR	Human	1	NL	-	Pathologic: Cervical Cancer	CC BY 4.0
CHAOS [60]	40	20	1	AB	Human	1	TR	Contrast-enhanced	Healthy	CC BY-NC-SA 4.0
AbdomenCT-1K [42]	1,062	1,000	4	AB	Hybrid	12	DE, NL, CA, FR, IL, US, CN	Mix	Pathologic: Liver, Pancreas, Kidney, Colon	Mixed: CC BY 4.0, CC BY-NC-SA 4.0, CC BY-SA 4.0
VerSe [61]	374	374	22	SP	Hybrid	-	-	-	Pathologic: Spine (Fracture, Implants, Foreign Material)	CC BY-SA 4.0
EXACT09 [62]	40	-	-	CH	-	8	-	Mix	Mixed: Lung Disease (Healthy to Severe Pathologies)	Restricted (team use only; redistribution prohibited)
CAD-PE [63]	40	-	-	CH	-	6	ES	Contrast-enhanced	Pathologic: Pulmonary Embolism	CC BY 4.0
RibFrac [64]	660	-	-	CH, AB	-	1	CN	-	Pathologic: Rib Fractures	CC BY-NC 4.0
Learn2reg [65]	16	8	4	AB	Human	-	-	-	-	Mixed: TCIA + CC BY 3.0
LNDb [66]	294	-	-	CH	-	1	PT	-	Pathologic: Lung Nodules (Screening)	CC BY 4.0
LOLA11 [67]	55	-	-	CH	-	-	-	-	Pathologic: Multiple Serious Abnormalities	Restricted (challenge use only; no training, no redistribution)
SLIVER07 [68]	30	20	1	CH	Human	Various	-	Contrast-enhanced	Pathologic: Multiple Tumors, Cysts, Metastases	Restricted (liver segmentation only; requires explicit permission)
STOIC2021 [69]	2,000	-	-	CH	-	20	FR	Mix	Pathologic: COVID-19 Suspected	CC BY-NC 4.0
CT-RATE [41]	3,134	-	-	CH	-	1	TR	-	-	-
EMPIRE10 [70]	60	60	1	CH	Hybrid	Various	NL, BE	-	Mixed: Lung Disease or Healthy	Restricted (challenge use only; no training, no redistribution)
AMOS [71]	200	200	15	AB	Hybrid	2	CN	Mix	Pathologic: Abdominal Tumors (Healthy Excluded)	CC BY 4.0
HaN-Seg [43]	42	42	30	HN	Human	1	SI	-	-	CC BY-NC-ND 4.0
HaN-Seg Extra Brain Labels	-	42	9	HN	Algorithm/	1	SI	-	-	CC BY-NC-ND 4.0
CT-ORG [72]	140	140	5	WB, AB	Hybrid	8	DE, NL, CA, IL, FR, US	Mix	Mixed: Liver Lesions (Benign & Malignant), Bone & Lung Metastasis	CC BY 3.0
LIDC-IDRI [73]	997	-	-	CH	-	7	-	-	Pathologic: Lung Nodules (Benign or Malignant)	CC BY 3.0
CT Lymph Nodes [74]	174	-	-	CH, AB	-	Various	-	-	Pathologic: Lymphadenopathy (Non-cancer), Abdomen, Mediastinum	CC BY 3.0
CPTAC-CCRCC [75]	258	-	-	CH, AB	-	-	-	-	Pathologic: Kidney Clear Cell Carcinoma	CC BY 3.0
CPTAC-LUAD [76]	133	-	-	CH, AB	-	-	-	Mix	Pathologic: Lung Adenocarcinoma	CC BY 3.0
CT Images in COVID-19 [77]	121	-	-	CH	-	4	CN, JP, IT	-	Pathologic: COVID-19 Pneumonia	CC BY 4.0
NSCLC Radiogenomics [78]	131	-	-	CH	-	2	US	-	Pathologic: NSCLC (Non-Small Cell Lung Cancer)	CC BY 3.0
Pancreas-CT [79]	80	-	-	AB	-	1	US	Contrast-enhanced	Healthy	CC BY 3.0
Pancreatic-CT-CBCT-SEG [80]	93	-	-	CH, AB	-	1	US	Mix	Pathologic: Pancreatic Cancer	CC BY 4.0
RIDER Lung CT [81]	59	-	-	CH	-	1	US	Non-contrast	Pathologic: NSCLC, Pulmonary Metastases	CC BY 4.0
TCGA-KICH [82]	17	-	-	AB	-	-	-	-	Pathologic: Kidney Chromophobe Carcinoma	CC BY 3.0
TCGA-KIRC [83]	398	-	-	AB	-	-	-	-	Pathologic: Kidney Renal Clear Cell Carcinoma	CC BY 3.0
TCGA-KIRP [84]	19	-	-	AB	-	-	-	-	Pathologic: Kidney Papillary Cell Carcinoma	CC BY 3.0
TCGA-LIHC [85]	242	-	-	AB	-	-	-	-	Pathologic: Liver Hepatocellular Carcinoma (HCC)	CC BY 3.0
National Lung Screening Trial (NLST) [40]	7,172	-	-	CH	-	33	US	Non-contrast	-	CC BY 4.0
Total-Segmentator [27]	1,203	1,203	104	VR	Hybrid	8	CH	Contrast-enhanced	Mixed: 645 Pathologic (Tumor, Trauma, etc), 404 Healthy	CC BY 4.0
SAROS [44]	900	900	11	WB, VR	Hybrid	Various	-	-	-	Mixed: CC BY 3.0, CC BY 4.0, CC BY-NC 3.0, TCIA (restricted access)
New Hospital Data - CT-TRI [86]	586	-	-	AB	-	1	DE	Mix	Pathologic: Liver and Kidney Cancer	CC-BY-SA-NC
New Hospital Data - Head	484	-	-	HN	-	1	TR	-	-	-
<b>Total</b>	<b>22,022</b>	<b>4,695</b>	<b>167</b>	<b>-</b>	<b>-</b>	<b>&gt; 100</b>	<b>16</b>	<b>Mix</b>	<b>Normal and pathologic</b>	<b>-</b>

**Table 1: Summary of CT collection in CADS-dataset.** Overview of 22,022 CT volumes that form the foundation of the CADS-dataset and enable the development of the CADS-model. Each dataset entry details volume counts, number of annotated volumes, annotated anatomical structures, image body regions (WB: Whole Body, HN: Head and Neck, CH: Chest, AB: Abdomen, PR: Pelvic Region, SP: Spine, VR: Various Regions), annotation methodology, number of acquisition centers, geographical origin (Austria (AT), Belgium (BE), Canada (CA), Switzerland (CH), China (CN), Germany (DE), Spain (ES), France (FR), Israel (IL), Italy (IT), Japan (JP), Netherlands (NL), Portugal (PT), Slovenia (SI), Turkey (TR), and United States (US)), contrast enhancement status, pathological conditions, and licensing information. The collection, organized into four major categories as shown in the table, spans 40 diverse sources across 16 countries: 1) public challenge datasets from *e.g.*, Grand Challenges [36], 2) research collections from The Cancer Imaging Archive (TCIA [35]), 3) whole-body datasets providing large anatomical coverage, and 4) newly acquired abdominal and head images from our clinical collaborators. Of these, 4,695 volumes (approximately 21% of the collection) contain partial manual or hybrid annotations. Through systematic curation and annotation processes, this collection ultimately enables the segmentation of 167 anatomical structures by the CADS-model. This heterogeneous collection, encompassing both normal and pathological cases across various imaging protocols and patient demographics, serves as the cornerstone for developing robust, generalizable AI-powered anatomical segmentation capabilities.

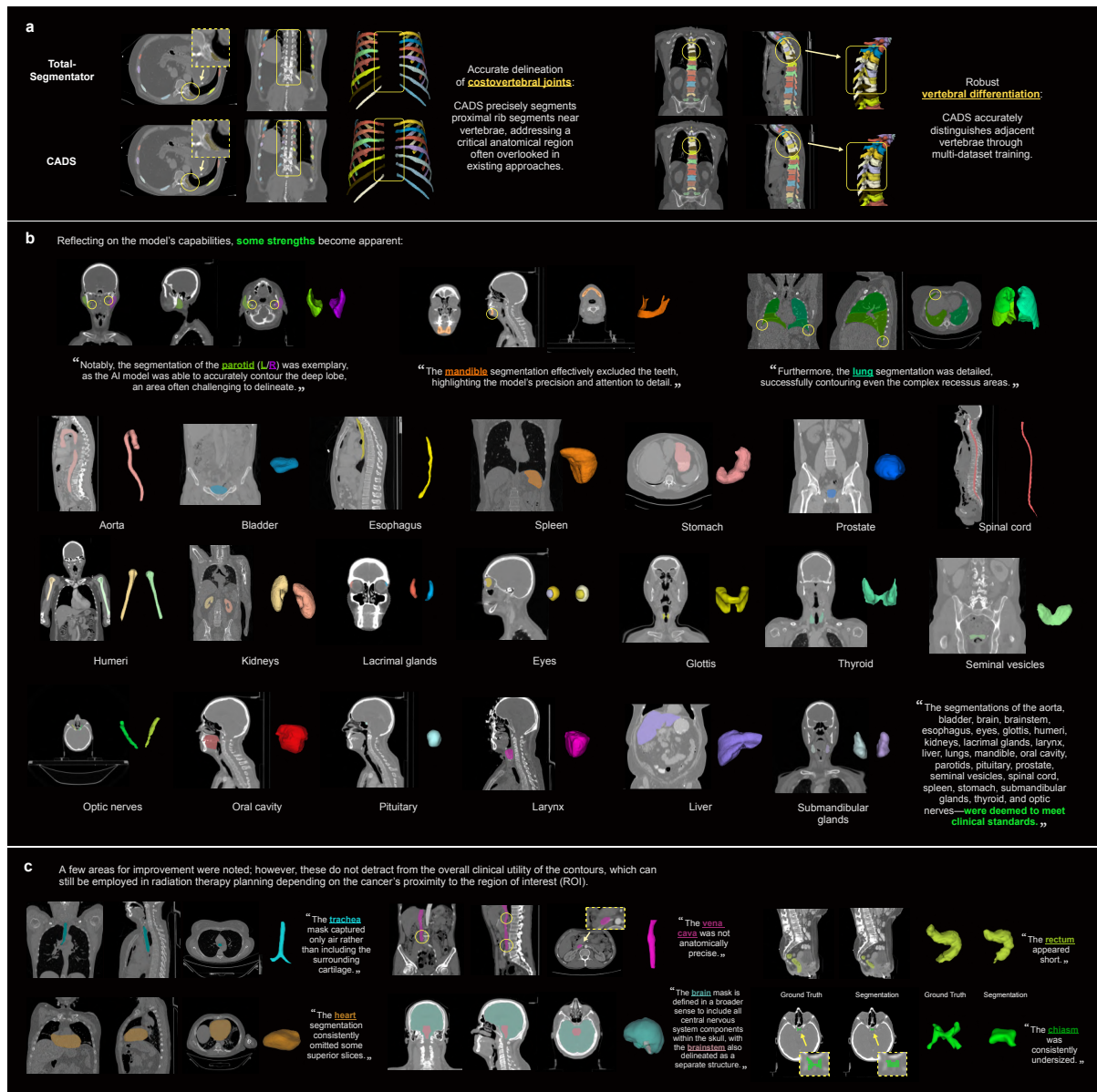


**Fig. 5: Qualitative assessment of CADS-model segmentation performance.** Visual evaluation of segmentation results across three key aspects: (a) Comparison of skeletal structure segmentation between existing methods and CADS-model, demonstrating significant improvements aligned with standard medical definitions. Notable advancements include anatomically accurate delineation of costovertebral joints and precise differentiation of adjacent vertebrae, addressing common limitations in current approaches while adhering to established anatomical conventions. (b) Radiologist-reviewed examples of successful segmentations from unseen clinical data (with expert feedback shown as adjacent text), demonstrating the CADS-model's proficiency in anatomically complex regions. Cases were selected around median performance levels to ensure representative sampling of a large-scale clinical cohort. Visualizations showcase accurate delineation of challenging structures such as the parotid deep lobe, mandible, and intricate lung areas, while other anatomical targets meet clinical standards. (c) Areas identified for potential refinement, with corresponding radiologist feedback shown alongside. While specific improvement opportunities were noted in certain structures, these limitations do not compromise the model's clinical utility, particularly for radiation therapy planning where segmentation requirements vary by treatment context.



## References

1. Eurostat, “Medical technologies - examinations by medical imaging techniques (CT, MRI and PET).” [https://ec.europa.eu/eurostat/databrowser/view/hlth\\_co\\_exam/default/table?lang=en](https://ec.europa.eu/eurostat/databrowser/view/hlth_co_exam/default/table?lang=en), 2024. Last updated: 2024-09-03.
2. F. Shi, W. Hu, J. Wu, M. Han, J. Wang, W. Zhang, Q. Zhou, J. Zhou, Y. Wei, Y. Shao, *et al.*, “Deep learning empowered volume delineation of whole-body organs-at-risk for accelerated radiotherapy,” *Nature communications*, vol. 13, no. 1, p. 6566, 2022.
3. S. Eyuboglu, G. Angus, B. N. Patel, A. Pareek, G. Davidzon, J. Long, J. Dunnmon, and M. P. Lungren, “Multi-task weak supervision enables anatomically-resolved abnormality detection in whole-body FDG-PET/CT,” *Nature communications*, vol. 12, no. 1, p. 1880, 2021.
4. T. P. Vagenas, T. L. Economopoulos, C. Sachpekidis, A. Dimitrakopoulou-Strauss, L. Pan, A. Provata, and G. K. Matsopoulos, “A decision support system for the identification of metastases of metastatic melanoma using whole-body FDG PET/CT images,” *IEEE Journal of Biomedical and Health Informatics*, vol. 27, no. 3, pp. 1397–1408, 2022.
5. A. D. Weston, P. Korfiatis, T. L. Kline, K. A. Philbrick, P. Kostandy, T. Sakinis, M. Sugimoto, N. Takahashi, and B. J. Erickson, “Automated abdominal segmentation of CT scans for body composition analysis using deep learning,” *Radiology*, vol. 290, no. 3, pp. 669–679, 2019.
6. I. Isgum, M. Staring, A. Rutten, M. Prokop, M. A. Viergever, and B. Van Ginneken, “Multi-atlas-based segmentation with local decision fusion—application to cardiac and aortic segmentation in CT scans,” *IEEE transactions on medical imaging*, vol. 28, no. 7, pp. 1000–1010, 2009.
7. P. P. Rebouças Filho, P. C. Cortez, A. C. da Silva Barros, V. H. C. Albuquerque, and J. M. R. Tavares, “Novel and powerful 3d adaptive crisp active contour method applied in the segmentation of CT lung images,” *Medical image analysis*, vol. 35, pp. 503–516, 2017.
8. M. De Bruijne, B. Van Ginneken, W. J. Niessen, M. Loog, and M. A. Viergever, “Model-based segmentation of abdominal aortic aneurysms in CTA images,” in *Medical imaging 2003: Image processing*, vol. 5032, pp. 1560–1571, SPIE, 2003.
9. R. Wolz, C. Chu, K. Misawa, M. Fujiwara, K. Mori, and D. Rueckert, “Automated abdominal multi-organ segmentation with subject-specific atlas generation,” *IEEE transactions on medical imaging*, vol. 32, no. 9, pp. 1723–1730, 2013.
10. A. Criminisi, J. Shotton, D. Robertson, and E. Konukoglu, “Regression forests for efficient anatomy detection and localization in CT studies,” in *Medical Computer Vision. Recognition Techniques and Applications in Medical Imaging* (B. Menze, G. Langs, Z. Tu, and A. Criminisi, eds.), (Berlin, Heidelberg), pp. 106–117, Springer Berlin Heidelberg, 2011.
11. A. Montillo, J. Shotton, J. Winn, J. E. Iglesias, D. Metaxas, and A. Criminisi, “Entangled decision forests and their application for semantic segmentation of CT images,” in *Information Processing in Medical Imaging: 22nd International Conference, IPMI 2011, Kloster Irsee, Germany, July 3-8, 2011. Proceedings 22*, pp. 184–196, Springer, 2011.
12. O. Jimenez-del Toro, H. Müller, M. Krenn, K. Gruenberg, A. A. Taha, M. Winterstein, I. Eggel, A. Foncubierta-Rodríguez, O. Goksel, A. Jakab, *et al.*, “Cloud-based evaluation of anatomical structure segmentation and landmark detection algorithms: Visceral anatomy benchmarks,” *IEEE transactions on medical imaging*, vol. 35, no. 11, pp. 2459–2475, 2016.
13. J. Ma, Y. He, F. Li, L. Han, C. You, and B. Wang, “Segment anything in medical images,” *Nature Communications*, vol. 15, no. 1, p. 654, 2024.
14. J. Wu and M. Xu, “One-prompt to segment all medical images,” in *Proceedings of the IEEE/CVF Conference on Computer Vision and Pattern Recognition*, pp. 11302–11312, 2024.
15. O. Ronneberger, P. Fischer, and T. Brox, “U-net: Convolutional networks for biomedical image segmentation,” in *Medical image computing and computer-assisted intervention—MICCAI 2015: 18th international conference, Munich, Germany, October 5-9, 2015, proceedings, part III 18*, pp. 234–241, Springer, 2015.
16. F. Milletari, N. Navab, and S.-A. Ahmadi, “V-net: Fully convolutional neural networks for volumetric medical image segmentation,” in *2016 fourth international conference on 3D vision (3DV)*, pp. 565–571, Ieee, 2016.
17. H. R. Roth, L. Lu, A. Farag, H.-C. Shin, J. Liu, E. B. Turkbey, and R. M. Summers, “Deeporgan: Multi-level deep convolutional networks for automated pancreas segmentation,” in *Medical Image Computing and Computer-Assisted Intervention—MICCAI 2015: 18th International Conference, Munich, Germany, October 5-9, 2015, Proceedings, Part I 18*, pp. 556–564, Springer, 2015.
18. H. E. Wong, M. Rakic, J. Guttag, and A. V. Dalca, “Scribbleprompt: fast and flexible interactive segmentation for any biomedical image,” in *European Conference on Computer Vision*, pp. 207–229, Springer, 2024.
19. Y. He, P. Guo, Y. Tang, A. Myronenko, V. Nath, Z. Xu, D. Yang, C. Zhao, B. Simon, M. Belue, *et al.*, “Vista3d: Versatile imaging segmentation and annotation model for 3D computed tomography,” *arXiv preprint arXiv:2406.05285*, 2024.
20. V. I. Butoi, J. J. G. Ortiz, T. Ma, M. R. Sabuncu, J. Guttag, and A. V. Dalca, “Universeg: Universal medical image segmentation,” in *Proceedings of the IEEE/CVF International Conference on Computer Vision*, pp. 21438–21451, 2023.
21. S. Ren, X. Huang, X. Li, J. Xiao, J. Mei, Z. Wang, A. Yuille, and Y. Zhou, “Medical vision generalist: Unifying medical imaging tasks in context,” *arXiv preprint arXiv:2406.05565*, 2024.
22. F. Isensee, P. F. Jaeger, S. A. Kohl, J. Petersen, and K. H. Maier-Hein, “nnu-net: a self-configuring method for deep learning-based biomedical image segmentation,” *Nature methods*, vol. 18, no. 2, pp. 203–211, 2021.



23. A. Dosovitskiy, L. Beyer, A. Kolesnikov, D. Weissenborn, X. Zhai, T. Unterthiner, M. Dehghani, M. Minderer, G. Heigold, S. Gelly, *et al.*, “An image is worth 16x16 words: Transformers for image recognition at scale,” *arXiv preprint arXiv:2010.11929*, 2020.
24. M. Singh, Q. Duval, K. V. Alwala, H. Fan, V. Aggarwal, A. Adcock, A. Joulin, P. Dollár, C. Feichtenhofer, R. Girshick, *et al.*, “The effectiveness of mae pre-pretraining for billion-scale pretraining,” in *Proceedings of the IEEE/CVF international conference on computer vision*, pp. 5484–5494, 2023.
25. J. Deng, W. Dong, R. Socher, L.-J. Li, K. Li, and L. Fei-Fei, “Imagenet: A large-scale hierarchical image database,” in *2009 IEEE conference on computer vision and pattern recognition*, pp. 248–255, Ieee, 2009.
26. A. Krizhevsky, G. Hinton, *et al.*, “Learning multiple layers of features from tiny images,” 2009.
27. J. Wasserthal, H.-C. Breit, M. T. Meyer, M. Pradella, D. Hinck, A. W. Sauter, T. Heye, D. T. Boll, J. Cyriac, S. Yang, *et al.*, “Totalsegmentator: robust segmentation of 104 anatomic structures in CT images,” *Radiology: Artificial Intelligence*, vol. 5, no. 5, 2023.
28. A. Diaz-Pinto, S. Alle, V. Nath, Y. Tang, A. Ihsani, M. Asad, F. Pérez-García, P. Mehta, W. Li, M. Flores, *et al.*, “Monai label: A framework for ai-assisted interactive labeling of 3d medical images,” *Medical Image Analysis*, vol. 95, p. 103207, 2024.
29. S. Plotka, M. Chrabaszcz, and P. Biecek, “Swin smt: Global sequential modeling for enhancing 3d medical image segmentation,” in *International Conference on Medical Image Computing and Computer-Assisted Intervention*, pp. 689–698, Springer, 2024.
30. Z. Ji, D. Guo, P. Wang, K. Yan, L. Lu, M. Xu, Q. Wang, J. Ge, M. Gao, X. Ye, *et al.*, “Continual segment: Towards a single, unified and non-forgetting continual segmentation model of 143 whole-body organs in CT scans,” in *Proceedings of the IEEE/CVF International Conference on Computer Vision*, pp. 21140–21151, 2023.
31. W. Li, C. Qu, X. Chen, P. R. Bassi, Y. Shi, Y. Lai, Q. Yu, H. Xue, Y. Chen, X. Lin, *et al.*, “Abdomenatlas: A large-scale, detailed-annotated, & multi-center dataset for efficient transfer learning and open algorithmic benchmarking,” *Medical Image Analysis*, vol. 97, p. 103285, 2024.
32. H. Liu, Z. Xu, R. Gao, H. Li, J. Wang, G. Chabin, I. Oguz, and S. Grbic, “Cosst: Multi-organ segmentation with partially labeled datasets using comprehensive supervisions and self-training,” *IEEE Transactions on Medical Imaging*, 2024.
33. L. K. S. Sundar, J. Yu, O. Muzik, O. C. Kulterer, B. Fueger, D. Kifjak, T. Nakuz, H. M. Shin, A. K. Sima, D. Kitzmantl, *et al.*, “Fully automated, semantic segmentation of whole-body 18F-FDG PET/CT images based on data-centric artificial intelligence,” *Journal of Nuclear Medicine*, vol. 63, no. 12, pp. 1941–1948, 2022.
34. A. Jaus, C. Seibold, K. Hermann, A. Walter, K. Giske, J. Haubold, J. Kleesiek, and R. Stiefelhagen, “Towards unifying anatomy segmentation: automated generation of a full-body CT dataset via knowledge aggregation and anatomical guidelines,” *arXiv preprint arXiv:2307.13375*, 2023.
35. K. Clark, B. Vendt, K. Smith, J. Freymann, J. Kirby, P. Koppel, S. Moore, S. Phillips, D. Maffitt, M. Pringle, *et al.*, “The cancer imaging archive (tcia): maintaining and operating a public information repository,” *Journal of digital imaging*, vol. 26, pp. 1045–1057, 2013.
36. “Grand challenge.” <https://grand-challenge.org>. Accessed: August 1, 2025.
37. MICCAI Society, “MICCAI Challenges.” <https://miccai.org/index.php/special-interest-groups/challenges/miccai-registered-challenges/>. Accessed: August 1, 2025.
38. A. Fedorov, R. Beichel, J. Kalpathy-Cramer, J. Finet, J.-C. Fillion-Robin, S. Pujol, C. Bauer, D. Jennings, F. Fennessy, M. Sonka, *et al.*, “3d slicer as an image computing platform for the quantitative imaging network,” *Magnetic resonance imaging*, vol. 30, no. 9, pp. 1323–1341, 2012.
39. R. Cornet and N. de Keizer, “Forty years of snomed: a literature review,” *BMC medical informatics and decision making*, vol. 8, pp. 1–6, 2008.
40. N. L. S. T. R. Team, “Data from the national lung screening trial (NLST).” The Cancer Imaging Archive.
41. I. E. Hamamci, S. Er, F. Almas, A. G. Simsek, S. N. Esirgun, I. Dogan, M. F. Dasdelen, O. F. Durugol, B. Wittmann, T. Amiranashvili, *et al.*, “Developing generalist foundation models from a multimodal dataset for 3d computed tomography,” *arXiv preprint arXiv:2403.17834*, 2024.
42. J. Ma, Y. Zhang, S. Gu, C. Zhu, C. Ge, Y. Zhang, X. An, C. Wang, Q. Wang, X. Liu, *et al.*, “Abdomenct-1k: Is abdominal organ segmentation a solved problem?,” *IEEE Transactions on Pattern Analysis and Machine Intelligence*, vol. 44, no. 10, pp. 6695–6714, 2021.
43. G. Podobnik, P. Strojani, P. Peterlin, B. Ibragimov, and T. Vrtovec, “Han-seg: The head and neck organ-at-risk CT and MR segmentation dataset,” *Medical physics*, vol. 50, no. 3, pp. 1917–1927, 2023.
44. S. Koitka, G. Baldini, L. Kroll, N. van Landeghem, O. B. Pollok, J. Haubold, O. Pelka, M. Kim, J. Kleesiek, F. Nensa, *et al.*, “Saros: A dataset for whole-body region and organ segmentation in CT imaging,” *Scientific Data*, vol. 11, no. 1, p. 483, 2024.
45. T. Amiranashvili, D. Lüdke, H. B. Li, B. Menze, and S. Zachow, “Learning shape reconstruction from sparse measurements with neural implicit functions,” in *International Conference on Medical Imaging with Deep Learning*, pp. 22–34, PMLR, 2022.
46. T. Amiranashvili, D. Lüdke, H. B. Li, S. Zachow, and B. H. Menze, “Learning continuous shape priors from sparse data with neural implicit functions,” *Medical Image Analysis*, vol. 94, p. 103099, 2024.
47. R. Mir, S. M. Kelly, Y. Xiao, A. Moore, C. H. Clark, E. Clementel, C. Corning, M. Ebert, P. Hoskin, C. W. Hurkmans, *et al.*, “Organ at risk delineation for radiation therapy clinical trials: Global harmonization group consensus guidelines,” *Radiotherapy and Oncology*, vol. 150, pp. 30–39, 2020.

48. E. Ziegler, T. Urban, D. Brown, J. Petts, S. D. Pieper, R. Lewis, C. Hafey, and G. J. Harris, "Open health imaging foundation viewer: an extensible open-source framework for building web-based imaging applications to support cancer research," *JCO clinical cancer informatics*, vol. 4, pp. 336–345, 2020.
49. S. Pai, I. Hadzic, D. Bontempi, K. Bressem, B. H. Kann, A. Fedorov, R. H. Mak, and H. J. Aerts, "Vision foundation models for computed tomography," *arXiv preprint arXiv:2501.09001*, 2025.
50. J. Liu, Y. Zhang, J.-N. Chen, J. Xiao, Y. Lu, B. A. Landman, Y. Yuan, A. Yuille, Y. Tang, and Z. Zhou, "Clip-driven universal model for organ segmentation and tumor detection," in *Proceedings of the IEEE/CVF international conference on computer vision*, pp. 21152–21164, 2023.
51. W. Lei, W. Xu, K. Li, X. Zhang, and S. Zhang, "Medlsam: Localize and segment anything model for 3d CT images," *Medical Image Analysis*, vol. 99, p. 103370, 2025.
52. Z. Huang, H. Wang, Z. Deng, J. Ye, Y. Su, H. Sun, J. He, Y. Gu, L. Gu, S. Zhang, *et al.*, "Stu-net: Scalable and transferable medical image segmentation models empowered by large-scale supervised pre-training," *arXiv preprint arXiv:2304.06716*, 2023.
53. M. Shen, Y. Bu, and G. W. Wornell, "On balancing bias and variance in unsupervised multi-source-free domain adaptation," in *International conference on machine learning*, pp. 30976–30991, PMLR, 2023.
54. V. Feofanov, E. Devijver, and M.-R. Amini, "Multi-class probabilistic bounds for majority vote classifiers with partially labeled data," *Journal of Machine Learning Research*, vol. 25, no. 104, pp. 1–47, 2024.
55. L. Breiman, "Bagging predictors," *Machine learning*, vol. 24, no. 2, pp. 123–140, 1996.
56. T. Hastie, R. Tibshirani, J. H. Friedman, and J. H. Friedman, *The elements of statistical learning: data mining, inference, and prediction*, vol. 2. Springer, 2009.
57. N. Heller, F. Isensee, K. H. Maier-Hein, X. Hou, C. Xie, F. Li, Y. Nan, G. Mu, Z. Lin, M. Han, *et al.*, "The state of the art in kidney and kidney tumor segmentation in contrast-enhanced CT imaging: Results of the kits19 challenge," *Medical image analysis*, vol. 67, p. 101821, 2021.
58. P. Bilic, P. Christ, H. B. Li, E. Vorontsov, A. Ben-Cohen, G. Kaissis, A. Szeskin, C. Jacobs, G. E. H. Mamani, G. Chartrand, *et al.*, "The liver tumor segmentation benchmark (lits)," *Medical Image Analysis*, vol. 84, p. 102680, 2023.
59. B. Landman, Z. Xu, J. Igelsias, M. Styner, T. Langerak, and A. Klein, "Miccai multi-atlas labeling beyond the cranial vault—workshop and challenge," in *Proc. MICCAI Multi-Atlas Labeling Beyond Cranial Vault—Workshop Challenge*, vol. 5, p. 12, 2015.
60. A. E. Kavur, N. S. Gezer, M. Barış, S. Aslan, P.-H. Conze, V. Groza, D. D. Pham, S. Chatterjee, P. Ernst, S. Özkan, *et al.*, "Chaos challenge-combined (CT-MR) healthy abdominal organ segmentation," *Medical Image Analysis*, vol. 69, p. 101950, 2021.
61. A. Sekuboyina, M. E. Husseini, A. Bayat, M. Löffler, H. Liebl, H. Li, G. Tetteh, J. Kukačka, C. Payer, D. Štern, *et al.*, "Verse: a vertebrae labelling and segmentation benchmark for multi-detector CT images," *Medical image analysis*, vol. 73, p. 102166, 2021.
62. P. Lo, B. Van Ginneken, J. M. Reinhardt, T. Yavarna, P. A. De Jong, B. Irving, C. Fetita, M. Ortner, R. Pinho, J. Sijbers, *et al.*, "Extraction of airways from CT (EXACT'09)," *IEEE Transactions on Medical Imaging*, vol. 31, no. 11, pp. 2093–2107, 2012.
63. G. González, D. Jimenez-Carretero, S. Rodríguez-López, C. Cano-Espinosa, M. Cazorla, T. Agarwal, V. Agarwal, N. Tajbakhsh, M. B. Gotway, J. Liang, *et al.*, "Computer aided detection for pulmonary embolism challenge (CAD-PE)," *arXiv preprint arXiv:2003.13440*, 2020.
64. L. Jin, J. Yang, K. Kuang, B. Ni, Y. Gao, Y. Sun, P. Gao, W. Ma, M. Tan, H. Kang, *et al.*, "Deep-learning-assisted detection and segmentation of rib fractures from CT scans: Development and validation of fracnet," *EBioMedicine*, vol. 62, 2020.
65. A. Hering, L. Hansen, T. C. Mok, A. C. Chung, H. Siebert, S. Häger, A. Lange, S. Kuckertz, S. Heldmann, W. Shao, *et al.*, "Learn2reg: comprehensive multi-task medical image registration challenge, dataset and evaluation in the era of deep learning," *IEEE Transactions on Medical Imaging*, vol. 42, no. 3, pp. 697–712, 2022.
66. J. Pedrosa, G. Aresta, C. Ferreira, G. Atwal, H. A. Phoulady, X. Chen, R. Chen, J. Li, L. Wang, A. Galdran, *et al.*, "Lndb challenge on automatic lung cancer patient management," *Medical image analysis*, vol. 70, p. 102027, 2021.
67. Eva van Rikxoort and Bram van Ginneken and Sjoerd Kerkstra, "LObe and Lung Analysis 2011 (LOLA11)." <https://lola11.grand-challenge.org/>, 2011.
68. T. Heimann, B. Van Ginneken, M. A. Styner, Y. Arzhaeva, V. Aurich, C. Bauer, A. Beck, C. Becker, R. Beichel, G. Bekes, *et al.*, "Comparison and evaluation of methods for liver segmentation from CT datasets," *IEEE transactions on medical imaging*, vol. 28, no. 8, pp. 1251–1265, 2009.
69. M.-P. Revel, S. Boussouar, C. de Margerie-Mellon, I. Saab, T. Lapotre, D. Mompoin, G. Chassagnon, A. Miron, M. Lederlin, S. Bennani, *et al.*, "Study of thoracic CT in COVID-19: the STOIC project," *Radiology*, vol. 301, no. 1, pp. E361–E370, 2021.
70. K. Murphy, B. Van Ginneken, J. M. Reinhardt, S. Kabus, K. Ding, X. Deng, K. Cao, K. Du, G. E. Christensen, V. Garcia, *et al.*, "Evaluation of registration methods on thoracic CT: the EMPIRE10 challenge," *IEEE transactions on medical imaging*, vol. 30, no. 11, pp. 1901–1920, 2011.
71. Y. Ji, H. Bai, C. Ge, J. Yang, Y. Zhu, R. Zhang, Z. Li, L. Zhanng, W. Ma, X. Wan, *et al.*, "Amos: A large-scale abdominal multi-organ benchmark for versatile medical image segmentation," *Advances in neural information processing systems*, vol. 35, pp. 36722–36732, 2022.
72. B. Rister, K. Shivakumar, T. Nobashi, and D. L. Rubin, "CT-ORG: A dataset of CT volumes with multiple organ segmentations." The Cancer Imaging Archive, 2019.

73. S. G. A. III and et al., “Data from LIDC-IDRI.” The Cancer Imaging Archive, 2015.
74. H. Roth and et al., “A new 2.5 D representation for lymph node detection in CT (CT lymph nodes).” The Cancer Imaging Archive, 2015.
75. N. C. I. C. P. T. A. C. (CPTAC), “The clinical proteomic tumor analysis consortium clear cell renal cell carcinoma collection (CPTAC-CCRCC).” The Cancer Imaging Archive, 2018.
76. N. C. I. C. P. T. A. C. (CPTAC), “The clinical proteomic tumor analysis consortium lung adenocarcinoma collection (CPTAC-LUAD).” The Cancer Imaging Archive, 2018.
77. P. An and et al., “CT images in COVID-19.” The Cancer Imaging Archive, 2020.
78. S. Bakr and et al., “Data for NSCLC radiogenomics collection.” The Cancer Imaging Archive, 2017.
79. H. Roth, A. Farag, E. B. Turkbey, L. Lu, J. Liu, and R. M. Summers, “Data from pancreas-CT.” The Cancer Imaging Archive, 2016.
80. J. Hong and et al., “Breath-hold CT and cone-beam CT images with expert manual organ-at-risk segmentations from radiation treatments of locally advanced pancreatic cancer (Pancreatic-CT-CBCT-SEG).” The Cancer Imaging Archive, Oct. 2021.
81. B. Zhao, L. H. Schwartz, M. G. Kris, and G. J. Riely, “Coffee-break lung CT collection with scan images reconstructed at multiple imaging parameters.” The Cancer Imaging Archive, 2015.
82. M. W. Linehan, R. Gautam, C. A. Sadow, and S. Levine, “The cancer genome atlas kidney chromophobe collection (TCGA-KICH).” The Cancer Imaging Archive, 2016.
83. O. Akin and et al., “The cancer genome atlas kidney renal clear cell carcinoma collection (TCGA-KIRC).” The Cancer Imaging Archive, 2016.
84. M. Linehan and et al., “The cancer genome atlas cervical kidney renal papillary cell carcinoma collection (TCGA-KIRP).” The Cancer Imaging Archive, 2016.
85. B. J. Erickson and et al., “The cancer genome atlas liver hepatocellular carcinoma collection (TCGA-LIHC).” The Cancer Imaging Archive, 2016.
86. S. Rühling, F. Navarro, A. Sekuboyina, M. El Hussein, T. Baum, B. Menze, R. Braren, C. Zimmer, and J. S. Kirschke, “Automated detection of the contrast phase in MDCT by an artificial neural network improves the accuracy of opportunistic bone mineral density measurements,” *European Radiology*, pp. 1–10, 2022.
87. H. Möller, H. Schön, A. Dima, B. Keinert-Weth, R. Graf, M. Atad, J. Paetzold, F. Jungmann, R. Braren, F. Kofler, *et al.*, “Automated thoracolumbar stump rib detection and analysis in a large ct cohort,” *arXiv preprint arXiv:2505.05004*, 2025.
88. F. Isensee, T. Wald, C. Ulrich, M. Baumgartner, S. Roy, K. Maier-Hein, and P. F. Jaeger, “nnu-net revisited: A call for rigorous validation in 3d medical image segmentation,” *arXiv preprint arXiv:2404.09556*, 2024.
89. L. Maier-Hein, A. Reinke, P. Godau, M. D. Tizabi, F. Buettner, E. Christodoulou, B. Glocker, F. Isensee, J. Kleesiek, M. Kozubek, *et al.*, “Metrics reloaded: recommendations for image analysis validation,” *Nature methods*, vol. 21, no. 2, pp. 195–212, 2024.
90. J. Jia, M. Staring, and B. C. Stoel, “seg-metrics: a python package to compute segmentation metrics,” *medRxiv*, pp. 2024–02, 2024.
91. Google DeepMind, “Surface Distance Metrics.” <https://github.com/google-deepmind/surface-distance>, 2024. Accessed: August 1, 2025.

## A Online Methods

### Ethics statement

This study has received ethical approval from two independent institutional review boards. The Clinical Research Ethics Committee at Istanbul Medipol University (E-10840098-772.02-6841, 27/10/2023) approves the release of 484 new head CT scans and associated models. The Ethics Committee of the Technical University of Munich (TUM) (27/19 S-SR) authorizes the scientific use and publication of 586 anonymized, triphasic contrast-enhanced abdominal CT scans.

## 1 Data collection and preprocessing

### 1.1 CADS-dataset: Image collection and curation

Robust deep learning models for whole-body CT segmentation require extensive and diverse datasets that capture anatomical variations across different populations and imaging protocols. We hypothesize that utilizing a large volume of images, including those without manual annotations, can enhance segmentation performance and model generalization compared to smaller, hand-annotated datasets alone. This approach aligns with established findings that larger datasets improve model generalization and robustness on unseen domains [19,93,94]. This data-centric approach helps address healthcare data challenges such as class imbalance and potential biases while reducing overfitting risks [95].

We aggregate our dataset from diverse sources, including medical imaging challenges (*e.g.*, Grand Challenge [36], MICCAI challenges [37]) and public repositories such as The Cancer Imaging Archive (TCIA) [35]. Our selection criteria focus on CT scans that cover key anatomical regions throughout the body, including the brain, head-and-neck, thorax, abdomen, pelvis, and femur. To maximize data diversity and scale, we do not restrict our collection to annotated scans. Consequently, approximately 79% of our initial collection does not include any manual annotations.

To strengthen the annotated portion of our dataset, we incorporate precisely labeled images from existing large-scale datasets such as TotalSegmentator [27] and SAROS [44]. Furthermore, three in-house medical research assistants and a radiation oncologist (JCP) contributes additional manual annotations to the VISCERAL Gold Corpus dataset [12]. These new annotations expand coverage to include critical structures such as the spinal canal, larynx, heart, mammary glands, colostomy bag, sigmoid colon, rectum, prostate, and seminal vesicles that are essential for radiotherapy planning, extending beyond the original abdominal and thoracic focus. These new manual annotations are publicly released as part of the CADS-dataset alongside this work.

We further enhance the dataset with two new CT collections. First, we include 484 anonymized head CT scans from patients aged  $\geq 18$  years from Istanbul Medipol University (see row “New Hospital Data - Head” in Table 1), further augment the existing cranial image resources in the dataset. Second, we incorporate 586 triphasic contrast-enhanced abdominal CT scans (non-enhanced, arterial, and portal venous phases) from TUM Klinikum Rechts der Isar (see row “New Hospital Data - CT-TRI” in Table 1), featuring a higher prevalence of liver and kidney tumors [86]. All newly acquired head and abdominal CT scans are made publicly available within the CADS-dataset.

The final aggregated dataset comprises 22,022 CT scans, representing one of the most comprehensive collections for whole-body CT segmentation to date (Table 1). For rigorous evaluation, we partition these scans into non-overlapping training and test sets (Supplementary Table A.3). All model development decisions, including hyperparameter tuning and architecture selection, rely exclusively on validation data from the training split, ensuring complete independence of the hold-out test sets throughout development.

### 1.2 CADS-dataset: Preprocessing and standardization

Our diverse image collection requires standardized preprocessing to ensure consistency across varying formats, resolutions, and orientations. We implement a three-step pipeline:

First, we reorient all images to the standard RAS (Right-Anterior-Superior) convention. Second, we resample to a uniform 1.5 mm isotropic resolution, which balances segmentation accuracy with computational efficiency, as finer resolutions would substantially increase runtime and memory requirements for deep learning models. Third, we simplify the original affine transformation matrices by removing rotation and translation components, preserving only scaling and shear. This simplification is crucial for downstream tasks, such as pseudo-label quality control, which may involve shape analysis and direct comparisons of anatomical structures across different scans.

For patient privacy in newly acquired hospital head CT scans, we apply a Gaussian filter ( $\sigma = 5$  voxels at 1.5 mm spacing) to facial regions. This relatively strong blurring effectively obscures identity while preserving the overall structural integrity required for anatomical analysis near the face area.



## 2 CADS-dataset: Annotation pipeline development

### 2.1 From partial annotations to whole-body pseudo-labels

Our collected dataset (Section 1) presents a significant imbalance between labeled and unlabeled data, *i.e.*, only 21% of images have manual annotations, often for just one or two structures, while 79% lack any annotations. While supervised training requires paired image-label data, obtaining comprehensive annotations for all 167 target structures across our entire dataset is resource-prohibitive. To leverage this partially annotated dataset effectively, we employ pseudo-labeling, a semi-supervised learning strategy based on the cluster assumption [96]. This assumption suggests that data points of the same class form cohesive clusters in the feature space. Our approach uses initial model predictions to assign labels to unlabeled samples. By utilizing the distribution information within unlabeled data, this method forms smoother decision boundaries, enhances model generalization, and mitigates overfitting.

To address the complexity of segmenting 167 diverse anatomical structures, we develop specialized models for distinct anatomical regions or categories. As shown in Figure 2, we categorize these structures into nine groups (detailed in Figure 1 and Supplementary Table A.2). Our training data draws from multiple sources.

(1) The *TotalSegmentator* dataset [27] provides a foundation with annotations for 104 structures, including vital organs, vessels, and bones, forming five of our nine specialized groups.

(2) *Organs at risk (OARs)*: Our in-house medical team, comprising three medical research assistants and a radiation oncologist (JCP), manually annotates 10 additional structures on images from the VISCERAL Gold Corpus dataset [12], creating an OAR group including spinal canal, larynx, heart chambers, and other structures critical for radiotherapy planning.

(3) *Head-and-neck structures*: The Han-Seg dataset [43] provides training data for head-and-neck structures, covering essential components such as cochlea, optic nerves, and carotid arteries.

(4) *Brain structures*: We generate annotations by registering Han-Seg CT scans with the SimNIBS MRI atlas [97] using ANTS non-rigid transformation [98]. These registration-derived annotations ensure consistency across the dataset.

(5) *Broad anatomical context structures*: The SAROS dataset [44] contributes broader anatomical context structures, such as subcutaneous tissue and major body cavities. The dataset provides sparse slice-based 2D annotations, with labels available only on selected slices. To create dense 3D per-slice annotations required for volumetric training, we perform interpolation between the annotated slices.

Using these carefully prepared initial training sets, we employ the nnU-Net framework [22] to train specialized models for each body group. These models then generate pseudo-labels for all 167 structures across our entire 22,022 CT scan collection.

### 2.2 Shape-informed label quality control

The diversity of images in our large-scale CT collection is a key property of our dataset and is a major contributor to robustness of the emerging segmentation models. A dataset of this scale also inevitably contains outlier images – volumes with wrong spacings and orientation, unusually high noise levels, low contrast, etc. Such outliers cause catastrophically bad segmentations during pseudo-labeling. While the overall image diversity is important for downstream model robustness, erroneous pseudo-labels will degrade the final model’s performance [99,100]. We balance this trade-off by ranking pseudo-labels in terms of their quality and removing a certain percentage of worst pseudo-labels from the downstream training data.

We formulate ranking of pseudo-labels as likelihood estimation in shape space. Our approach has a few unique properties. First, it is automated, allowing ranking of large-scale datasets. Second, training of our likelihood estimator requires only ground-truth segmentations and does not rely on degraded shapes at training time. This makes our method’s ranking performance agnostic to any specific failure modes of the pseudo-labeling network, essentially performing unbiased, zero-shot (or unsupervised) outlier detection. Lastly, we focus directly on pseudo-labels instead of images for ranking. Arguably, this leads to a simpler problem outlier detection in shape space, compared to image space. Furthermore, it allows us to take the generalization ability of the pseudo-labeler network into account and only exclude images where it fails.

To perform likelihood estimation, we train an auto-decoder on ground-truth multi-class segmentation labels, taken from the fully-annotated datasets. The auto-decoder is based on implicit neural representations [45,46] and allows us to effectively model heterogeneous high-resolution volumes with varying fields of view. At inference time, we reconstruct an unseen multi-class pseudo-label with our shape prior model. For more details about training and reconstruction, we refer the reader to [45,46]. Since the shape prior has been trained on clean ground-truth segmentation masks, it will not be able to reconstruct erroneous segmentation masks. Therefore, shape likelihood can be connected to the distance between the observed

pseudo-label and its reconstruction, with large distance indicating an outlier. Note that this method does not rely on any ground-truth at inference time.

Different choices of the metric can be made to measure the distance between a pseudo-label and its reconstruction. We choose Hausdorff distance due to its sensitivity to outliers, in contrast to Dice score. Since a few far-off voxels are unlikely to hinder subsequent segmentation model training, we choose a more robust 90-percentile Hausdorff distance. This approach allows us to automatically estimate quality scores for pseudo-labels without relying on their corresponding ground-truth, with a large Hausdorff distance indicating a low-quality pseudo-label.

### 2.3 Enhancing robustness via complementary training approaches

The specialized models are initially trained on small fully-annotated datasets to learn specific anatomical structures. However, when applying these models to generate pseudo-labels across the entire 22,022 CT scans, two challenges may arise: (1) distribution shifts between the training data and the target data lead to inconsistent predictions on scans outside the training distribution [101,102]; (2) the limited size of initial training datasets restricts the models’ ability to capture anatomical variations [103], increasing overfitting risks to source-specific characteristics [104]. These limitations introduce noise and inaccuracies in the generated pseudo-labels that must be addressed before downstream use.

To generate high-quality labels for the entire CADSDataset, we develop a multi-strategy approach. As shown in Figure 2, this process involves three steps: (1) preparing distinct labeled data subsets, (2) training complementary models (“flavors”) on each subset, and (3) combining their predictions to create final labels. We define three training data flavors:

*GT-flavor:* This model is trained directly on original ground truth (GT) annotations. Although smaller in data amount compared to pseudo-labeled data, these GT annotations provide the highest quality labels that are available without further manual intervention. This precision is crucial for challenging structures that are small, complex, or infrequent, since training on high-fidelity GT annotations enables the model to learn fine-grained details and precise boundaries. However, the limited quantity of paired image-label samples prevents the model from learning the rich anatomical variations present in the complete 22,022 CT scans.

*Pseudo-flavor:* The Pseudo-flavor model utilizes all 22,022 training images with their initially generated pseudo-labels (Section 2.1). This large-scale approach provides access to more anatomical variations than the available GT data alone cannot capture. The large volume of pseudo-labeled data helps the model better learn the underlying data distribution, smoothing decision boundaries according to the cluster assumption and reducing overfitting risks compared to smaller datasets. We further optimize training by selecting task-specific subsets for different anatomical targets. For example, we filter images for head presence when training brain and head-and-neck models (Section 3.1). This targeted selection improves training efficiency for specific anatomical domains. The detailed training image counts for each specialized group are provided in Supplementary Table A.4. Although this approach benefits from larger scale and diversity, the inherent nature of pseudo-labels can introduce noise and inaccuracies.

*Shape-flavor:* The Shape-flavor model aims to improve label quality by training exclusively on more reliable pseudo-labels identified through our shape-based quality control process (Section 2.2). We use trained shape-informed models to compute anatomical plausibility scores for each structure’s pseudo-labels. The lowest-scoring 10% of images are identified as anatomically inconsistent and excluded from training. Unlike the Pseudo-flavor model which uses all 22,022 images, the Shape-flavor focuses on more anatomically plausible pseudo-labels. This approach helps capture finer shape details and reduces sensitivity to outliers and artifacts. The 10% exclusion threshold balances between data quality improvement and maintaining sufficient training samples for robust learning.

### 2.4 Statistical ranking and selection of model flavors

After training the three model flavors, we determine which flavor model provides the most reliable segmentation for each target structure. We evaluate performance using both in-distribution (ID) and out-of-distribution (OOD) validation data. ID validation images come from five core data sources (described in Section 2.1) that provide GT labels for initial model training. OOD validation images come from other labeled datasets in our collection (*e.g.*, for liver segmentation, while the model is trained on TotalSegmentator dataset (ID), its OOD validation leverages annotations from LiTS, VISCERAL, BTCV-Abdomen datasets, and etc.). We prioritize OOD performance metrics when available because they can better reflect model generalization.

For each anatomical structure, we implement a performance-driven process (Algorithm 1) to identify the most reliable model flavor. We evaluate segmentation quality using Dice Similarity Coefficient (Dice)



as the primary metric and 95-percentile Hausdorff distance (HD95) as a secondary metric. The selection process for each anatomical target follows these steps:

*Step-1:* We calculate mean Dice scores for each flavor using OOD validation results when available. Otherwise, we use ID results.

*Step-2:* We perform statistical tests (significance threshold  $p < 0.05$ ) to assess if the observed Dice score differences between three flavors are statistically significant. First, we use the Shapiro-Wilk test to check data normality and Levene’s test to assess variance equality. Based on these results, we select the appropriate comparison method: ANOVA, Welch’s ANOVA, or Kruskal-Wallis test. We then perform post-hoc tests (Tukey’s HSD or Dunn’s test) to identify significant differences between flavors.

*Step-3:* We assign initial ranking points to each model flavor based on statistical comparisons or mean Dice scores when no significant differences exist.

*Step-4:* When Dice scores do not clearly identify the best flavor (*i.e.*, multiple flavors share the highest rank or have statistically indistinguishable top performance), we conduct secondary evaluation using HD95 metrics. We perform similar statistical analysis on HD95 scores to refine the ranking of ambiguous cases.

*Step-5:* Based on total ranking points, we establish a final priority order for the three flavors. The highest-ranked flavor’s pseudo-label becomes the final label for that structure in the CADS-dataset.

The final assignment of flavors and targets is shown in Supplementary Figure A.8. This systematic approach ensures we select the best-performing flavor for each anatomical structure based on quantitative measurements.

## 2.5 Assembly of final labels

The final step in creating the CADS-dataset involves assembling a unified label set that integrates pseudo-labels from the best-performing model flavor for each anatomical structure (Section 2.4). When available, original GT annotations take highest priority and replace corresponding pseudo-labels to ensure maximum label fidelity.

Our integration process requires a merging strategy to handle potential overlapping segmentations from different model flavors’ results. Hence, we implement a progressive merging order based on label reliability. The process follows three main steps:

First, we establish a base layer using pseudo-labels from structures whose selected flavor shows the lowest mean Dice score within each anatomical group. We then progressively add pseudo-labels from structures with higher mean Dice scores. For structures with identical Dice scores, we prioritize those with higher proportions of GT annotations in their respective training data. Finally, we merge original GT annotations if available. These GT labels serve as higher standard and overwrite any existing pseudo-labels for the same structures. Overall, this sequential integration ensures that less reliable segmentations are replaced by more reliable ones. The complete statistics of the resulting CADS-dataset label set are summarized in Supplementary Table A.5.

## 3 Post-processing and refinements

### 3.1 Refining head region pseudo-labels: Mitigating hallucinations

Our specialized models trained exclusively on head region images from the Han-Seg dataset face a unique challenge when generating pseudo-labels for scans that include other body parts. Due to their training on this limited anatomical domain, these models are susceptible to generating false-positive (FP) predictions when encountering unseen anatomical contexts outside the head region. This hallucination effect [105,106] occurs because the models lack exposure to non-head anatomical structures during training. We implement an automated two-step postprocessing strategy to address this issue.

In the first step, we apply a quality control filter to identify scans with adequate brain coverage. We use the predicted brain segmentation voxel count as an indicator. Scans with predicted brain voxel counts below 2,000 voxels are excluded from head structure pseudo-label generation. This threshold represents approximately 10% of the brain size interquartile range in our dataset. It serves as a robust indicator for identifying scans where the head is not clearly visible or has limited field of view.

The second step addresses images that contain both head and extended body regions. We perform targeted cropping of the initial head-related pseudo-labels to remove FP predictions that extend into other body parts. This process preserves predictions within a defined bounding box centered around the predicted brain segmentation centroid. The bounding box dimensions vary by structure group: (1) for brain structures:  $\pm[100, 100, 133]$  voxels along the  $x$ -,  $y$ -, and  $z$ -axes; (2) for head-and-neck structures:  $\pm[100, 100, 200]$  voxels to accommodate neck coverage.

These refined pseudo-labels are then used in subsequent pipeline stages. Our postprocessing approach significantly reduces FP segmentations outside the intended anatomical region. This improves the overall quality and anatomical accuracy of head structure pseudo-labels across the CADs-dataset.

### 3.2 Refinement of rib segmentation for clinical accuracy

Accurate individual rib segmentation presents challenges in clinical applications, with growing concerns in the medical imaging community regarding the quality of existing rib annotations [87]. Existing datasets and automated methods often have two main insufficiencies: (1) incomplete segmentation, *i.e.*, missing the part of costovertebral joints where ribs meet vertebrae, and (2) segmentation artifacts, where a single rib might be fragmented or inconsistently labeled as multiple rib classes. Hence, we develop a specialized refinement process for the CADs-dataset rib labels to ensure anatomical correctness in the segmentations.

In the first stage, we address fragmented or inconsistently labeled rib predictions through following steps. We begin by binarizing the multi-class rib segmentation to identify all foreground voxels representing the whole rib structure. We then perform connected components analysis on top of the binary rib map to delineate all spatially distinct, contiguous segments, and assign each a unique temporary label. Next, for each of these segments, we determine the most probable rib class through majority voting based on the original rib segmentation classes. This process ensures each rib structure maintains consistent labeling.

The second stage focuses on retrieving commonly omitted costovertebral joints in existing segmentation approaches. We begin by leveraging vesselFM [107], a foundation model initially developed from 3D blood vessel segmentation, which has a strong inductive bias towards tubular shapes. We utilize vesselFM to detect all tube-like structures throughout the body. With ribs also falling in this category, we effectively retrieve the complete contour of ribs, intrinsically including the costovertebral joint regions, but simultaneously yields a broad binary map containing many tubular structures beyond the target joints. To create a region of interest, we dilate the spine mask from our model predictions, which helps identify potential joint locations since costovertebral joints anatomically connect to vertebrae. We then isolate potential joint structures by selecting vesselFM predictions that intersect the dilated spine region but exclude the spine itself. To further refine these candidates, we apply morphological opening to remove noise and separate components. We then filter components based on size, retaining those between 100 and 1,500 voxels. Finally, we assign each validated joint component to the nearest rib within a defined proximity threshold. This systematic pipeline significantly improves the anatomical accuracy of rib segmentations in the CADs-dataset. It addresses both fragmentation artifacts and missing costovertebral joints to create more complete and anatomically accurate rib labels.

## 4 CADs-model architecture and training

### 4.1 Developing the CADs-model: Balanced training strategies for large-scale segmentation

Following the creation of CADs-dataset (Sections 1.1-3.2), we develop the CADs-model to leverage this rich data resource. Our objective is to train a model with enhanced generalization capabilities by utilizing the dataset’s substantial size and anatomical diversity compared to those typically developed on smaller, single-source datasets.

We select the nnU-Net framework [88] with its residual encoder UNet configuration for our model architecture. This choice is based on nnU-Net’s proven state-of-the-art performance in medical image segmentation and its computational efficiency for large-scale training. However, training on large heterogeneous datasets presents a significant challenge of class imbalance. This uneven distribution of anatomical structures can lead to biased model training [108], unbalanced gradient updates [109], and inadequate learning of minority classes [110]. In the CADs-dataset, this class imbalance can be observed in structures like the uppermost cervical vertebrae (C1-C5) that appear less frequently across the 22,022 volumes (Supplementary Table A.5).

To mitigate the influence of class imbalance and ensure balanced performance across all 167 target structures, we modify the standard nnU-Net training process. While nnU-Net by default applies uniform image sampling and prioritizes foreground classes during patch sampling, it does not distinguish between minority and majority foreground classes. Therefore, we perform oversampling that assigns sampling weights based on the inverse probability of class occurrence. For example, less frequent C1-C5 vertebrae receive higher sampling weights than other vertebral segments to ensure adequate representation during training.

Furthermore, the CADs-dataset also enables customized training tailored to specific anatomical regions. Instead of using all 22,022 images uniformly, we create targeted subsets for specialized tasks. For instance, for head-related groups, we select images containing adequate head coverage using specific criteria: predicted brain voxel count exceeding 2,000 voxels for the brain group and at least 24 target structures

for the head-and-neck group. This approach optimizes training efficiency for region-specific targets. The final training image counts for each specialized group are detailed in Supplementary Table A.4.

## 5 Evaluation framework and performance analysis

### 5.1 Quantitative assessment and false negative penalization

Our evaluation combines a suite of metrics that quantitatively capture both overall volume overlap and boundary accuracy, complemented by a specific penalization strategy for false negatives.

*Dice Coefficient:* Dice serves as our primary voxel-based metric for quantifying overlap between GT and predicted segmentation. As defined in Equation 5.1, it computes twice the intersection volume divided by the sum of both volumes. The resulting value ranges from 0 (no overlap) to 1 (perfect overlap) and provides a direct measure of volumetric agreement.

*Normalized Surface Dice (NSD):* NSD evaluates segmentation boundary similarity by considering surface points within a specified tolerance distance ( $\tau$ ). In Equation 5.1,  $S$  represents the boundary and  $\mathcal{B}$  denotes the tolerated region around the boundary with offset  $\tau$  [89]. NSD ranges from 0 to 1, with 1 indicating perfect surface overlap. We set the tolerance  $\tau$  to 3mm based on a voxel spacing of 1.5mm when training the models.

*Hausdorff Distance (HD):* For boundary accuracy assessment, we use two distance-based metrics. The HD measures the maximum distance between any point on the predicted contour and its nearest point on the GT contour (and vice-versa). This metric captures the largest spatial discrepancy between boundaries.

*95% Hausdorff Distance (HD95):* It uses the 95th percentile of point-to-surface distances to provide a more robust measure by excluding the most distant 5% of points, thus mitigating the sensitivity of standard HD to extreme outliers. A lower HD95 value indicates better boundary alignment.

These metrics complement each other in our evaluation. While Dice scores assess overall volumetric agreement, surface-distance metrics capture intricate shape details crucial for smaller or anatomically complex organs. Computing all four metrics for each target ensures systematic evaluation of segmentation performance.

$$\text{DSC}(GT, Pred) = \frac{2|GT \cap Pred|}{|GT| + |Pred|} \quad (1)$$

$$\text{NSD}(S_{GT}, S_{Pred}, \tau) = \frac{|S_{GT} \cap \mathcal{B}_{S_{Pred}}^{(\tau)}| + |S_{Pred} \cap \mathcal{B}_{S_{GT}}^{(\tau)}|}{|S_{GT}| + |S_{Pred}|} \quad (2)$$

$$\text{HD}(S_{GT}, S_{Pred}) = \max \left\{ \sup_{g \in S_{GT}} \inf_{p \in S_{Pred}} d(g, p), \sup_{p \in S_{Pred}} \inf_{g \in S_{GT}} d(p, g) \right\} \quad (3)$$

$$\text{HD95}(S_{GT}, S_{Pred}) = \max \left\{ P_{95} \left( \left\{ \min_{p \in S_{Pred}} d(g, p) \mid g \in S_{GT} \right\} \right), P_{95} \left( \left\{ \min_{g \in S_{GT}} d(p, g) \mid p \in S_{Pred} \right\} \right) \right\} \quad (4)$$

*False Negative (FN):* FNs occur when the model fails to detect organs present in the images. This issue is particularly evident for small structures (*e.g.*, arytenoid, cochlea, and etc.) due to severe foreground-background class imbalance. The likelihood of FNs also increases in partially visible structures that can be found in cropped scans (from datasets like TotalSegmentator or VerSe). Addressing FNs is crucial for clinical evaluation because missing even a small organ can have significant consequences.

Hence, we implement the FN penalization strategy to provide fair and clinically relevant assessment. Our approach first distinguishes between genuinely missed structures and those largely outside the field of view. We consider a structure as truly missed when it occupies a reasonably visible volume (exceeding 90% of the organ’s average volume, reference statistics in Supplementary Table A.5) but is still entirely absent in the prediction. For these true FN cases we override the standard metrics: both Dice and NSD are set to 0, while HD and HD95 receive a maximum penalty value equal to the diagonal length of image bounding box. Conversely, we exclude structures from evaluation when their GT volume is less than 10% of the average. Such minimal volumes typically indicate structures mostly outside the field of view where organ identification becomes impractical. While this penalization may increase overall mean values for distance-based metrics like HD95 due to maximum penalty assignments, it ensures appropriate penalization of missing segmentations rather than ignoring them.

## 5.2 Cross-dataset evaluation: Annotation alignment and special case handling

We standardize our evaluation process by adapting model outputs to match each dataset’s annotation scheme. For datasets that combine multiple structures into single classes (such as “kidneys” including both left and right, or “lungs” including multiple lobes), we merge the model’s corresponding predictions before metric calculation. This adaptation applies to datasets like KiTS, CT-ORG, AbdomenCT-1K, VISCERAL Gold Corpus and Silver Corpus, and EMPIRE10. In datasets like KiTS and LiTS, we merge lesion or tumor annotations into their corresponding organ categories to match the primary organ segmentation task.

Some datasets require special handling. The SAROS dataset provides annotations for only every fifth axial slice. Therefore, we restrict our analysis to these annotated slices and exclude intermediate slices without original GTs. For the VerSe dataset, we exclude scans with atypical anatomical variations such as lumbar sacralization (L6) or thoracic lumbarization (T13), following the convention in previous studies [27]. These transitional vertebrae cases are excluded from evaluation due to their rarity.

For serially repeating structures like vertebrae and ribs, our label assembly process (Section 2.5) takes them as unified groups rather than individual elements. This approach prevents label merging conflicts at junctions and ensures consistency. We group vertebrae into cervical, thoracic, and lumbar segments. For ribs, we apply uniform labels from a single model flavor across all rib segments.

## 5.3 Details of real-world hospital evaluation cohort

The University Hospital Zurich evaluation cohort comprises 2,864 CT scans from patients with various oncological conditions, representing a diverse spectrum of pathologies commonly encountered in radiation oncology practice. Supplementary Table A.6 details the distribution of primary disease sites, with central nervous system malignancies, bone tumors, and head and neck cancers constituting the majority of cases.

For this cohort, reference annotation masks were either generated using MIM software and validated by medical doctors, or directly contoured by radiation oncologists following standard clinical protocols. These clinically validated segmentations serve as the reference standard for computing all quantitative performance metrics reported in our evaluation.

## 5.4 Extended evaluation of the CADS-model

We provide more evaluation results of the CADS-model’s segmentation performance. We present detailed structure-by-structure comparisons with the TotalSegmentator baseline, including Dice and HD95 scores (mean  $\pm$  std, median, 95% CI) for all 167 anatomical targets (Supplementary Table A.12). The results are visualized in radar plots and grouped by anatomical system (Supplementary Figures A.9 to A.11).

Our evaluation includes comparative assessments of Hausdorff Distance (HD) and Normalized Surface Dice (NSD) across test cohorts (Supplementary Table A.8), and detailed performance analysis for each dataset (Supplementary Table A.7). For real-world hospital validation, we report individual results for Dice, HD95, HD, Normalized Surface Dice, True Positive Rate (TPR), and Error Volume metrics (Supplementary Tables A.9 to A.11). We also provide score distributions across all 167 targets (Supplementary Figures A.12 to A.15).

# 6 Technical details and quality assurance

## 6.1 Implementation details

*Initial specialized models:* We configure our initial label propagation models as 3D full-resolution U-Nets within the nnU-Net framework. We disable mirroring throughout development to prevent confusion from anatomical symmetries.

*Three model flavors:* Our three flavor models share a common architecture based on nnU-Net with modifications for computational efficiency. The architecture consists of a 5-layer 3D U-Net with channel numbers [32, 64, 128, 256, 512] and stride-2 sampling. We use instance normalization for feature scaling and Parametric Rectified Linear Units (PReLU) for activation. Each layer includes two convolutional residual units for improved feature retention and flow. For image preprocessing, we scale intensities from the 5th to 95th percentiles to the range [0, 1] and apply clipping for contrast enhancement. During training, we randomly crop four patches of size (128, 128, 128) per image with balanced foreground-background sampling. We train all models for 200 epochs using a batch size of 2. The Adam optimizer starts with a learning rate of  $1 \times 10^{-4}$  and follows cosine annealing. We monitor performance using Dice Cross-entropy loss and Dice metrics. These optimizations reduce computational costs across the pipeline to accommodate our 22,022 images.

*CADS-model:* The CADS-model uses a 3D full-resolution U-Net with residual connections in the encoder path. We select this architecture for robust performance and efficient runtime. The model uses moderate batch and patch sizes compatible with 24GB VRAM GPUs following nnU-Net’s L configuration [88]. We maintain disabled mirroring to preserve accuracy for symmetrical organs.

*Libraries:* We develop our models using PyTorch (version 2.5.1) with CUDA 12.4. The implementation uses the nnU-Net framework (version 2.5.1). We compute evaluation metrics using Seg-metrics [90] and surface-distance [91] packages. Postprocessing utilizes the TPTBox Python library. All code is available on GitHub.

*Computational resources:* Before model training, the required preprocessing steps in nnU-Net take approximately 9 hours for 22,000 images. We conduct model training primarily on NVIDIA A100 GPUs. Training duration varies depending on the complexity and number of targets in each model group. For reference, completing 1,000 epochs ranged from 83 to 161 hours. Training a single model utilizes one 80GB A100 GPU, complemented by 120GB of RAM and 6 CPU cores.

## 6.2 Manual review and curation of test set annotations

To ensure a reliable model evaluation, a review process is conducted for a significant portion of our unseen test set, specifically for images from the TotalSegmentator dataset. This dataset covers 104 structures, which aligns with over 60% of our 167 segmentation targets. However, preliminary inspection reveals inaccuracies in various GT annotations, particularly evident in ribs and vertebrae (illustrated in Figure 5a). These GT imprecisions can significantly impact model evaluation correctness.

Hence, we perform quality assessment on GT labels in 65 test images from TotalSegmentator dataset. Before detailed review, we correct obvious systematic errors such as mislabeled ribs and vertebrae. Then, in-house medical professionals thoroughly examine these pre-corrected labels along with the original GTs for the remaining structures. The review process involves independent assessment of all 104 anatomical structures, classifying each annotation as reliable or unreliable with documented error descriptions.

The review process identified several recurrent types of annotation errors in the original TotalSegmentator GT (Supplementary Figure A.7):

*Mislabeling between adjacent structures:* For example, problems like “parts of the small intestine appear labeled as colon”, or vice versa. Medical professionals often highlight cases of “overlap between liver, spleen and stomach”, where portions of one organ show incorrect attribution to adjacent ones. Similar mislabeling exists between hip and femur regions.

*Missing segments or incomplete labels:* Many structures show incomplete GT annotations. This issue is particularly common in ribs, where “costovertebral junction missing” is a frequent comment. Additional examples include “medial part missing” for gluteal muscles, “short segment in the mid esophagus not labeled”, and incomplete annotations of gallbladder, adrenal glands, and pancreas.

*Over-segmentation and unrelated structure inclusion:* The urinary bladder labels often extend beyond their boundaries into the perivesical region or prostate. Similarly, parts of lung tissue appear within heart chamber labels.

*Boundary inaccuracies:* The GT annotations show imprecise delineation of structural borders throughout various anatomical regions.

Following this detailed review, we establish a curated GT dataset. For the final quantitative evaluation of our model’s performance on these 65 test images, we exclude structures in test images where medical professionals have flagged specific anatomical structures as unreliable. This curation process ensures that our reported model performance is validated only on accurate and reliable reference annotations, providing a more truthful assessment of the model capabilities.

## Data availability

Our CADS-dataset, comprising paired CT volumes and curated whole-body annotations, is publicly accessible via <https://huggingface.co/datasets/mrmrx/CADS-dataset>.

## Code availability

Our trained models and codebase are publicly available for further research at <https://github.com/murong-xu/CADS>. Additionally, we provide a 3D Slicer tool, which can be downloaded with detailed user instructions available at <https://github.com/murong-xu/SlicerCADS>.



## Author contributions

M.X., T.A., F.Na., and B.M. designed the study. M.X., T.A., F.Na., I.E.H., and S.E. were responsible for data collection. M.X., T.A., and F.Na. were responsible for data analysis, model construction, and model validation. M.X. took the lead on manuscript writing, with contributions from T.A. M.X., E.d.l.R. and J.D. contributed to figure preparation. M.X. were responsible for the software plugin development. M.F., S.M.C., and S.T.L. contributed to the external evaluation. I.E.H., S.E., and J.C.P. managed data anonymization and annotation. I.E.H., S.E., M.-A.W., G.L., M.K.O., and J.S.K. contributed to the new data release. S.B., G.B., J.H., F.Ne., and R.H. contributed to data processing. S.S., B.W., and A.S. contributed to label quality optimization. N.M. and S.K. contributed to label quality review. R.G. and H.M. contributed to model inference optimization. A.F., R.K., J.W., E.d.l.R., and S.E.C. provided knowledge support. B.M. supervised the all study. All authors contributed to writing and revising the manuscript.

## Acknowledgments

This research was supported by the Helmut Horten Foundation, the Comprehensive Cancer Center Zurich (C3Z Precision Oncology Funding Program, OMD-ZH project), and the European Research Council (ERC) under the European Union’s Horizon 2020 research and innovation programme (101045128 — iBack-epic — ERC-2021-COG).

We extend our sincere gratitude to all data providers and original authors of the public datasets integrated into the CADS-dataset. While these datasets are publicly available for academic research, we emphasize that we are not the original authors of these source datasets. Users of the CADS-dataset must comply with the individual licenses and terms of use for each source dataset, and properly cite the original works. For detailed information about individual dataset licenses, please refer to our dataset documentation and the original publications cited within this paper.

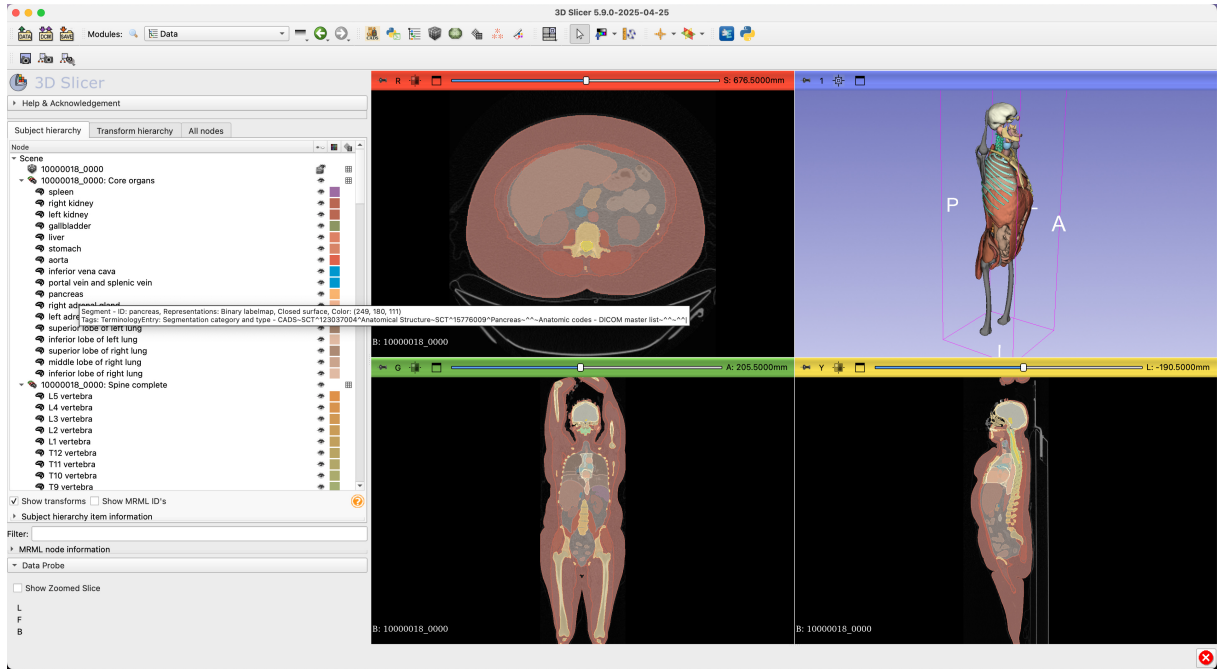
The three-dimensional visualizations presented in Figures 1, 5, and A.6 were generated using 3D Slicer [38].

## Methods References

92. Y. He, P. Guo, Y. Tang, A. Myronenko, V. Nath, Z. Xu, D. Yang, C. Zhao, B. Simon, M. Belue, *et al.*, “Vista3d: Versatile imaging segmentation and annotation model for 3D computed tomography,” *arXiv preprint arXiv:2406.05285*, 2024.
93. S. Wang, C. Li, R. Wang, Z. Liu, M. Wang, H. Tan, Y. Wu, X. Liu, H. Sun, R. Yang, *et al.*, “Annotation-efficient deep learning for automatic medical image segmentation,” *Nature communications*, vol. 12, no. 1, p. 5915, 2021.
94. X. Zhai, A. Kolesnikov, N. Houlsby, and L. Beyer, “Scaling vision transformers,” in *Proceedings of the IEEE/CVF conference on computer vision and pattern recognition*, pp. 12104–12113, 2022.
95. Y. Zhang, J. Gao, Z. Tan, L. Zhou, K. Ding, M. Zhou, S. Zhang, and D. Wang, “Data-centric foundation models in computational healthcare: A survey,” *arXiv preprint arXiv:2401.02458*, 2024.
96. C. Olivier, S. Bernhard, and Z. Alexander, “Semi-supervised learning,” *IEEE Transactions on Neural Networks*, vol. 20, no. 3, pp. 542–542, 2006.
97. O. Puonti, K. Van Leemput, G. B. Saturnino, H. R. Siebner, K. H. Madsen, and A. Thielscher, “Accurate and robust whole-head segmentation from magnetic resonance images for individualized head modeling,” *Neuroimage*, vol. 219, p. 117044, 2020.
98. B. B. Avants, N. Tustison, G. Song, *et al.*, “Advanced normalization tools (ants),” *Insight j*, vol. 2, no. 365, pp. 1–35, 2009.
99. J. Zhang, G. Wang, H. Xie, S. Zhang, N. Huang, S. Zhang, and L. Gu, “Weakly supervised vessel segmentation in x-ray angiograms by self-paced learning from noisy labels with suggestive annotation,” *Neurocomputing*, vol. 417, pp. 114–127, 2020.
100. D. Kwon and S. Kwak, “Semi-supervised semantic segmentation with error localization network,” in *Proceedings of the IEEE/CVF Conference on Computer Vision and Pattern Recognition*, pp. 9957–9967, 2022.
101. H. Guan and M. Liu, “Domain adaptation for medical image analysis: a survey,” *IEEE Transactions on Biomedical Engineering*, vol. 69, no. 3, pp. 1173–1185, 2021.
102. Q. Yu, N. Xi, J. Yuan, Z. Zhou, K. Dang, and X. Ding, “Source-free domain adaptation for medical image segmentation via prototype-anchored feature alignment and contrastive learning,” in *International Conference on Medical Image Computing and Computer-Assisted Intervention*, pp. 3–12, Springer, 2023.
103. L. Liu, Z. Zhang, S. Li, K. Ma, and Y. Zheng, “S-cuda: self-cleansing unsupervised domain adaptation for medical image segmentation,” *Medical Image Analysis*, vol. 74, p. 102214, 2021.
104. M. Maynord, M. M. Farhangi, C. Fermüller, Y. Aloimonos, G. Levine, N. Petrick, B. Sahiner, and A. Pezeshk, “Semi-supervised training using cooperative labeling of weakly annotated data for nodule detection in chest CT,” *Medical Physics*, vol. 50, no. 7, pp. 4255–4268, 2023.



105. A.-M. Rickmann, M. Xu, T. N. Wolf, O. Kovalenko, and C. Wachinger, “Halos: Hallucination-free organ segmentation after organ resection surgery,” in *International Conference on Information Processing in Medical Imaging*, pp. 667–678, Springer, 2023.
106. X. Luo, Z. Li, S. Zhang, W. Liao, and G. Wang, “Rethinking abdominal organ segmentation (raos) in the clinical scenario: A robustness evaluation benchmark with challenging cases,” *arXiv preprint arXiv:2406.13674*, 2024.
107. B. Wittmann, Y. Wattenberg, T. Amiranashvili, S. Shit, and B. Menze, “vesselfm: A foundation model for universal 3d blood vessel segmentation,” *arXiv preprint arXiv:2411.17386*, 2024.
108. Z. Li, K. Kamnitsas, and B. Glocker, “Analyzing overfitting under class imbalance in neural networks for image segmentation,” *IEEE transactions on medical imaging*, vol. 40, no. 3, pp. 1065–1077, 2020.
109. Z. Zhong, J. Cui, Y. Yang, X. Wu, X. Qi, X. Zhang, and J. Jia, “Understanding imbalanced semantic segmentation through neural collapse,” in *Proceedings of the IEEE/CVF conference on computer vision and pattern recognition*, pp. 19550–19560, 2023.
110. C. Huang, Y. Li, C. C. Loy, and X. Tang, “Learning deep representation for imbalanced classification,” in *Proceedings of the IEEE conference on computer vision and pattern recognition*, pp. 5375–5384, 2016.
111. F. Isensee, T. Wald, C. Ulrich, M. Baumgartner, S. Roy, K. Maier-Hein, and P. F. Jaeger, “nnu-net revisited: A call for rigorous validation in 3d medical image segmentation,” *arXiv preprint arXiv:2404.09556*, 2024.



**Supplementary Fig. A.6: CADS-model integration in 3D Slicer.** Implementation of the CADS-model as a user-friendly plugin for the widely-used 3D Slicer platform [38]. The interface demonstrates seamless integration of our whole-body segmentation capabilities, with anatomical structures coded using standardized SNOMED-CT medical terminology and visualization across axial, sagittal, and coronal views. This implementation provides clinicians and researchers with immediate access to advanced AI-powered segmentation within a familiar clinical workflow environment.

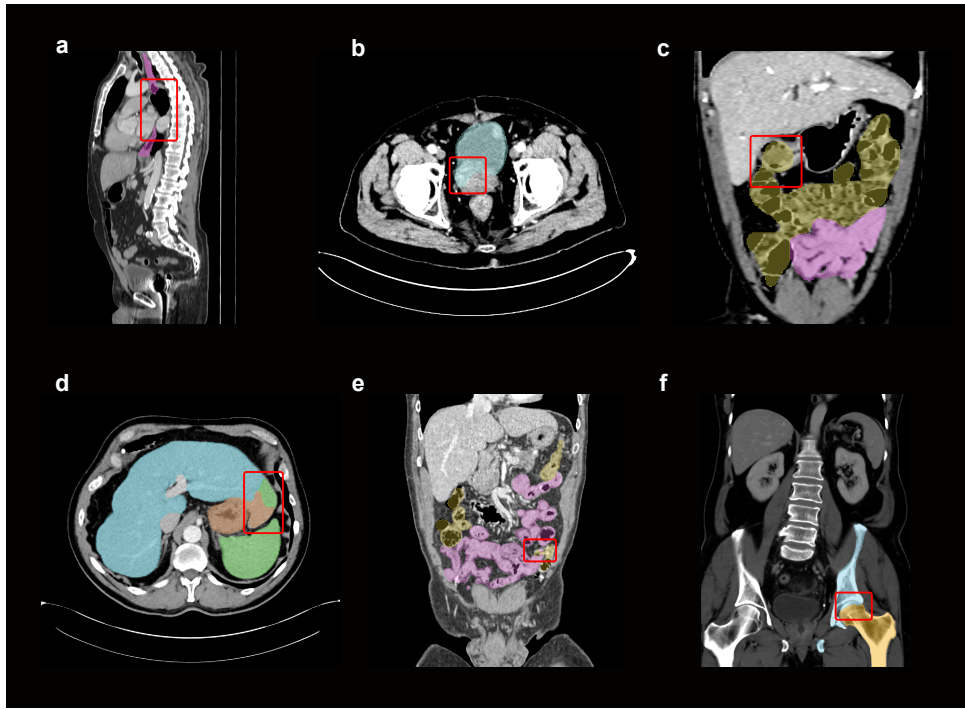
	Spleen	Kidney R	Kidney L	Gallbladder	Liver	Stomach	Aorta	Inferior vena cava	Portal and splenic vein
# Occurrence	21,097	18,482	20,110	15,429	21,191	21,118	21,342	21,046	20,602
Med. Vol.	59,202	22,472	24,004	3,633	430,341	72,764	58,888	13,554	3,603
	Pancreas	Adrenal Gland R	Adrenal Gland L	Lung Upper Lobe L	Lung Lower Lobe L	Lung Upper Lobe R	Lung Middle Lobe R	Lung Lower Lobe R	Vertebrae L5
#Occurrence	20,641	20,652	20,406	21,011	21,137	18,241	20,725	21,379	5,413
Med. Vol.	17,155	960	1,114	307,385	275,330	281,021	109,989	304,069	17,458
	Vertebrae L4	Vertebrae L3	Vertebrae L2	Vertebrae L1	Vertebrae T12	Vertebrae T11	Vertebrae T10	Vertebrae T9	Vertebrae T8
#Occurrence	6,519	8,733	15,049	19,730	20,811	20,891	20,732	20,352	19,667
Med. Vol.	17,874	16,921	13,274	13,718	13,119	12,054	11,152	9,930	8,931
	Vertebrae T7	Vertebrae T6	Vertebrae T5	Vertebrae T4	Vertebrae T3	Vertebrae T2	Vertebrae T1	Vertebrae C7	Vertebrae C6
#Occurrence	18,750	17,932	17,475	17,332	17,318	17,289	17,255	16,744	9,792
Med. Vol.	8,357	7,649	7,195	6,738	6,426	6,650	6,165	2,601	570
	Vertebrae C5	Vertebrae C4	Vertebrae C3	Vertebrae C2	Vertebrae C1	Esophagus	Trachea	Heart myocardium	Heart atrium L
#Occurrence	3,255	1,167	905	1,276	1,249	21,030	17,547	20,619	20,352
Med. Vol.	499	3,111	3,349	4,007	3,317	9,350	9,773	31,054	17,734
	Heart ventricle L	Heart atrium R	Heart ventricle R	Pulmonary artery	Brain	Iliac artery L	Iliac artery R	Iliac vena L	Iliac vena R
#Occurrence	20,574	20,516	20,684	17,701	1,268	6,803	6,240	5,703	5,901
Med. Vol.	29,043	22,501	38,916	18,132	358,424	2,701	3,160	6,974	5,545
	Small bowel	Duodenum	Colon	Urinary bladder	Face	Humerus L	Humerus R	Scapula L	Scapula R
#Occurrence	17,026	17,601	20,347	4,022	4,793	16,344	16,629	18,569	18,568
Med. Vol.	36,292	6,784	54,292	41,437	47	9,753	10,476	28,550	27,772

	Clavicula L	Clavicula R	Femur L	Femur R	Hip L	Hip R	Sacrum	Gluteus maximus L	Gluteus maximus R
#Occurrence	17,302	17,310	3,628	3,573	5,290	5,272	4,494	4,122	4,188
Med. Vol.	6,226	6,731	48,277	48,168	96,869	97,104	62,408	131,518	133,948
	Gluteus medius L	Gluteus medius R	Gluteus minimus L	Gluteus minimus R	Autoch- thon L	Autoch- thon R	Iliopsoas L	Iliopsoas R	Rib-1 L
#Occurrence	4,776	4,803	3,784	3,810	21,344	21,343	16,617	17,524	17,318
Med. Vol.	63,677	62,294	16,844	17,984	86,627	85,689	3,361	2,838	2,850
	Rib-2 L	Rib-3 L	Rib-4 L	Rib-5 L	Rib-6 L	Rib-7 L	Rib-8 L	Rib-9 L	Rib-10 L
#Occurrence	17,363	17,483	18,180	19,522	20,547	20,776	20,870	20,893	20,897
Med. Vol.	3,374	3,992	4,910	5,405	5,947	6,218	5,471	4,948	3,963
	Rib-11 L	Rib-12 L	Rib-1 R	Rib-2 R	Rib-3 R	Rib-4 R	Rib-5 R	Rib-6 R	Rib-7 R
#Occurrence	20,862	19,871	17,316	17,369	17,487	18,074	19,445	20,488	20,720
Med. Vol.	2,313	838	2,883	3,394	4,034	5,122	5,661	6,046	6,371
	Rib-8 R	Rib-9 R	Rib-10 R	Rib-11 R	Rib-12 R	Spinal canal	Larynx	Heart	Bowel bag
#Occurrence	20,825	20,856	20,879	20,848	19,790	21,939	16,531	20,805	21,367
Med. Vol.	5,648	5,078	3,813	2,206	759	16,463	751	137,449	186,750
	Sigmoid	Rectum	Prostate	Seminal vesicle	Mammary gland L	Mammary gland R	Sternum	Psoas major R	Psoas major L
#Occurrence	6,263	5,850	3,618	3,619	10,784	9,602	20,786	20,251	20,218
Med. Vol.	13,524	9,185	6,225	2,145	94,565	119,226	15,512	2,601	2,999
	Rectus abdominis R	Rectus abdominis L	White matter	Gray matter	CSF	Scalp	Eye balls	Compact bone	Spongy bone
#Occurrence	21,059	21,054	3,336	1,729	2,612	4,622	1,071	4,952	3,578
Med. Vol.	13,604	14,002	1,106	163,903	1,546	12,311	4,283	861	892
	Blood	Head muscles	Carotid artery L	Carotid artery R	Arytenoids	Mandible	Brainstem	Buccal mucosa	Oral cavity
#Occurrence	2,319	1,083	17,746	16,281	4,522	5,080	1,234	1,108	2,244
Med. Vol.	2,125	503	510	175	60	2,217	5,551	761	4,116
	Cochlea L	Cochlea R	Cricophary -ngeal inlet	Cervical esophagus	Anterior eyeball L	Anterior eyeball R	Posterior eyeball L	Posterior eyeball R	Lacrimal gland L
#Occurrence	1,068	1,104	10,050	16,216	403	397	1,035	945	771
Med. Vol.	33	39	508	549	239	240	731	457	50
	Lacrimal gland R	Submandi- bular gland L	Submandi- bular gland R	Thyroid	Larynx- glottis	Larynx- supraglottic	Lips	Optic chiasm	Optic nerve L
#Occurrence	711	1,350	1,418	17,074	7,573	3,951	1,740	1,019	1,030
Med. Vol.	57	904	782	3,424	566	1,138	2,231	72	152
	Optic nerve R	Parotid gland L	Parotid gland R	Pituitary gland	Subcuta- -neous tissue	Muscle	Abdominal cavity	Thoracic cavity	Bones
#Occurrence	1,031	1,301	1,313	1,045	22,022	22,022	21,990	22,001	22,022
Med. Vol.	157	4,629	4,738	96	1,410,735	1,609,604	1,280,645	1,329,453	590,596
	Glands	Pericardium	Breast implant	Mediastinum	Spinal cord				
#Occurrence	18,294	21,283	3,341	21,419	21,703				
Med. Vol.	2,879	205,442	75	175,396	17,388				

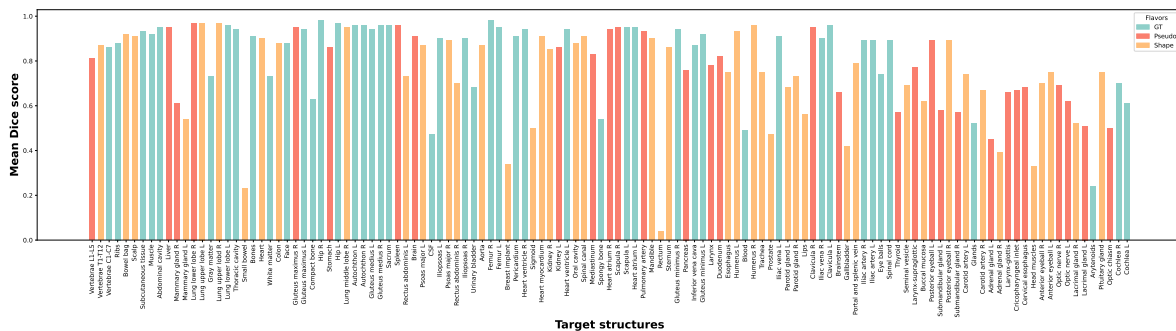
Supplementary Table A.5: **Summary statistics for segmentation targets in the CADS-dataset.** This table details the 167 segmentation targets within our CADS-dataset (derived from 22,022 images). For each target, the table lists its Occurrence frequency across the dataset and its median volume.

	Description	Targets
1	Major abdominal organs, primary thoracic organs (lungs), and major abdominal vasculature.	Spleen, Kidney (R/L), Liver, Lungs (lobes), Stomach, Aorta, Pancreas, Adrenal glands (R/L).
2	Complete set of individual vertebrae from cervical to lumbar regions.	Vertebra L1-L5, T1-T12, C1-C7.
3	Various thoracic and abdominal organs (including heart components, GI tract), brain, major pelvic vessels, and face.	Esophagus, Trachea, Myocardium, Heart atria/ventricles, Pulmonary artery, Brain, Iliac arteries/veins, Small intestine, Colon, Urinary bladder, Face.
4	Major bones of the appendicular skeleton (upper/lower limbs, shoulder/pelvic girdles), sacrum, and associated large muscle groups.	Humerus (L/R), Scapula (L/R), Femur (L/R), Hip (L/R), Sacrum, Gluteus muscles (maximus, medius, minimus L/R), Iliopsoas (L/R).
5	Complete set of individual ribs, both left and right.	Rib 1-12 L/R.
6	Miscellaneous structures including spinal canal, larynx, whole heart, specific lower GI/pelvic organs, mammary glands, sternum, and anterior abdominal wall muscles.	Spinal canal, Larynx, Heart (overall), Sigmoid colon, Rectum, Prostate, Mammary glands (L/R), Sternum, Psoas major (L/R), Rectus abdominis (L/R).
7	Intracranial tissues and fluids, scalp, eyeball, general bone tissue classifications, and muscles of the head.	White matter, Gray matter, Cerebrospinal fluid, Scalp, Eyeball, Compact bone, Spongy bone, Muscle of head.
8	Detailed head and neck anatomical structures, including specific arteries, cartilages, components of the aerodigestive tract, sensory organs (eye, ear), and various glands.	Carotid artery (L/R), Mandible, Brainstem, Oral cavity, Cochlea (L/R), Cervical esophagus, Eyeball segments (anterior/posterior L/R), Lacrimal/Submandibular/Parotid glands, Thyroid, Optic nerves (L/R), Pituitary.
9	General tissue types, major body cavities, broad anatomical categories (bones, glands as a whole), and specific structures like pericardium and spinal cord.	Subcutaneous tissue, Muscle (general), Abdominal cavity, Thoracic cavity, Bones (general), Gland structure (general), Pericardium, Spinal cord.

Supplementary Table A.2: **Overview of target structures for each CADS segmentation model.** This table outlines the nine model groups used for segmenting 167 anatomical structures. Each group is described by its general anatomical focus and a list of representative target structures



**Supplementary Fig. A.7: Ground truth annotation inconsistencies in the TotalSegmentator dataset highlighting the need for expert review.** This figure presents examples of unreliable ground truth annotations identified within the TotalSegmentator dataset. Such inaccuracies can significantly impact the training and evaluation of automated segmentation models. The visualized annotation issues include: (a) Mid-esophagus: Omission of the label for a short segment. (b) Urinary bladder: Label over-extension into adjacent anatomical structures, such as the perivesical space or the prostate. (c) Small intestine: Misclassification of segments as colon. (d) Liver: Portions of liver tissue mislabelled as stomach, and other distinct portions as spleen. (e) Small intestine (regional): Misclassification of segments near the stomach and sigmoid colon as colon. (f) Left hip and femur: Suboptimal labeling at their junction, characterized by minimal overlap of the left hip's ground truth label, leading to an inaccurate boundary.



**Supplementary Fig. A.8: Model flavor selection for assembling 167 whole-body structures in CADS-dataset**

**Supplementary Table A.12: Comparison of CADS-model (CADS) and TotalSegmentator (TotalSeg) performance across 167 structures.** Segmentation performance is compared using Dice and HD95 metrics. For each structure, the results are quantified by the mean  $\pm$  standard deviation, median, and 95% confidence interval of the scores. Empty TotalSeg entries indicate structures uniquely segmented by CADS-model. Green stars (\*) indicate statistically significant improvements ( $p < 0.05$ ).

Organ	CADS (Dice)	TotalSeg (Dice)	CADS (HD95)	TotalSeg (HD95)
-------	----------------	--------------------	----------------	--------------------

*Continued on next page*



Organ	CADS (Dice)	TotalSeg (Dice)	CADS (HD95)	TotalSeg (HD95)
<b>Digestive System</b>				
Gallbladder	72.98±28.87 83.99 (67.01, 78.41)	74.08±28.80 <sup>*</sup> 85.35 (68.00, 79.60)	46.87±218.36 3.67 (8.33, 95.29)	46.12±218.41 3.51 (7.58, 95.15)
Liver	96.59±2.00 <sup>*</sup> 96.94 (96.38, 96.78)	96.47±1.93 96.74 (96.27, 96.65)	3.50±3.46 <sup>*</sup> 3.00 (3.18, 3.86)	3.68±3.55 3.00 (3.36, 4.05)
Stomach	91.80±11.26 93.62 (89.13, 93.73)	91.97±11.62 <sup>*</sup> 93.88 (89.14, 93.97)	6.77±11.90 3.00 (4.51, 9.56)	8.54±19.88 3.00 (4.98, 13.23)
Pancreas	79.83±17.96 <sup>*</sup> 85.32 (77.63, 81.90)	79.38±18.40 84.72 (77.12, 81.51)	7.29±10.84 <sup>*</sup> 3.67 (6.08, 8.68)	7.55±10.89 4.24 (6.35, 8.90)
Esophagus	84.91±9.72 88.22 (82.98, 86.73)	86.58±10.39 <sup>*</sup> 88.40 (84.54, 88.57)	4.12±5.69 1.50 (3.11, 5.28)	4.02±5.32 1.50 (3.11, 5.14)
Small intestine	78.79±26.15 92.43 (66.92, 88.78)	76.92±30.92 94.10 (63.23, 88.75)	19.50±35.31 3.00 (6.53, 36.08)	25.26±42.89 1.50 (9.12, 45.01)
Duodenum	78.54±15.34 80.13 (74.98, 81.76)	79.99±15.18 <sup>*</sup> 81.73 (76.60, 83.17)	6.72±6.91 4.74 (5.28, 8.33)	6.44±6.73 4.74 (5.08, 8.05)
Colon	93.52±3.72 94.87 (91.87, 95.02)	94.91±2.83 <sup>*</sup> 95.60 (93.67, 96.06)	4.31±4.82 2.12 (2.45, 6.59)	3.10±2.68 1.50 (2.07, 4.37)
Colostomy bag	92.39±2.16 93.40 (90.84, 93.82)	— — —	10.58±3.71 9.75 (8.13, 13.21)	— — —
Sigmoid colon	66.71±19.01 72.10 (52.96, 78.95)	— — —	27.94±15.14 29.81 (17.46, 38.34)	— — —
Rectum	66.23±19.83 69.33 (54.91, 75.70)	— — —	21.71±14.10 15.94 (14.68, 29.49)	— — —
Oral cavity	89.58±3.13 89.29 (87.82, 91.29)	— — —	4.26±1.45 3.67 (3.47, 5.09)	— — —
Cricopharyngeus	69.80±5.94 71.15 (66.30, 72.91)	— — —	3.05±0.89 3.00 (2.56, 3.56)	— — —
Cervical esophagus	64.79±10.05 66.27 (58.52, 69.98)	— — —	5.02±2.85 3.93 (3.62, 6.82)	— — —
<b>Reproductive System</b>				
Prostate	73.87±17.79 79.57 (66.89, 79.31)	69.87±23.80 77.71 (60.38, 77.33)	9.36±11.51 6.00 (6.14, 13.99)	72.75±202.46 6.17 (6.72, 158.06)
Seminal vesicle	76.10±8.96 79.51 (67.10, 83.58)	— — —	4.00±1.61 3.75 (2.56, 5.52)	— — —
Mammary gland L	68.33±25.10 76.52 (41.18, 88.05)	— — —	33.71±30.51 19.64 (12.83, 68.66)	— — —

Continued on next page

Organ	CADS (Dice)	TotalSeg (Dice)	CADS (HD95)	TotalSeg (HD95)
Mammary gland R	68.86±24.20 78.63 (44.06, 88.59)	— — —	34.26±22.29 26.07 (16.18, 57.53)	— — —
<b>Nervous System</b>				
Brain	94.37±10.76 <sup>*</sup> 97.49 (91.09, 96.96)	92.68±13.59 97.29 (88.54, 95.95)	2.58±4.21 1.50 (1.65, 3.93)	2.96±4.53 1.50 (1.89, 4.37)
Spinal canal	91.70±1.47 91.87 (90.62, 92.66)	— — —	1.50±0.00 1.50 (1.50, 1.50)	— — —
White matter	78.53±4.97 80.52 (75.55, 81.39)	— — —	3.03±0.91 3.00 (2.53, 3.58)	— — —
Gray matter	76.76±4.57 78.35 (73.97, 79.37)	— — —	2.70±0.71 2.60 (2.32, 3.17)	— — —
Cerebrospinal fluid	53.72±7.13 55.96 (49.36, 57.62)	— — —	6.35±1.40 6.18 (5.62, 7.24)	— — —
Brainstem	79.94±10.12 <sup>*</sup> 82.96 (74.40, 84.28)	56.21±9.45 55.60 (51.80, 61.00)	4.53±2.26 <sup>*</sup> 4.09 (3.50, 5.71)	31.92±8.21 32.66 (27.64, 35.46)
Optic chiasm	46.89±13.13 46.94 (38.99, 54.41)	— — —	2.89±1.11 2.12 (2.29, 3.62)	— — —
Optic nerve L	60.69±20.15 <sup>*</sup> 69.90 (47.81, 69.86)	50.87±19.18 54.71 (39.15, 60.51)	71.78±230.89 <sup>*</sup> 2.12 (1.80, 211.21)	81.24±228.07 13.53 (10.75, 219.58)
Optic nerve R	65.29±12.12 <sup>*</sup> 66.13 (58.04, 71.51)	49.99±16.98 51.62 (39.29, 58.11)	2.14±0.81 <sup>*</sup> 2.12 (1.76, 2.66)	80.86±228.17 12.28 (10.95, 218.98)
Spinal cord	88.66±13.18 <sup>*</sup> 92.07 (86.37, 90.62)	83.88±12.63 86.90 (81.72, 85.75)	3.38±3.78 <sup>*</sup> 1.50 (2.81, 4.02)	6.71±7.12 3.00 (5.64, 7.89)
<b>Cardiovascular System</b>				
Aorta	92.16±8.35 <sup>*</sup> 93.63 (90.56, 93.39)	91.24±8.47 93.30 (89.69, 92.49)	5.14±13.92 <sup>*</sup> 1.50 (3.12, 7.74)	6.90±17.87 2.12 (4.23, 10.20)
Inferior vena cava	88.75±8.01 90.82 (87.03, 90.39)	89.66±7.58 <sup>*</sup> 92.03 (88.02, 91.24)	3.09±1.98 2.36 (2.70, 3.52)	3.08±2.15 2.36 (2.64, 3.55)
Portal vein and splenic vein	85.73±8.22 89.52 (83.05, 88.19)	87.94±8.07 <sup>*</sup> 91.67 (85.28, 90.30)	2.44±1.73 1.50 (1.95, 3.03)	2.13±1.42 <sup>*</sup> 1.50 (1.74, 2.61)
Myocardium	94.53±2.31 <sup>*</sup> 95.03 (93.68, 95.27)	85.33±2.88 85.10 (84.36, 86.32)	1.57±0.23 <sup>*</sup> 1.50 (1.50, 1.66)	2.50±0.60 2.12 (2.31, 2.72)
Atrium L	95.42±5.49 <sup>*</sup> 97.53 (93.61, 96.83)	89.26±9.56 92.93 (86.21, 91.85)	1.71±0.56 <sup>*</sup> 1.50 (1.56, 1.89)	3.99±8.20 2.60 (2.49, 6.67)

Continued on next page

Organ	CADS (Dice)	TotalSeg (Dice)	CADS (HD95)	TotalSeg (HD95)
Heart ventricle L	96.38±3.35 <sup>*</sup> 97.24 (95.28, 97.22)	91.11±4.36 92.14 (89.68, 92.21)	1.90±1.74 <sup>*</sup> 1.50 (1.56, 2.48)	3.21±2.15 3.00 (2.76, 3.94)
Atrium R	95.68±3.22 <sup>*</sup> 96.63 (94.56, 96.55)	87.35±9.31 89.69 (84.06, 89.76)	1.91±0.95 <sup>*</sup> 1.50 (1.66, 2.23)	5.50±9.11 3.67 (3.65, 8.62)
Heart ventricle R	96.58±1.45 <sup>*</sup> 96.88 (96.14, 96.98)	90.94±2.15 91.30 (90.32, 91.56)	1.75±0.50 <sup>*</sup> 1.50 (1.62, 1.91)	3.54±1.31 3.35 (3.19, 3.94)
Pulmonary artery	95.28±2.45 <sup>*</sup> 96.00 (94.32, 96.03)	87.76±14.56 91.80 (81.83, 91.80)	1.52±0.11 <sup>*</sup> 1.50 (1.50, 1.56)	4.92±12.33 2.12 (2.13, 9.90)
Common iliac artery L	92.89±4.47 94.29 (91.37, 94.08)	94.16±3.53 <sup>*</sup> 95.43 (93.00, 95.18)	1.74±0.73 1.50 (1.53, 1.98)	1.84±1.57 1.50 (1.53, 2.38)
Common iliac artery R	91.45±11.40 94.20 (87.35, 94.11)	93.73±7.91 <sup>*</sup> 95.76 (90.81, 95.57)	2.63±4.75 1.50 (1.53, 4.31)	2.14±3.39 <sup>*</sup> 1.50 (1.43, 3.34)
Common iliac vein L	92.72±10.29 95.28 (89.03, 94.97)	93.33±9.78 <sup>*</sup> 96.06 (89.83, 95.51)	2.38±4.42 1.50 (1.55, 3.90)	1.93±1.72 1.50 (1.55, 2.55)
Common iliac vein R	93.13±4.62 94.33 (91.56, 94.36)	93.86±3.62 <sup>*</sup> 94.84 (92.68, 94.87)	2.46±4.72 1.50 (1.52, 4.08)	2.20±2.44 1.50 (1.53, 3.03)
Heart	89.72±2.94 <sup>*</sup> 89.56 (87.75, 91.78)	75.90±3.50 76.34 (73.45, 78.30)	10.59±5.14 <sup>*</sup> 9.47 (7.15, 14.35)	45.26±11.04 48.98 (37.05, 52.46)
Blood	55.80±11.95 61.33 (48.56, 62.51)	— — —	3.84±1.75 3.35 (2.89, 5.01)	— — —
Carotid artery L	74.25±6.07 <sup>*</sup> 75.15 (70.60, 77.51)	65.37±8.93 65.28 (60.18, 70.11)	5.11±7.68 <sup>*</sup> 2.12 (2.01, 10.05)	12.50±8.85 8.78 (8.01, 17.90)
Carotid artery R	75.33±4.36 <sup>*</sup> 75.76 (72.68, 77.64)	64.25±6.12 65.18 (60.91, 67.64)	3.15±1.67 <sup>*</sup> 2.90 (2.24, 4.13)	12.89±3.71 12.45 (10.93, 15.14)
Pericardium	92.47±13.22 96.04 (90.20, 94.40)	— — —	3.76±4.78 3.00 (3.04, 4.56)	— — —
<b>Respiratory System</b>				
Upper lobe of lung L	97.51±5.88 99.34 (95.63, 98.78)	98.20±5.05 <sup>*</sup> 99.51 (96.58, 99.20)	2.38±3.95 1.50 (1.56, 3.65)	1.63±3.84 <sup>*</sup> 1.50 (0.89, 2.85)
Lower lobe of lung L	98.20±2.54 99.00 (97.44, 98.81)	98.83±1.29 <sup>*</sup> 99.22 (98.45, 99.14)	3.72±14.73 1.50 (1.39, 8.11)	1.35±1.50 <sup>*</sup> 1.50 (0.99, 1.79)
Upper lobe of lung R	97.85±4.68 99.08 (96.21, 98.94)	98.17±3.27 <sup>*</sup> 99.26 (97.10, 99.04)	2.69±5.34 1.50 (1.57, 4.55)	1.92±1.87 1.50 (1.42, 2.54)
Middle lobe of lung R	95.65±8.37 98.14 (92.95, 97.56)	97.30±3.78 <sup>*</sup> 98.59 (96.15, 98.23)	2.64±3.16 1.50 (1.90, 3.67)	2.12±1.89 <sup>*</sup> 1.50 (1.66, 2.70)

Continued on next page

Organ	CADS (Dice)	TotalSeg (Dice)	CADS (HD95)	TotalSeg (HD95)
Lower lobe of lung R	98.40±2.25	98.58±2.06 <sup>*</sup>	1.62±2.07	1.67±2.69
	99.34	99.41	1.50	1.50
	(97.78, 98.95)	(98.00, 99.07)	(1.16, 2.23)	(1.10, 2.47)
Trachea	86.06±10.92	86.65±12.60	11.69±11.46	12.07±12.45
	92.97	95.75	1.50	1.50
	(83.55, 88.52)	(83.68, 89.43)	(9.11, 14.36)	(9.23, 14.93)
Larynx	83.50±2.63	—	4.55±0.94	—
	82.82	—	4.50	—
	(81.37, 86.06)	—	(3.71, 5.39)	—
Arytenoid cartilage	57.98±11.63	—	2.42±1.11	—
	58.85	—	2.12	—
	(50.45, 63.54)	—	(1.90, 3.13)	—
Glottis	74.01±7.78	—	2.40±1.32	—
	74.34	—	1.81	—
	(69.38, 78.36)	—	(1.78, 3.23)	—
Supraglottis	83.11±5.95	—	2.29±1.23	—
	83.77	—	2.12	—
	(79.31, 86.09)	—	(1.76, 3.09)	—
<b>Lymphatic and Immune System</b>				
Spleen	95.94±3.78	95.84±4.46	2.45±4.81 <sup>*</sup>	2.57±5.66
	96.78	96.82	1.50	1.50
	(95.47, 96.36)	(95.26, 96.31)	(1.97, 3.11)	(2.03, 3.34)
<b>Urinary System</b>				
Kidney R	92.66±11.08	92.84±10.95	4.63±5.45	5.68±15.82
	95.25	94.97	2.12	2.12
	(90.59, 94.28)	(90.74, 94.44)	(3.76, 5.61)	(3.72, 8.93)
Kidney L	91.32±14.92	91.52±14.63	5.35±8.45	5.49±9.52
	94.77	94.77	2.12	1.50
	(88.49, 93.64)	(88.80, 93.75)	(4.07, 6.93)	(4.04, 7.26)
Urinary bladder	83.53±15.40 <sup>*</sup>	82.50±17.30	9.16±12.05	11.30±30.07
	87.64	87.15	5.09	4.97
	(80.70, 86.07)	(79.33, 85.30)	(7.20, 11.33)	(7.50, 17.46)
<b>Skeletal System</b>				
Vertebra L5	89.52±16.01	90.73±14.59 <sup>*</sup>	2.82±5.60	2.42±4.83
	92.91	93.51	1.50	1.50
	(85.75, 92.51)	(87.18, 93.30)	(1.82, 4.16)	(1.59, 3.58)
Vertebra L4	89.73±16.77	90.11±16.98 <sup>*</sup>	2.73±5.39	2.83±6.21
	93.95	94.11	1.50	1.50
	(85.67, 92.83)	(86.03, 93.33)	(1.70, 4.00)	(1.64, 4.35)
Vertebra L3	91.02±11.19	91.66±9.67 <sup>*</sup>	3.19±6.00	2.99±5.97
	94.02	94.33	1.50	1.50
	(88.30, 92.94)	(89.40, 93.40)	(2.06, 4.58)	(1.84, 4.32)
Vertebra L2	91.85±7.59	92.04±7.10 <sup>*</sup>	2.40±4.03	2.65±5.19
	93.60	93.64	1.50	1.50
	(90.04, 93.22)	(90.35, 93.32)	(1.67, 3.36)	(1.71, 3.85)
Vertebra L1	91.56±11.09	91.95±10.10	2.29±4.07	2.14±3.35
	93.67	93.88	1.50	1.50
	(88.93, 93.37)	(89.56, 93.55)	(1.56, 3.27)	(1.55, 2.95)
Vertebra T12	92.66±3.47	92.27±5.44	1.65±0.65	2.00±2.99
	93.64	93.67	1.50	1.50
	(91.88, 93.33)	(91.03, 93.26)	(1.53, 1.80)	(1.56, 2.73)

Continued on next page

Organ	CADS (Dice)	TotalSeg (Dice)	CADS (HD95)	TotalSeg (HD95)
Vertebra T11	92.13±5.57 93.24 (90.85, 93.13)	91.44±10.41 93.27 (88.86, 93.05)	1.81±1.73 1.50 (1.55, 2.24)	2.14±3.49 1.50 (1.56, 2.96)
Vertebra T10	91.33±10.14 93.14 (88.78, 92.83)	90.38±13.37 93.03 (87.12, 92.71)	1.86±2.36 1.50 (1.53, 2.44)	2.20±3.44 1.50 (1.55, 3.02)
Vertebra T9	90.37±11.49 <sup>*</sup> 93.12 (87.34, 92.36)	89.62±12.73 92.86 (86.21, 92.02)	2.10±3.11 1.50 (1.53, 2.92)	2.36±3.82 1.50 (1.58, 3.35)
Vertebra T8	89.61±12.03 <sup>*</sup> 91.22 (86.13, 91.72)	88.34±13.03 90.41 (84.42, 90.97)	1.97±3.10 1.50 (1.53, 2.80)	2.78±4.62 1.50 (1.76, 4.07)
Vertebra T7	89.40±12.45 <sup>*</sup> 91.59 (85.71, 91.63)	87.88±14.10 91.40 (83.57, 90.98)	1.96±3.01 <sup>*</sup> 1.50 (1.51, 2.80)	2.62±4.16 1.50 (1.68, 3.84)
Vertebra T6	89.16±12.39 <sup>*</sup> 90.62 (85.41, 91.33)	87.49±14.23 90.41 (83.21, 90.55)	1.93±3.01 <sup>*</sup> 1.50 (1.50, 2.77)	2.72±4.49 1.50 (1.68, 4.03)
Vertebra T5	90.13±3.02 90.10 (89.35, 90.90)	88.96±6.67 89.87 (87.05, 90.53)	1.56±0.18 1.50 (1.51, 1.61)	2.20±3.24 1.50 (1.54, 3.17)
Vertebra T4	89.71±3.30 89.83 (88.84, 90.54)	88.99±4.86 89.65 (87.65, 90.14)	1.56±0.21 1.50 (1.51, 1.62)	2.06±2.64 1.50 (1.55, 2.84)
Vertebra T3	89.67±3.23 89.58 (88.87, 90.45)	87.96±11.74 89.42 (84.57, 90.09)	1.56±0.20 1.50 (1.51, 1.61)	2.14±3.14 1.50 (1.55, 3.02)
Vertebra T2	89.82±3.11 90.26 (89.06, 90.58)	88.36±11.64 89.92 (85.08, 90.39)	1.56±0.24 1.50 (1.51, 1.63)	1.87±2.23 1.50 (1.54, 2.49)
Vertebra T1	89.92±3.18 90.55 (89.11, 90.69)	89.18±6.39 90.65 (87.35, 90.50)	1.62±0.37 1.50 (1.54, 1.72)	2.05±2.63 1.50 (1.55, 2.78)
Vertebra C7	87.70±5.21 90.09 (86.01, 89.18)	87.67±5.32 89.57 (85.93, 89.16)	1.95±1.15 1.50 (1.65, 2.34)	1.96±1.18 1.50 (1.65, 2.36)
Vertebra C6	85.76±5.31 85.82 (83.82, 87.58)	85.80±5.68 88.27 (83.73, 87.73)	1.83±0.60 1.50 (1.65, 2.06)	1.83±0.66 1.50 (1.64, 2.09)
Vertebra C5	86.59±4.58 86.90 (84.91, 88.19)	86.39±4.78 86.65 (84.68, 88.08)	1.72±0.42 1.50 (1.59, 1.89)	1.76±0.47 1.50 (1.60, 1.93)
Vertebra C4	86.72±4.10 <sup>*</sup> 86.63 (85.25, 88.17)	86.48±4.24 86.55 (84.97, 87.98)	1.68±0.31 1.50 (1.58, 1.80)	1.68±0.34 1.50 (1.56, 1.81)
Vertebra C3	87.68±3.61 <sup>*</sup> 87.77 (86.36, 88.93)	87.48±3.81 88.33 (86.08, 88.79)	1.62±0.28 1.50 (1.52, 1.73)	1.67±0.35 1.50 (1.56, 1.82)
Vertebra C2	89.91±2.97 90.73 (88.80, 90.98)	90.04±3.06 91.23 (88.91, 91.13)	1.54±0.16 1.50 (1.50, 1.61)	1.56±0.19 1.50 (1.50, 1.63)

*Continued on next page*



Organ	CADS (Dice)	TotalSeg (Dice)	CADS (HD95)	TotalSeg (HD95)
Vertebra C1	87.09±6.19 89.04 (84.43, 89.38)	86.92±7.75 89.20 (83.38, 89.60)	1.79±0.72 1.50 (1.55, 2.11)	1.90±1.11 1.50 (1.58, 2.43)
Humerus L	97.80±1.56 <sup>*</sup> 98.27 (97.21, 98.33)	92.89±7.59 95.62 (89.79, 95.03)	1.35±0.45 <sup>*</sup> 1.50 (1.15, 1.50)	5.61±12.13 1.50 (2.18, 10.84)
Humerus R	93.70±16.16 <sup>*</sup> 97.97 (87.27, 97.54)	90.41±16.95 95.34 (83.59, 94.43)	3.95±8.69 <sup>*</sup> 1.50 (1.57, 7.47)	24.28±114.71 1.50 (1.89, 67.43)
Scapula L	97.28±1.08 97.58 (96.82, 97.61)	97.66±1.33 <sup>*</sup> 98.02 (97.08, 98.06)	1.50±0.41 1.50 (1.33, 1.67)	0.94±0.72 <sup>*</sup> 1.50 (0.67, 1.22)
Scapula R	97.44±0.43 97.50 (97.26, 97.61)	97.95±0.37 <sup>*</sup> 98.01 (97.81, 98.10)	1.19±0.61 1.50 (0.94, 1.44)	0.62±0.74 <sup>*</sup> 0.00 (0.31, 0.94)
Clavicle L	98.07±0.56 98.20 (97.88, 98.25)	98.58±0.46 <sup>*</sup> 98.70 (98.43, 98.73)	0.80±0.74 1.50 (0.55, 1.06)	0.28±0.57 <sup>*</sup> 0.00 (0.10, 0.49)
Clavicle R	97.38±1.01 97.75 (97.00, 97.71)	98.11±0.86 <sup>*</sup> 98.39 (97.79, 98.38)	1.50±0.00 1.50 (1.50, 1.50)	0.70±0.75 <sup>*</sup> 0.00 (0.47, 0.94)
Femur L	94.52±3.70 94.98 (89.78, 98.81)	92.12±5.56 95.15 (84.32, 96.91)	3.08±1.33 3.00 (1.50, 4.74)	3.33±2.16 2.12 (1.50, 6.36)
Femur R	98.91±0.00 98.91 (98.91, 98.91)	96.52±0.00 96.52 (96.52, 96.52)	1.50±0.00 1.50 (1.50, 1.50)	1.50±0.00 1.50 (1.50, 1.50)
Hip L	98.32±0.16 98.25 (98.16, 98.53)	98.60±0.06 98.58 (98.54, 98.69)	1.50±0.00 1.50 (1.50, 1.50)	1.00±0.71 1.50 (0.00, 1.50)
Hip R	98.17±0.47 97.93 (97.76, 98.83)	98.46±0.14 98.53 (98.26, 98.59)	1.50±0.00 1.50 (1.50, 1.50)	1.00±0.71 1.50 (0.00, 1.50)
Sacrum	97.59±0.52 <sup>*</sup> 97.64 (97.42, 97.74)	86.32±1.87 86.51 (85.84, 86.96)	1.50±0.00 <sup>*</sup> 1.50 (1.50, 1.50)	6.38±1.07 6.36 (6.05, 6.68)
Rib-1 L	93.85±0.75 93.64 (93.19, 94.50)	90.52±4.29 90.66 (86.45, 94.31)	1.50±0.00 1.50 (1.50, 1.50)	3.82±3.04 3.00 (1.42, 6.82)
Rib-2 L	92.96±4.49 93.91 (90.33, 95.09)	91.66±3.29 91.40 (89.87, 93.46)	1.34±0.62 <sup>*</sup> 1.50 (0.99, 1.64)	4.67±4.99 1.50 (2.35, 7.71)
Rib-3 L	92.80±5.27 <sup>*</sup> 94.83 (89.90, 95.17)	87.77±14.46 90.32 (79.29, 93.04)	1.74±2.15 <sup>*</sup> 1.50 (0.80, 2.94)	6.10±7.94 2.12 (2.62, 10.45)
Rib-4 L	95.85±1.57 <sup>*</sup> 96.50 (95.06, 96.55)	89.78±10.28 92.14 (84.05, 93.65)	0.97±0.72 <sup>*</sup> 1.50 (0.62, 1.32)	7.69±9.35 3.32 (3.55, 12.36)
Rib-5 L	94.99±3.64 <sup>*</sup> 95.89 (92.94, 96.38)	91.40±6.30 92.30 (88.07, 94.21)	1.45±1.55 <sup>*</sup> 1.50 (0.77, 2.27)	6.06±6.81 4.50 (3.15, 9.77)

Continued on next page

Organ	CADS (Dice)	TotalSeg (Dice)	CADS (HD95)	TotalSeg (HD95)
Rib-6 L	95.10±3.12 <sup>*</sup>	93.78±3.13	1.36±0.44 <sup>*</sup>	3.49±3.59
	96.12	93.24	1.50	1.50
	(93.60, 96.22)	(92.44, 95.10)	(1.14, 1.50)	(2.03, 5.10)
Rib-7 L	96.84±1.18	96.32±3.89	0.75±0.75	3.02±6.85
	96.92	98.04	0.75	0.00
	(96.29, 97.37)	(94.33, 97.88)	(0.42, 1.08)	(0.42, 6.70)
Rib-8 L	96.13±3.25	96.26±4.58	0.57±1.08	9.75±34.77
	97.25	98.33	0.00	0.00
	(94.50, 97.43)	(93.91, 98.06)	(0.17, 1.12)	(0.42, 27.20)
Rib-9 L	96.87±1.49	96.18±2.83	0.68±0.75 <sup>*</sup>	1.71±2.42
	97.16	97.30	0.00	0.00
	(96.19, 97.49)	(94.88, 97.37)	(0.38, 0.97)	(0.75, 2.85)
Rib-10 L	91.72±12.24 <sup>*</sup>	88.26±11.82	16.53±57.68 <sup>*</sup>	21.00±56.69
	95.50	90.81	1.50	6.54
	(84.82, 95.83)	(81.40, 92.82)	(0.84, 47.51)	(4.06, 52.42)
Rib-11 L	95.23±1.27 <sup>*</sup>	91.78±3.24	1.22±0.59 <sup>*</sup>	4.40±3.23
	95.34	91.17	1.50	4.03
	(94.60, 95.84)	(90.26, 93.40)	(0.94, 1.50)	(2.84, 6.03)
Rib-12 L	92.73±2.68 <sup>*</sup>	81.58±6.47	1.51±0.34 <sup>*</sup>	8.58±3.21
	92.49	80.96	1.50	9.12
	(91.70, 93.68)	(79.29, 83.98)	(1.37, 1.63)	(7.37, 9.71)
Rib-1 R	94.87±1.99	93.08±3.36	1.25±0.56	2.13±1.92
	94.82	93.37	1.50	1.50
	(93.30, 96.51)	(90.41, 95.75)	(0.75, 1.50)	(0.85, 3.95)
Rib-2 R	95.48±1.27 <sup>*</sup>	93.15±2.42	1.18±0.62	1.83±1.46
	95.90	93.63	1.50	1.50
	(94.78, 96.10)	(91.85, 94.38)	(0.86, 1.50)	(1.16, 2.69)
Rib-3 R	89.61±21.48 <sup>*</sup>	87.45±20.03	35.61±145.25	5.74±8.29
	95.28	93.39	1.50	1.50
	(78.71, 95.76)	(77.06, 93.86)	(0.95, 104.42)	(2.43, 9.89)
Rib-4 R	93.65±8.47 <sup>*</sup>	92.25±8.52	2.22±4.35	3.78±9.13
	96.27	95.17	1.50	1.50
	(88.92, 96.49)	(87.18, 95.45)	(0.80, 4.66)	(1.02, 8.82)
Rib-5 R	93.36±4.81	92.61±6.87	1.99±2.87	3.25±6.56
	95.85	94.27	1.50	1.50
	(90.54, 95.85)	(88.11, 95.57)	(0.85, 3.84)	(1.00, 7.36)
Rib-6 R	94.30±4.24	94.34±3.57	1.68±2.71	1.46±2.16
	95.92	95.69	1.50	1.50
	(92.01, 96.11)	(92.53, 96.02)	(0.75, 3.15)	(0.66, 2.68)
Rib-7 R	96.59±1.96	96.27±3.20	0.65±0.79	1.45±3.34
	97.37	97.44	0.00	0.00
	(95.57, 97.42)	(94.57, 97.65)	(0.26, 1.04)	(0.29, 3.29)
Rib-8 R	97.16±1.28	97.08±2.60	0.36±0.63	0.44±0.68
	97.65	98.06	0.00	0.00
	(96.51, 97.71)	(95.70, 98.13)	(0.10, 0.71)	(0.18, 0.79)
Rib-9 R	96.62±2.42	95.79±5.77	0.48±0.75	1.38±3.92
	97.42	98.26	0.00	0.00
	(95.37, 97.61)	(92.72, 97.99)	(0.18, 0.87)	(0.18, 3.44)
Rib-10 R	94.18±4.52	91.65±4.18	1.57±1.65 <sup>*</sup>	4.22±4.12
	95.96	92.11	1.50	3.35
	(91.37, 95.98)	(89.25, 93.72)	(0.81, 2.62)	(2.32, 6.71)

*Continued on next page*

Organ	CADS (Dice)	TotalSeg (Dice)	CADS (HD95)	TotalSeg (HD95)
Rib-11 R	95.32±1.35 <sup>*</sup> 95.30 (94.71, 95.95)	87.34±11.96 90.07 (81.28, 92.01)	1.17±0.62 <sup>*</sup> 1.50 (0.83, 1.42)	8.62±12.33 4.95 (3.74, 15.00)
Rib-12 R	91.32±8.64 <sup>*</sup> 93.46 (87.68, 93.74)	79.67±8.33 80.36 (76.48, 82.62)	1.86±2.06 <sup>*</sup> 1.50 (1.36, 2.70)	11.51±4.93 11.42 (9.78, 13.43)
Sternum	88.08±4.84 <sup>*</sup> 90.10 (86.48, 89.49)	86.12±5.34 87.85 (84.39, 87.73)	3.79±6.74 2.12 (2.37, 6.21)	3.74±4.21 <sup>*</sup> 2.60 (2.76, 5.34)
Compact bone	67.63±7.47 71.28 (62.91, 71.78)	— — —	2.85±1.37 2.12 (2.14, 3.73)	— — —
Spongy bone	59.51±10.45 65.70 (52.89, 65.08)	— — —	4.12±1.92 3.35 (3.14, 5.41)	— — —
Mandible	92.90±2.13 93.42 (91.63, 94.03)	— — —	1.55±0.17 1.50 (1.50, 1.66)	— — —
Bones	91.13±13.20 94.28 (88.90, 93.06)	— — —	2.22±3.30 1.50 (1.77, 2.79)	— — —
<b>Endocrine System</b>				
Adrenal gland R	69.78±22.14 73.50 (65.74, 73.70)	70.67±23.79 <sup>*</sup> 74.81 (66.28, 74.80)	4.84±7.42 2.80 (3.76, 6.37)	4.88±7.51 2.12 (3.77, 6.42)
Adrenal gland L	71.94±22.20 77.32 (67.71, 75.76)	73.51±24.10 <sup>*</sup> 79.60 (69.04, 77.80)	18.01±148.03 2.12 (3.49, 46.24)	18.05±148.04 2.12 (3.49, 46.27)
Thyroid	73.31±17.51 <sup>*</sup> 77.70 (67.47, 78.03)	68.35±19.09 75.47 (62.39, 73.78)	5.11±4.97 <sup>*</sup> 3.67 (3.81, 6.75)	6.61±7.04 4.74 (4.78, 8.99)
Pituitary gland	67.74±12.30 67.81 (60.30, 74.29)	— — —	2.33±0.76 2.12 (1.97, 2.80)	— — —
Gland structure	52.92±15.69 57.12 (48.06, 57.52)	— — —	44.82±13.94 42.69 (40.91, 49.23)	— — —
<b>Muscular System</b>				
Gluteus maximus muscle L	96.66±1.73 97.33 (95.77, 97.41)	97.87±1.00 <sup>*</sup> 98.24 (97.36, 98.31)	1.81±0.66 1.50 (1.54, 2.16)	1.54±0.15 1.50 (1.50, 1.61)
Gluteus maximus muscle R	95.52±5.56 97.47 (92.59, 97.45)	97.69±1.88 <sup>*</sup> 98.52 (96.75, 98.47)	2.66±4.02 1.50 (1.50, 4.72)	1.97±1.27 1.50 (1.50, 2.66)
Gluteus medius muscle L	95.86±1.75 96.73 (94.61, 96.89)	97.17±1.27 <sup>*</sup> 97.97 (96.29, 97.93)	1.97±0.60 1.50 (1.64, 2.37)	1.74±0.49 1.50 (1.50, 2.07)
Gluteus medius muscle R	97.01±0.68 97.29 (96.58, 97.38)	97.96±0.60 <sup>*</sup> 98.29 (97.58, 98.27)	1.66±0.35 1.50 (1.50, 1.87)	1.56±0.18 1.50 (1.50, 1.67)

Continued on next page

Organ	CADS (Dice)	TotalSeg (Dice)	CADS (HD95)	TotalSeg (HD95)
Gluteus minius muscle L	94.58±1.56 94.95 (94.01, 95.07)	96.20±1.47* 96.77 (95.67, 96.66)	1.58±0.20 1.50 (1.52, 1.65)	1.51±0.07 1.50 (1.50, 1.54)
Gluteus minius muscle R	94.79±1.58 95.16 (94.01, 95.44)	96.62±1.18* 97.01 (96.02, 97.09)	1.59±0.27 1.50 (1.50, 1.73)	1.53±0.14 1.50 (1.50, 1.60)
Deep muscle of back L	97.35±1.42 97.90 (96.97, 97.67)	97.91±1.00* 98.32 (97.65, 98.14)	1.55±0.26 1.50 (1.50, 1.62)	1.51±0.08 1.50 (1.50, 1.53)
Deep muscle of back R	96.74±4.47 97.74 (95.48, 97.61)	97.60±2.53* 98.19 (96.89, 98.07)	7.37±45.79 1.50 (1.51, 18.95)	7.33±46.22 1.50 (1.51, 18.93)
Iliopsoas muscle L	96.69±1.26 96.95 (96.21, 97.08)	97.59±0.99* 97.82 (97.23, 97.91)	1.52±0.11 1.50 (1.50, 1.56)	1.50±0.00 1.50 (1.50, 1.50)
Iliopsoas muscle R	96.77±2.07 97.35 (95.93, 97.30)	97.61±1.67* 98.10 (96.96, 98.11)	1.54±0.22 1.50 (1.50, 1.62)	1.50±0.00 1.50 (1.50, 1.50)
Psoas major muscle R	86.84±14.23 89.22 (81.93, 89.89)	— — —	7.19±9.93 4.24 (4.81, 10.76)	— — —
Psoas major muscle L	88.99±4.22 89.73 (87.67, 90.28)	— — —	5.13±5.05 4.24 (3.82, 6.92)	— — —
Rectus abdominis muscle R	73.01±14.25 76.47 (68.33, 77.00)	— — —	17.10±19.84 8.37 (11.48, 23.57)	— — —
Rectus abdominis muscle L	72.00±15.42 76.79 (67.24, 76.54)	— — —	19.78±33.26 7.78 (11.58, 31.75)	— — —
Muscle of head	46.66±19.87 50.99 (33.89, 57.51)	— — —	3.87±3.19 2.60 (2.31, 6.02)	— — —
Muscle	92.22±13.44 95.53 (89.93, 94.17)	— — —	2.25±2.98 1.50 (1.83, 2.77)	— — —
Sensory Organs				
Eyeball	77.77±19.72 83.84 (64.64, 87.07)	— — —	4.39±4.26 2.60 (2.22, 7.22)	— — —
Cochlear L	66.96±22.53 69.70 (52.48, 77.22)	— — —	2.38±1.96 1.62 (1.64, 3.63)	— — —
Cochlear R	56.15±23.81 63.49 (41.53, 68.49)	— — —	2.91±2.30 2.12 (1.85, 4.42)	— — —
Anterior eyeball segment L	75.10±6.14 74.08 (71.58, 78.49)	— — —	2.01±0.53 2.12 (1.73, 2.31)	— — —
Anterior eyeball segment R	72.83±7.20 74.03 (68.72, 76.86)	— — —	2.50±1.03 2.25 (1.93, 3.08)	— — —

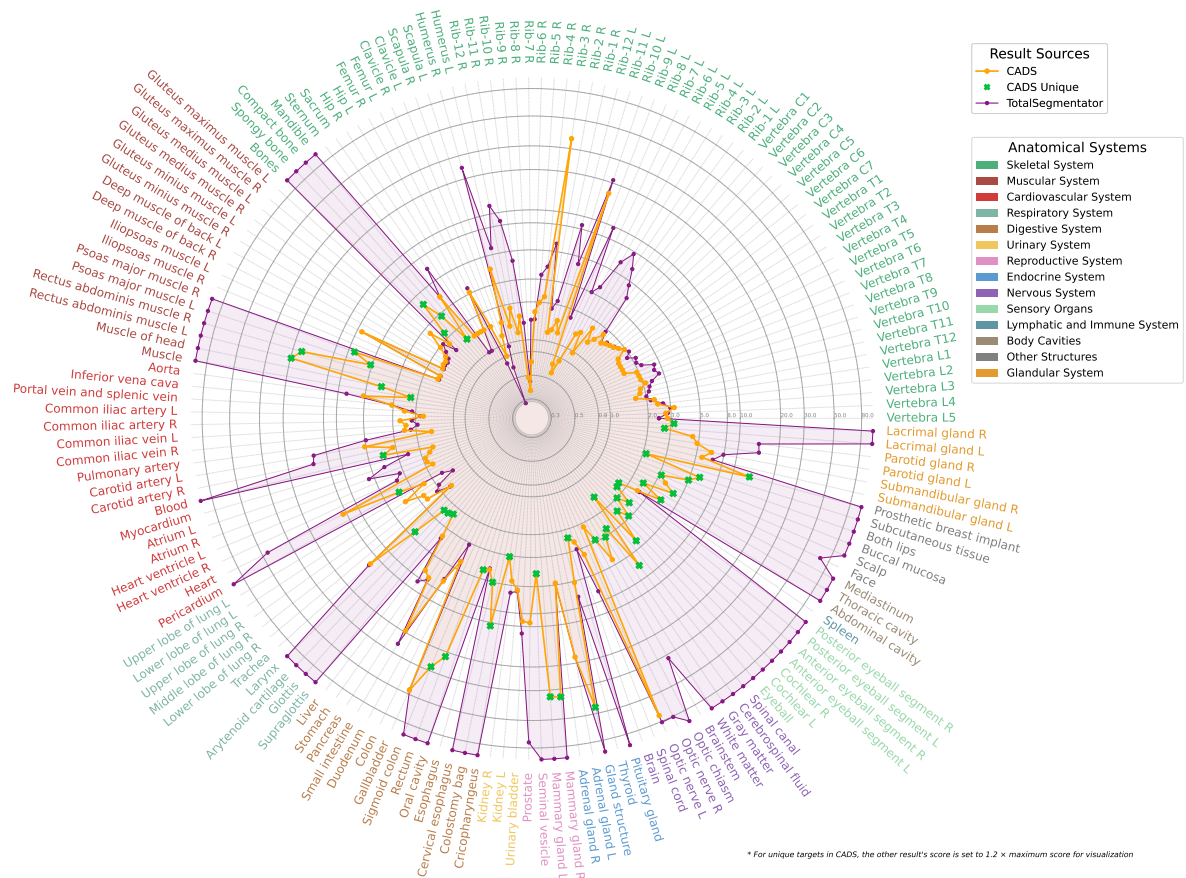
Continued on next page

Organ	CADS (Dice)	TotalSeg (Dice)	CADS (HD95)	TotalSeg (HD95)
Posterior eyeball segment L	89.99±2.57 90.84 (88.37, 91.22)	— — —	1.76±0.53 1.50 (1.50, 2.12)	— — —
Posterior eyeball segment R	89.50±2.91 90.10 (87.69, 90.92)	— — —	1.73±0.45 1.50 (1.50, 2.01)	— — —
<b>Body Cavities</b>				
Abdominal cavity	95.20±13.92 98.36 (92.67, 97.07)	— — —	3.80±8.97 1.50 (2.48, 5.39)	— — —
Thoracic cavity	95.07±13.50 98.14 (92.66, 97.14)	— — —	2.50±4.40 1.50 (1.85, 3.25)	— — —
Mediastinum	85.32±13.02 88.68 (83.10, 87.23)	— — —	4.33±2.59 3.67 (3.93, 4.77)	— — —
<b>Glandular System</b>				
Lacrimal gland L	62.85±12.14 63.52 (56.06, 69.44)	— — —	2.69±1.13 2.24 (2.07, 3.35)	— — —
Lacrimal gland R	58.05±12.59 59.97 (50.43, 64.84)	— — —	3.16±1.32 2.63 (2.49, 3.98)	— — —
Submandibular gland L	76.66±9.37* 76.60 (71.84, 81.02)	72.79±11.72 75.86 (66.74, 78.24)	5.56±3.40 4.54 (3.97, 7.31)	6.73±4.51 5.25 (4.64, 9.02)
Submandibular gland R	74.33±12.19 79.25 (67.97, 79.72)	70.88±16.74 76.25 (61.87, 78.24)	6.44±4.82 4.09 (4.24, 8.94)	7.94±6.27 4.62 (5.05, 11.17)
Parotid gland L	80.64±7.16* 83.44 (76.77, 83.76)	52.68±11.02 51.63 (47.22, 58.07)	4.89±1.80* 4.74 (4.04, 5.80)	14.40±4.31 14.50 (12.40, 16.58)
Parotid gland R	81.63±7.33* 84.52 (77.77, 84.86)	54.10±8.05 54.64 (50.04, 57.92)	4.47±2.19* 3.35 (3.48, 5.61)	14.13±4.11 13.98 (12.22, 16.32)
<b>Other Structures</b>				
Face	96.35±1.72* 96.48 (95.21, 97.32)	29.64±19.10 31.19 (18.31, 41.68)	3.52±1.89* 3.35 (2.46, 4.78)	68.28±91.42 34.99 (31.66, 132.16)
Scalp	92.58±2.17 93.41 (91.20, 93.73)	— — —	3.12±1.32 2.60 (2.45, 4.00)	— — —
Buccal mucosa	67.05±7.46 70.04 (62.51, 70.80)	— — —	5.00±2.40 4.50 (3.86, 6.53)	— — —
Both lips	67.15±13.75 69.17 (58.72, 74.13)	— — —	5.90±3.34 4.62 (4.20, 7.93)	— — —
Subcutaneous tissue	93.34±13.60 96.55 (90.99, 95.30)	— — —	2.12±2.54 1.50 (1.75, 2.56)	— — —

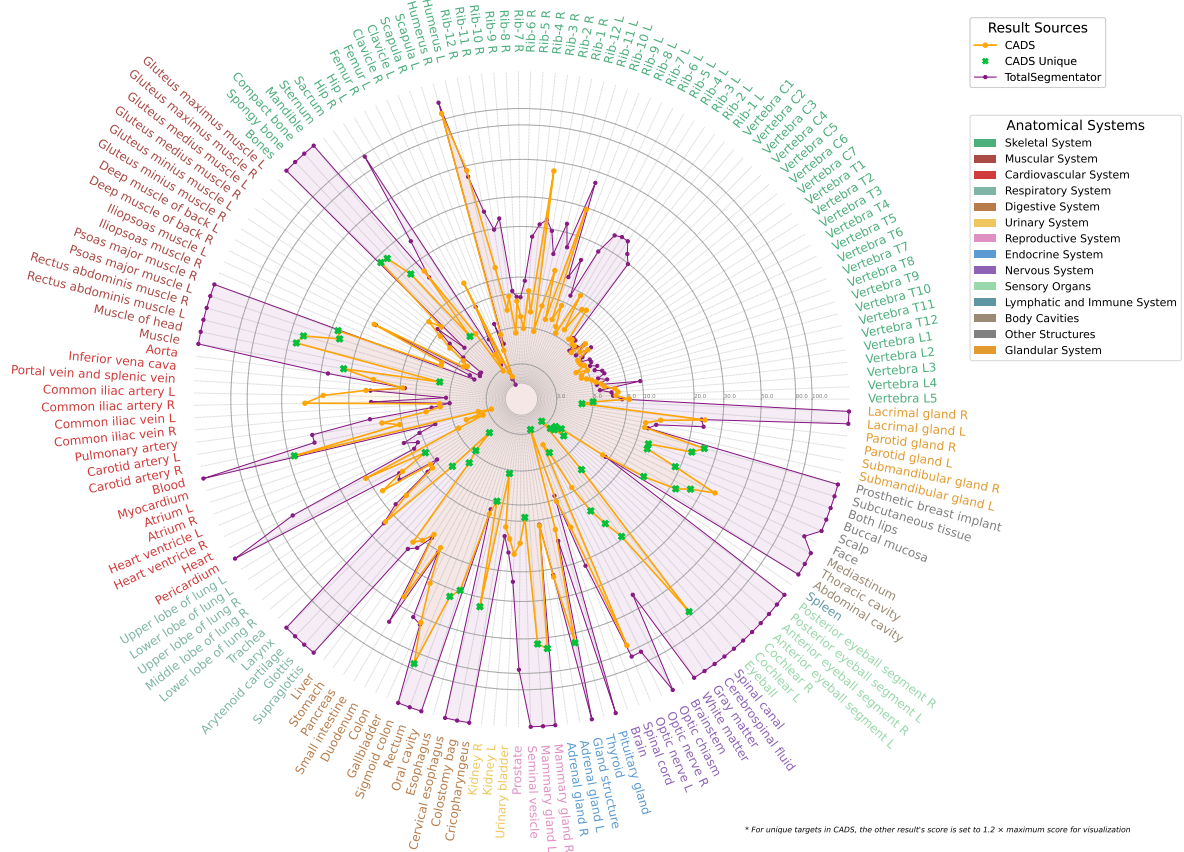
Continued on next page



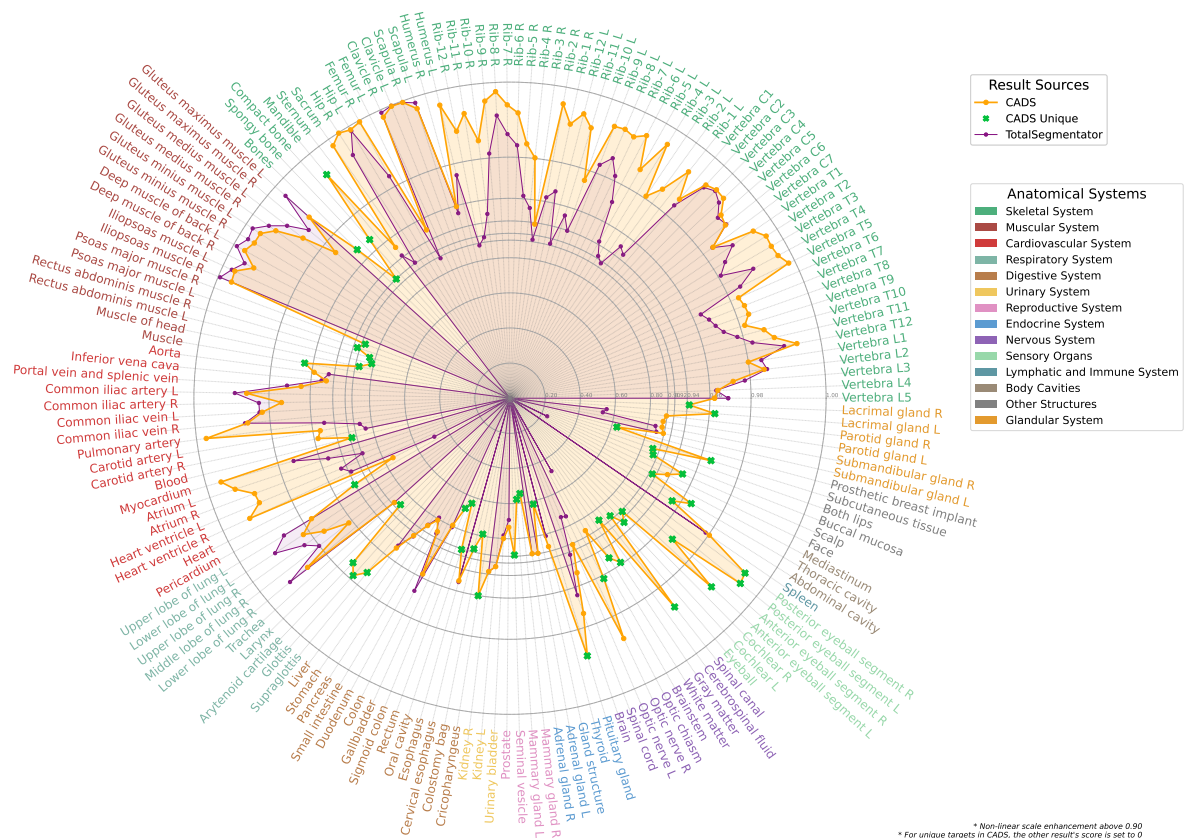
Organ	CADS (Dice)	TotalSeg (Dice)	CADS (HD95)	TotalSeg (HD95)
Prosthetic breast implant	69.77±17.06	—	13.38±7.82	—
	79.72	—	11.72	—
	(45.76, 83.84)	—	(4.74, 23.67)	—



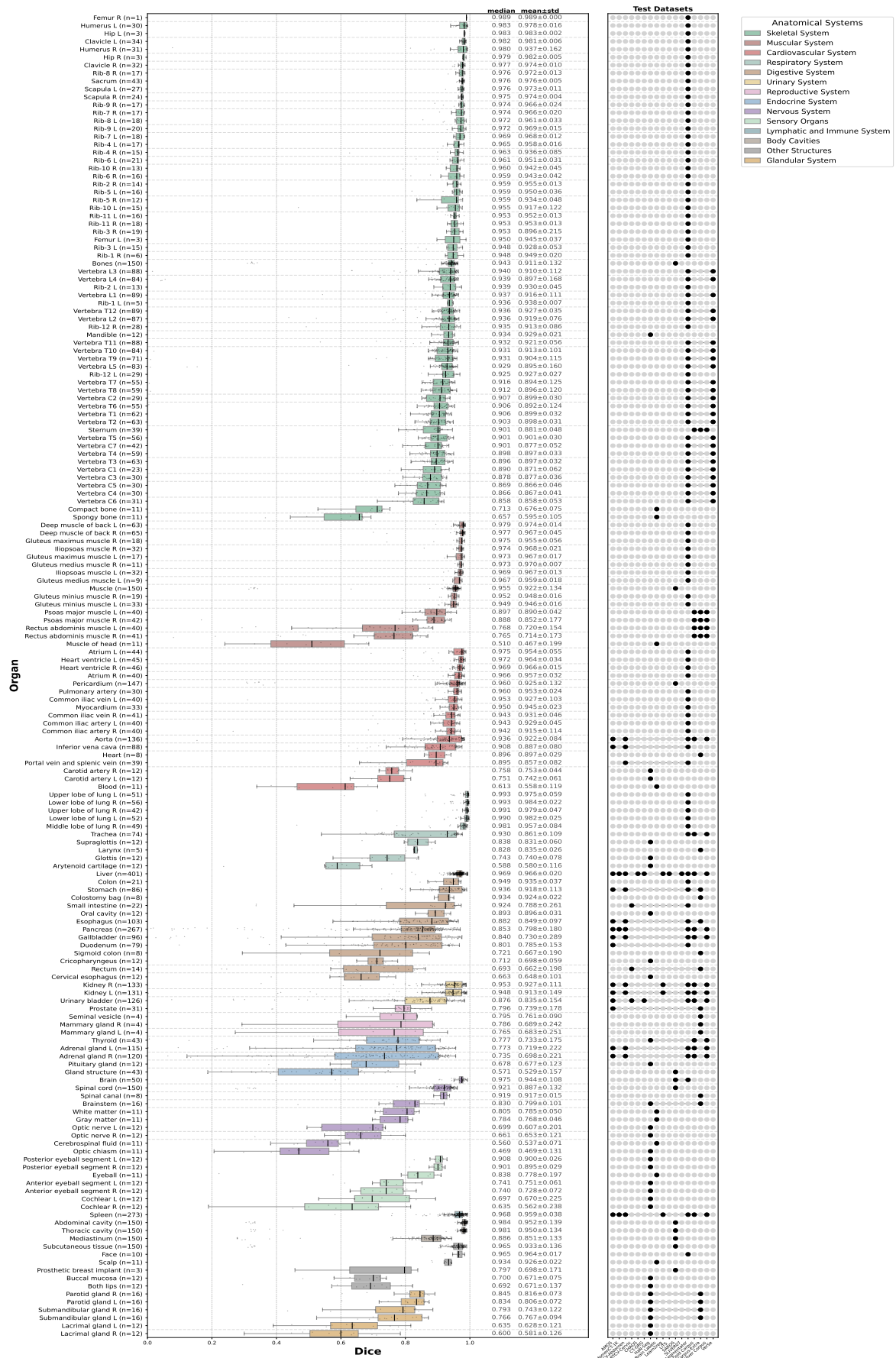
Supplementary Fig. A.9: **Structure-level performance analysis of HD95 scores.** Visualization of segmentation performance across 167 anatomical structures, grouped by anatomical systems. The radar plot presents HD95 scores (in mm), where lower values indicate superior performance.



Supplementary Fig. A.10: **Structure-level performance analysis of HD scores.** Visualization of segmentation performance across 167 anatomical structures, grouped by anatomical systems. The radar plot presents HD scores (in mm), where lower values indicate superior performance.

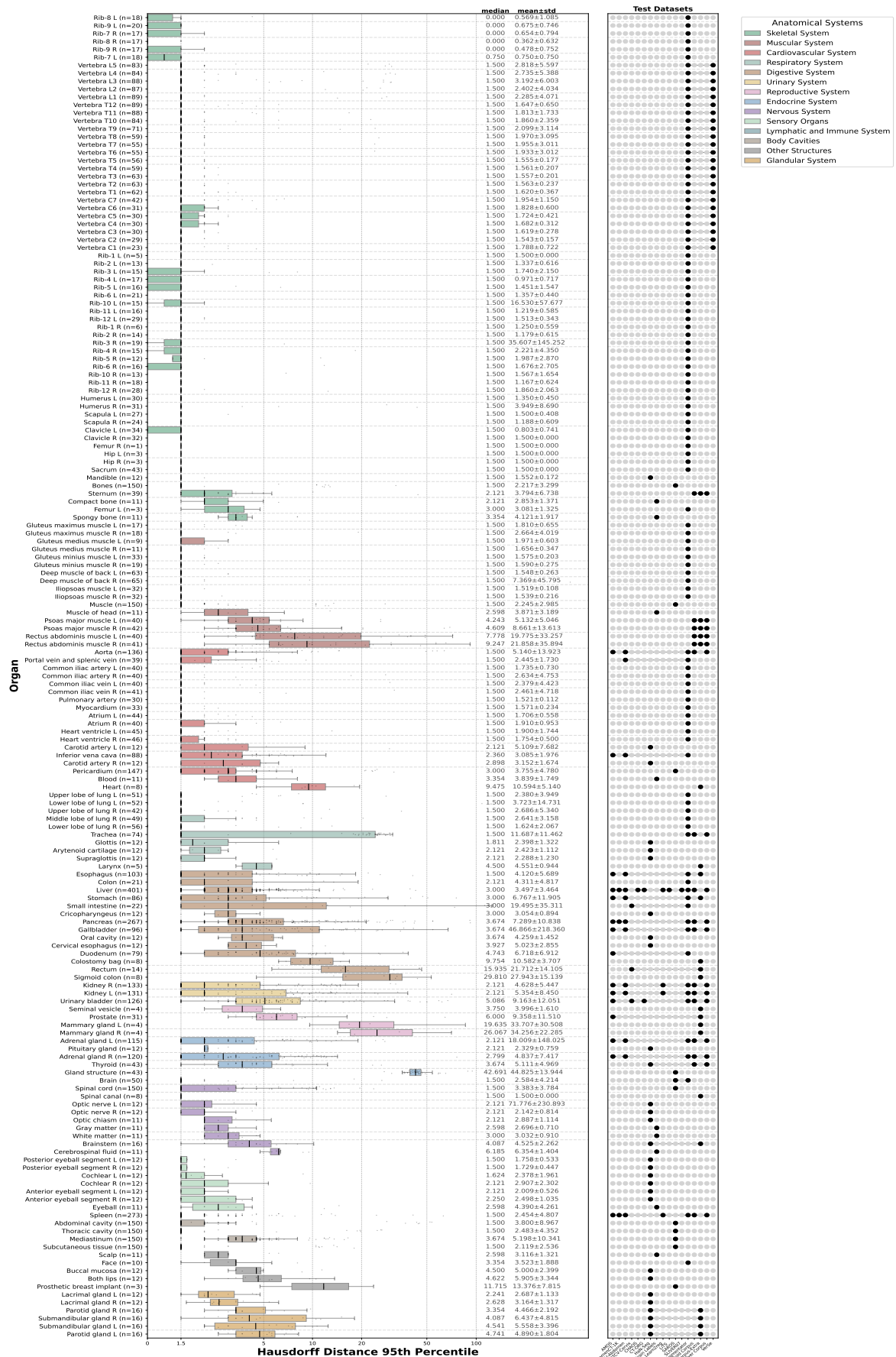


Supplementary Fig. A.11: **Structure-level performance analysis of NSD scores.** Visualization of segmentation performance across 167 anatomical structures, grouped by anatomical systems. The radar plot presents normalized surface dice scores (increasing radially from 0 at center to 1 at periphery).



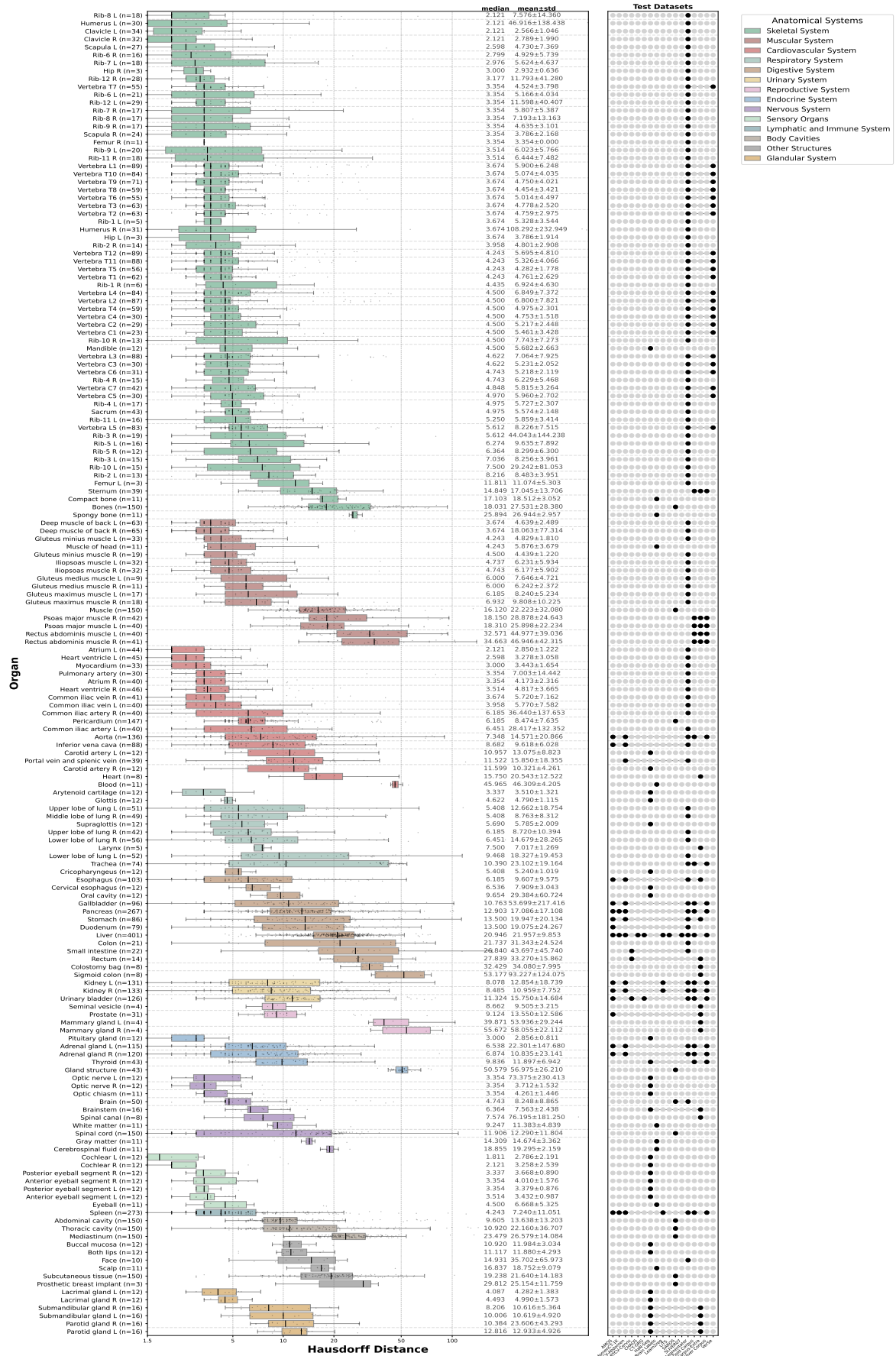
Supplementary Fig. A.12: CADS-model Dice score distribution.



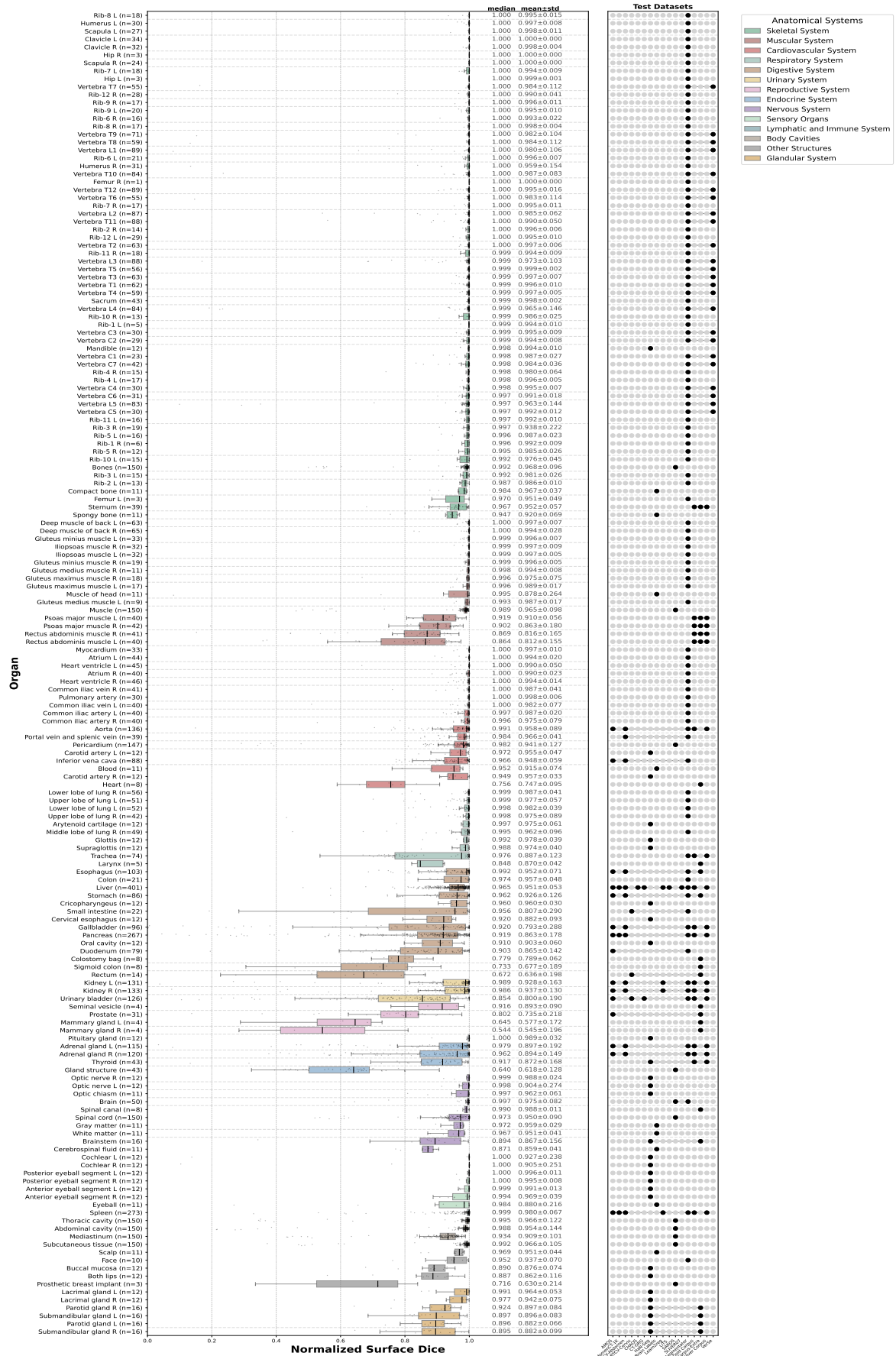


Supplementary Fig. A.13: CADS-model 95% Hausdorff distance score distribution.





Supplementary Fig. A.14: CADS-model Hausdorff distance score distribution.



Supplementary Fig. A.15: CADS-model normalized surface Dice score distribution.

**Algorithm 1** Flavor priority ranking

---

```

1: function GETMEANScore(organ, scores_data)    ▷ Calculates mean score, considering in/out-distribution
   data
2:   if organ has out-distribution results in scores_data then return Mean(scores_data's out-dist results)
3:   elsereturn Mean(scores_data's in-dist results)
4:   end if
5: end function

6: function TESTSIGNIFICANCE(organ, scores_data)  ▷ Performs statistical tests; returns significant pairwise
   differences ( $p < 0.05$ ) or  $\emptyset$ 
7:   Load 3 flavors' scores; Check normality (Shapiro-Wilk), variance equality (Levene)
8:   if scores are normal and variances are equal then
9:     stat_test  $\leftarrow$  ANOVA
10:  else if variances are not equal then
11:    stat_test  $\leftarrow$  Welch's ANOVA
12:  else
13:    stat_test  $\leftarrow$  Kruskal-Wallis
14:  end if
15:  Perform stat_test and post-hoc comparison (e.g., Tukey's HSD or Dunn's test)
16:  if post-hoc  $p < 0.05$  then return Significant pairs &  $p$ -values
17:  elsereturn  $\emptyset$ 
18:  end if
19: end function

20: for group in 9 body parts do
21:   for organ in organs do
22:     mean_Dice  $\leftarrow$  GETMEANScore(organ, DiceScores)
23:     sig_Diff_Dice  $\leftarrow$  TESTSIGNIFICANCE(organ, DiceScores)
24:     flavor_ranking_points  $\leftarrow$  {GT  $\mapsto$  0, P  $\mapsto$  0, S  $\mapsto$  0}    ▷ P: Pseudo, S: Shape
25:     if sig_Diff_Dice  $\neq \emptyset$  then
26:       Update flavor_ranking_points based on significant Dice differences
27:     else
28:       Update flavor_ranking_points based on mean Dice ranks
29:     end if
30:     ▷ Secondary HD95 evaluation if primary Dice ranking is ambiguous
31:     current_flavor_order  $\leftarrow$  Sort flavors by points in flavor_ranking_points (descending)
32:     if Top ranks in current_flavor_order are ambiguous then
33:       relevant_flavors  $\leftarrow$  Identify top-ranked, ambiguously ordered flavors
34:       mean_HD95  $\leftarrow$  GETMEANScore(organ, HD95Scores[relevant_flavors])
35:       sig_Diff_HD95  $\leftarrow$  TESTSIGNIFICANCE(organ, HD95Scores[relevant_flavors])
36:       hd95_points_update  $\leftarrow$  {flavor  $\mapsto$  0 for flavor in relevant_flavors}
37:       if sig_Diff_HD95  $\neq \emptyset$  then
38:         Update hd95_points_update based on significant HD95 differences
39:       else
40:         Update hd95_points_update based on mean HD95 ranks
41:       end if
42:       Add hd95_points_update to flavor_ranking_points for relevant_flavors    ▷ Refine points
43:     end if
44:     final_priority_order  $\leftarrow$  Sort flavors by final flavor_ranking_points (descending)
45:     Store final_priority_order for organ
46:   end for
47: end for

```

---

Data Source	#Vols	# Ann. Vols	#Train (with ann.)	#Train (without ann.)	#Test
VISCERAL Gold Corpus	40	40	32	-	8
VISCERAL Gold Corpus-Extra	-	40	32	-	8
VISCERAL Silver Corpus	127	127	101	-	26
KiTS	300	300	240	-	60
LiTS	201	201	131	-	70
BTCV-Abdomen	50	30	24	20	6
BTCV-Cervix	50	30	24	20	6
CHAOS	40	20	10	20	10
AbdomenCT-1K	1,062	1,000	849	62	151
VerSe	374	374	300	-	74
EXACT09	40	-	-	40	-
CAD-PE	40	-	-	40	-
RibFrac	660	-	-	660	-
Learn2reg	16	8	-	8	8
LNDb	294	-	-	294	-
LOLA11	55	-	-	55	-
SLIVER07	30	20	-	10	20
STOIC2021	2,000	-	-	2,000	-
CT-RATE	3,134	-	-	3,134	-
EMPIRE10	60	60	48	-	12
AMOS	200	200	161	-	39
HaN-Seg	42	42	30	-	12
HaN-Seg Extra Brain Labels	-	42	30	-	12
CT-ORG	140	140	112	-	28
LIDC-IDRI	997	-	-	997	-
CT Lymph Nodes	174	-	-	174	-
CPTAC-CCRCC	258	-	-	258	-
CPTAC-LUAD	133	-	-	133	-
CT Images in COVID-19	121	-	-	121	-
NSCLC Radiogenomics	131	-	-	131	-
Pancreas-CT	80	-	-	80	-
Pancreatic-CT-CBCT- SEG	93	-	-	93	-
RIDER Lung CT	59	-	-	59	-
TCGA-KICH	17	-	-	17	-
TCGA-KIRC	398	-	-	398	-
TCGA-KIRP	19	-	-	19	-
TCGA-LIHC	242	-	-	242	-
National Lung Screening Trial (NLST)	7,172	-	-	7,172	-
Total-Segmentator	1,203	1,203	1,138	-	65
SAROS	900	900	750	-	150
New Hospital Data - CT-TRI	586	-	-	586	-
New Hospital Data - Head	484	-	-	484	-
<b>Total</b>	<b>22,022</b>	<b>4,695</b>	<b>3,950</b>	<b>17,327</b>	<b>745</b>

Supplementary Table A.3: **Data partitioning for training and evaluating CADS-model across all data sources.** The training dataset consists of two subsets: volumes with original manual annotations and those without annotations (utilized for pseudo-label training). This strategic partitioning maintains independent evaluation sets and prevents data leakage throughout model development.

		1	2	3	4	5	6	7	8	9
<b>Initial specialized</b>		1,138	1,138	1,138	1,138	1,138	32	30	30	721
<b>3 Flavors</b>	<i>GT</i>	1,138	1,138	1,138	1,138	1,138	32	30	30	721
	<i>Pseudo</i>	20,455	20,990	21,032	20,483	20,372	20,980	1,082	312	21,119
	<i>Shape</i>	18,415	18,896	18,934	18,440	18,340	18,882	974	281	19,021
<b>CADS-model</b>		21,277	21,277	21,277	21,277	21,277	21,277	1,145	363	21,277

Supplementary Table A.4: **Training data composition across model development stages.** This table details the number of training images used at different development phases for each of the nine anatomical model groups (1-9). The development stages include: initial specialized models, intermediate three model flavors (GT, pseudo-labels, and shape-based) for generating CADS-dataset labels, and the final CADS-model leveraging the complete, refined CADS-dataset.

Supplementary Table A.6: **Disease distribution in the University Hospital Zurich evaluation cohort.** Percentage distribution of primary disease sites among 2,864 oncology patients used for real-world clinical validation.

Primary Disease Site Percentage (%)	
Brain/CNS	21.77
Bone	16.65
Head & Neck	13.06
Breast	11.83
Thorax	10.81
Genitourinary	8.85
Other	5.48
Abdomen/GI	4.32
Soft Tissue	2.32
Skin	2.25
Hematologic	1.89
Endocrine	0.54
Vascular	0.22

Supplementary : Dice score (%)  $\uparrow$  comparison across 18 datasets.

Model	VISCERAL GC	VISCERAL GC-Extra	VISCERAL SC	KITS	LiTS	BTCV- Abdomen	BTCV- Cervix	CHAOS	CT-ORG
TotalSeg	83.39	66.94	70.94	88.36	95.89	85.15	47.18	96.84	93.27
CADS	83.66	75.95	72.10	91.31	96.08	83.84	65.81	96.90	93.03
$\Delta$	<b>+0.28</b>	<b>+9.01</b>	<b>+1.15</b>	<b>+2.95</b>	<b>+0.19</b>	-1.32	<b>+18.64</b>	<b>+0.06</b>	-0.24
Model	AbdomenCT- 1K	VerSe	Learn2reg	SLIVER07	EMPIRE10	Total- Segmentator	AMOS	HaN-Seg	SAROS
TotalSeg	92.15	91.57	91.25	96.65	97.67	91.49	82.39	60.80	87.97
CADS	92.93	91.79	91.40	96.87	91.18	93.15	82.57	72.98	91.64
$\Delta$	<b>+0.78</b>	<b>+0.21</b>	<b>+0.14</b>	<b>+0.22</b>	-6.49	<b>+1.66</b>	<b>+0.18</b>	<b>+12.19</b>	<b>+3.67</b>

Supplementary : HD95 (mm)  $\downarrow$  comparison across 18 datasets..

Model	VISCERAL GC	VISCERAL GC-Extra	VISCERAL SC	KITS	LiTS	BTCV- Abdomen	BTCV- Cervix	CHAOS	CT-ORG
TotalSeg	8.12	18.43	30.12	7.65	4.46	5.55	83.20	3.33	9.05
CADS	7.98	8.68	29.65	7.36	4.05	4.06	40.99	3.21	9.29
$\Delta$	<b>-0.14</b>	<b>-9.75</b>	<b>-0.47</b>	<b>-0.29</b>	<b>-0.41</b>	<b>-1.49</b>	<b>-42.21</b>	<b>-0.12</b>	+0.24
Model	AbdomenCT- 1K	VerSe	Learn2reg	SLIVER07	EMPIRE10	Total- Segmentator	AMOS	HaN-Seg	SAROS
TotalSeg	4.07	2.05	4.99	3.70	2.23	3.86	10.85	32.89	4.97
CADS	3.54	1.92	4.87	3.53	8.89	2.40	6.15	18.71	3.00
$\Delta$	<b>-0.53</b>	<b>-0.14</b>	<b>-0.12</b>	<b>-0.17</b>	+6.66	<b>-1.46</b>	<b>-4.69</b>	<b>-14.18</b>	<b>-1.96</b>

Supplementary : Normalized surface Dice (%)  $\uparrow$  comparison across 18 datasets.

Model	VISCERAL GC	VISCERAL GC-Extra	VISCERAL SC	KITS	LiTS	BTCV- Abdomen	BTCV- Cervix	CHAOS	CT-ORG
TotalSeg	88.14	67.50	74.40	89.05	92.62	93.90	42.35	95.21	91.65
CADS	88.26	80.62	75.52	92.56	93.04	92.68	63.04	95.19	91.40
$\Delta$	<b>+0.11</b>	<b>+13.12</b>	<b>+1.12</b>	<b>+3.51</b>	<b>+0.42</b>	-1.22	<b>+20.69</b>	-0.02	-0.25
Model	AbdomenCT- 1K	VerSe	Learn2reg	SLIVER07	EMPIRE10	Total- Segmentator	AMOS	HaN-Seg	SAROS
TotalSeg	94.45	98.54	91.62	95.06	97.39	96.59	89.64	73.09	94.22
CADS	95.45	98.87	91.78	95.22	89.65	98.56	89.82	89.30	96.35
$\Delta$	<b>+1.01</b>	<b>+0.33</b>	<b>+0.16</b>	<b>+0.16</b>	-7.74	<b>+1.98</b>	<b>+0.18</b>	<b>+16.21</b>	<b>+2.13</b>

Supplementary : HD (mm)  $\downarrow$  comparison across 18 datasets.

Model	VISCERAL GC	VISCERAL GC-Extra	VISCERAL SC	KITS	LiTS	BTCV- Abdomen	BTCV- Cervix	CHAOS	CT-ORG
TotalSeg	19.68	28.81	30.12	23.38	4.46	17.54	83.20	26.31	9.05
CADS	19.25	17.73	29.65	19.54	4.05	14.43	40.99	24.70	9.29
$\Delta$	<b>-0.43</b>	<b>-11.09</b>	<b>-0.47</b>	<b>-3.85</b>	<b>-0.41</b>	<b>-3.10</b>	<b>-42.21</b>	<b>-1.61</b>	+0.24
Model	AbdomenCT- 1K	VerSe	Learn2reg	SLIVER07	EMPIRE10	Total- Segmentator	AMOS	HaN-Seg	SAROS
TotalSeg	17.73	5.10	4.99	26.64	2.23	4.87	22.00	32.89	4.97
CADS	16.00	5.44	4.87	25.20	8.89	3.21	16.06	18.71	3.00
$\Delta$	<b>-1.73</b>	+0.33	<b>-0.12</b>	<b>-1.44</b>	+6.66	<b>-1.65</b>	<b>-5.94</b>	<b>-14.18</b>	<b>-1.96</b>

Supplementary Table A.7: Quantitative comparison of segmentation performance between CADS-model and TotalSegmentator evaluated on 18 diverse test datasets. Green values in difference ( $\Delta$ ) row indicate CADS-model outperforms baseline.



Category		Primary Test (Compl. Annot.)		Secondary Test (Part. Annot.)		Full Test Data	
		NSD (%) $\uparrow$	HD (mm) $\downarrow$	NSD (%) $\uparrow$	HD (mm) $\downarrow$	NSD (%) $\uparrow$	HD (mm) $\downarrow$
Mutual Targets (119 struct.)	TotalSeg	94.68	15.87	88.20	18.85	93.35	18.03
	CADS	97.75	10.39	90.74	14.82	96.41	12.00
	$\Delta$	<b>+3.07</b>	<b>-5.48</b>	<b>+2.54</b>	<b>-4.03</b>	<b>+3.06</b>	<b>-6.03</b>
All Targets (167 struct.)	CADS	95.30	13.62	89.57	16.73	94.25	14.61

Supplementary Table A.8: **Comparison of HD and normalized surface dice across different test cohorts.** Green values in difference ( $\Delta$ ) row indicate CADS-model outperforms baseline.

Supplementary : Comparison of Dice results (%)  $\uparrow$ .

Model	Brainstem	Eye L	Eye R	Larynx	Optic nerve L	Optic nerve R	Parotid gland L	Parotid gland R	Submandibular gland L	Submandibular gland R
TotalSeg	60.11	90.90	90.90	36.44	61.21	62.51	62.99	63.56	81.22	84.72
CADS	83.19	91.82	92.16	80.24	66.60	67.46	82.39	84.58	85.53	84.11
$\Delta$	<b>+23.08</b>	<b>+0.92</b>	<b>+1.26</b>	<b>+43.80</b>	<b>+5.39</b>	<b>+4.95</b>	<b>+19.40</b>	<b>+21.02</b>	<b>+4.31</b>	-0.61
Model	Aorta	Urinary bladder	Brain	Esophagus	Humerus L	Humerus R	Kidney L	Kidney R	Liver	Lung L
TotalSeg	89.55	90.54	96.39	85.21	95.44	95.16	90.06	90.91	96.45	97.09
CADS	89.74	89.94	96.52	83.20	95.46	95.17	90.09	90.66	96.51	96.70
$\Delta$	<b>+0.19</b>	-0.60	<b>+0.13</b>	-2.01	<b>+0.02</b>	<b>+0.01</b>	<b>+0.03</b>	-0.25	<b>+0.06</b>	-0.39
Model	Lung R	Prostate	Spinal cord	Spleen	Stomach	Thyroid	Trachea	Inferior vena cava	Heart	Optic chiasm
TotalSeg	97.23	72.48	88.66	90.36	88.76	82.37	73.89	71.14	77.93	-
CADS	96.93	75.69	90.08	90.17	87.87	79.40	70.43	65.87	81.22	<b>30.49</b>
$\Delta$	-0.30	<b>+3.21</b>	<b>+1.42</b>	-0.19	-0.89	-2.97	-3.46	-5.27	<b>+3.29</b>	-
Model	Glottis	Lacrimal gland L	Lacrimal gland R	Mandible	Oral cavity	Pituitary gland	Rectum	Seminal vesicle		
TotalSeg	-	-	-	-	-	-	-	-		
CADS	<b>37.11</b>	<b>60.03</b>	<b>52.78</b>	<b>88.81</b>	<b>83.60</b>	<b>58.02</b>	<b>71.71</b>	<b>82.12</b>		
$\Delta$	-	-	-	-	-	-	-	-		

Supplementary : Comparison of HD95 results (mm)  $\downarrow$ .

Model	Brainstem	Eye L	Eye R	Larynx	Optic nerve L	Optic nerve R	Parotid gland L	Parotid gland R	Submandibular gland L	Submandibular gland R
TotalSeg	32.52	1.50	1.50	10.61	4.97	5.41	10.63	10.45	3.00	2.12
CADS	4.50	1.50	1.50	4.50	2.12	2.12	3.67	3.35	2.12	2.60
$\Delta$	<b>-28.02</b>	0.00	0.00	<b>-6.11</b>	<b>-2.85</b>	<b>-3.29</b>	<b>-6.96</b>	<b>-7.09</b>	<b>-0.88</b>	+0.48
Model	Aorta	Urinary bladder	Brain	Esophagus	Humerus L	Humerus R	Kidney L	Kidney R	Liver	Lung L
TotalSeg	2.12	3.67	2.60	2.12	1.50	2.12	11.22	10.35	4.24	2.12
CADS	2.12	4.24	2.60	2.12	1.50	1.50	11.38	10.61	3.67	2.12
$\Delta$	0.00	+0.57	0.00	0.00	0.00	<b>-0.62</b>	+0.16	+0.26	<b>-0.57</b>	0.00
Model	Lung R	Prostate	Spinal cord	Spleen	Stomach	Thyroid	Trachea	Inferior vena cava	Heart	Optic chiasm
TotalSeg	2.12	8.08	1.50	6.00	6.71	2.60	4.50	11.72	23.14	-
CADS	2.12	7.50	1.50	6.00	6.87	3.00	4.74	13.75	25.46	<b>7.65</b>
$\Delta$	0.00	<b>-0.58</b>	0.00	0.00	+0.17	+0.40	+0.24	+2.03	+2.32	-
Model	Glottis	Lacrimal gland L	Lacrimal gland R	Mandible	Oral cavity	Pituitary gland	Rectum	Seminal vesicle		
TotalSeg	-	-	-	-	-	-	-	-		
CADS	<b>10.66</b>	<b>3.00</b>	<b>3.00</b>	<b>1.50</b>	<b>7.79</b>	<b>3.00</b>	<b>23.38</b>	<b>3.00</b>		
$\Delta$	-	-	-	-	-	-	-	-		

Supplementary Table A.9: **Performance comparison between CADS and TotalSegmentator on real-world hospital data.** Evaluation using Dice and HD95 across 35 anatomical structures from 2864 patients with various pathologies. Empty TotalSeg entries indicate structures uniquely segmented by CADS-model. Green values indicate CADS-model improvements over baseline ( $\Delta$  row) and unique anatomical targets (CADS-model row).

Supplementary : Comparison of HD results (mm) ↓.

Model	Brainstem	Eye L	Eye R	Larynx	Optic nerve L	Optic nerve R	Parotid gland L	Parotid gland R	Submandibular gland L	Submandibular gland R
TotalSeg	41.38	6.36	6.54	15.73	11.81	12.73	16.67	16.19	6.18	4.97
CADS	8.08	3.00	3.00	9.49	5.61	5.61	9.00	8.75	4.50	4.97
△	<b>-33.30</b>	<b>-3.36</b>	<b>-3.54</b>	<b>-6.25</b>	<b>-6.20</b>	<b>-7.12</b>	<b>-7.67</b>	<b>-7.44</b>	<b>-1.68</b>	0.00
Model	Aorta	Urinary bladder	Brain	Esophagus	Humerus L	Humerus R	Kidney L	Kidney R	Liver	Lung L
TotalSeg	4.50	9.25	11.32	7.65	8.75	9.49	19.21	18.61	24.00	16.77
CADS	4.50	9.60	13.16	8.49	8.87	8.75	19.21	18.79	22.92	19.61
△	0.00	+0.36	+1.84	+0.84	+0.13	<b>-0.74</b>	0.00	+0.18	<b>-1.08</b>	+2.84
Model	Lung R	Prostate	Spinal cord	Spleen	Stomach	Thyroid	Trachea	Inferior vena cava	Heart	Optic chiasm
TotalSeg	19.61	13.79	5.41	20.12	25.05	7.50	12.09	34.53	39.26	-
CADS	22.95	12.41	6.71	19.73	24.00	8.08	12.99	34.57	34.39	<b>10.92</b>
△	+3.33	<b>-1.37</b>	+1.30	<b>-0.40</b>	<b>-1.06</b>	+0.58	+0.90	+0.03	<b>-4.87</b>	-
Model	Glottis	Lacrimal gland L	Lacrimal gland R	Mandible	Oral cavity	Pituitary gland	Rectum	Seminal vesicle		
TotalSeg	-	-	-	-	-	-	-	-		
CADS	<b>14.85</b>	<b>4.50</b>	<b>4.50</b>	<b>8.08</b>	<b>14.15</b>	<b>4.24</b>	<b>35.15</b>	<b>6.62</b>		
△	-	-	-	-	-	-	-	-		

Supplementary : Comparison of NSD results (%) ↑.

Model	Brainstem	Eye L	Eye R	Larynx	Optic nerve L	Optic nerve R	Parotid gland L	Parotid gland R	Submandibular gland L	Submandibular gland R
TotalSeg	49.32	98.08	97.83	25.32	90.52	90.00	62.02	63.97	95.32	98.14
CADS	88.19	100.00	100.00	85.88	98.01	98.02	91.14	93.96	98.62	98.06
△	<b>+38.87</b>	<b>+1.92</b>	<b>+2.17</b>	<b>+60.56</b>	<b>+7.49</b>	<b>+8.02</b>	<b>+29.12</b>	<b>+29.99</b>	<b>+3.30</b>	-0.08
Model	Aorta	Urinary bladder	Brain	Esophagus	Humerus L	Humerus R	Kidney L	Kidney R	Liver	Lung L
TotalSeg	99.50	91.67	97.09	97.80	99.89	98.92	88.24	89.49	94.11	97.90
CADS	99.20	90.27	96.86	97.11	99.61	99.33	88.71	89.32	94.43	97.14
△	-0.30	-1.40	-0.23	-0.69	-0.28	<b>+0.41</b>	<b>+0.47</b>	-0.17	<b>+0.32</b>	-0.76
Model	Lung R	Prostate	Spinal cord	Spleen	Stomach	Thyroid	Trachea	Inferior vena cava	Heart	Optic chiasm
TotalSeg	97.12	64.57	99.54	81.20	85.07	97.05	89.31	81.24	49.40	-
CADS	96.79	73.37	98.59	81.33	84.26	95.66	86.40	75.77	69.69	<b>74.38</b>
△	-0.33	<b>+8.80</b>	-0.95	<b>+0.13</b>	-0.81	-1.39	-2.91	-5.47	<b>+20.29</b>	-
Model	Glottis	Lacrimal gland L	Lacrimal gland R	Mandible	Oral cavity	Pituitary gland	Rectum	Seminal vesicle		
TotalSeg	-	-	-	-	-	-	-	-		
CADS	<b>62.12</b>	<b>98.02</b>	<b>97.72</b>	<b>98.88</b>	<b>74.05</b>	<b>97.90</b>	<b>68.35</b>	<b>95.54</b>		
△	-	-	-	-	-	-	-	-		

Supplementary Table A.10: **Performance comparison between CADS and TotalSegmentator on real-world hospital data.** Evaluation using HD and normalized surface dice across 35 anatomical structures from 2864 patients with various pathologies. Empty TotalSeg entries indicate structures uniquely segmented by CADS-model. Green values indicate CADS-model improvements over baseline (△ row) and unique anatomical targets (CADS-model row).

Supplementary : Comparison of TPR results (%)  $\uparrow$ .

Model	Brainstem	Eye L	Eye R	Larynx	Optic nerve L	Optic nerve R	Parotid gland L	Parotid gland R	Submandibular gland L	Submandibular gland R
TotalSeg	93.05	95.46	95.16	22.80	46.59	48.07	47.19	47.57	70.74	77.41
CADS	76.61	94.57	94.66	85.13	66.74	67.36	85.11	85.27	83.59	79.89
$\Delta$	-16.44	-0.89	-0.50	<b>+62.33</b>	<b>+20.15</b>	<b>+19.29</b>	<b>+37.92</b>	<b>+37.70</b>	<b>+12.85</b>	<b>+2.48</b>
Model	Aorta	Urinary bladder	Brain	Esophagus	Humerus L	Humerus R	Kidney L	Kidney R	Liver	Lung L
TotalSeg	97.08	96.28	93.61	84.21	97.15	97.48	83.73	85.40	95.89	96.06
CADS	94.40	96.14	93.94	80.75	93.95	94.43	84.31	84.84	96.19	95.20
$\Delta$	-2.68	-0.14	<b>+0.33</b>	-3.46	-3.20	-3.05	<b>+0.58</b>	-0.56	<b>+0.30</b>	-0.86
Model	Lung R	Prostate	Spinal cord	Spleen	Stomach	Thyroid	Trachea	Inferior vena cava	Heart	Optic chiasm
TotalSeg	96.37	68.67	90.10	87.33	88.60	81.64	60.59	61.98	69.89	-
CADS	95.60	73.43	91.87	86.99	88.24	79.42	55.75	59.29	69.46	<b>21.88</b>
$\Delta$	-0.77	<b>+4.76</b>	<b>+1.77</b>	-0.34	-0.36	-2.22	-4.84	-2.69	-0.43	-
Model	Glottis	Lacrimal gland L	Lacrimal gland R	Mandible	Oral cavity	Pituitary gland	Rectum	Seminal vesicle		
TotalSeg	-	-	-	-	-	-	-	-		
CADS	<b>26.65</b>	<b>56.78</b>	<b>49.30</b>	<b>88.34</b>	<b>82.50</b>	<b>46.95</b>	<b>58.53</b>	<b>79.97</b>		
$\Delta$	-	-	-	-	-	-	-	-		

Supplementary : Comparison of error volume results (%)  $\downarrow$ .

Model	Brainstem	Eye L	Eye R	Larynx	Optic nerve L	Optic nerve R	Parotid gland L	Parotid gland R	Submandibular gland L	Submandibular gland R
TotalSeg	107.37	7.92	7.29	-74.88	-47.31	-45.98	-50.75	-51.31	-25.61	-17.76
CADS	-16.19	4.46	3.52	12.19	-4.43	-4.28	0.36	-1.60	-5.54	-11.64
$\Delta$	<b>-91.18</b>	<b>-3.46</b>	<b>-3.77</b>	<b>-62.69</b>	<b>-42.88</b>	<b>-41.70</b>	<b>-50.39</b>	<b>-49.71</b>	<b>-20.07</b>	<b>-6.12</b>
Model	Aorta	Urinary bladder	Brain	Esophagus	Humerus L	Humerus R	Kidney L	Kidney R	Liver	Lung L
TotalSeg	16.81	10.31	-6.08	-3.21	3.90	4.74	-14.45	-12.81	-1.30	-2.67
CADS	9.08	10.70	-5.51	-7.53	-2.04	-1.72	-14.02	-13.42	-1.14	-3.73
$\Delta$	<b>-7.73</b>	+0.39	<b>-0.57</b>	+4.32	<b>-1.86</b>	<b>-3.02</b>	<b>-0.43</b>	+0.61	<b>-0.16</b>	+1.06
Model	Lung R	Prostate	Spinal cord	Spleen	Stomach	Thyroid	Trachea	Inferior vena cava	Heart	Optic chiasm
TotalSeg	-2.26	-23.73	-4.16	9.37	-4.50	-3.56	-35.83	-25.77	-21.71	-
CADS	-3.09	-16.52	3.16	11.26	-4.56	-3.46	-41.76	-19.97	-28.89	<b>52.30</b>
$\Delta$	+0.83	<b>-7.21</b>	<b>-1.00</b>	+1.89	+0.06	<b>-0.10</b>	+5.93	<b>-5.80</b>	+7.18	-
Model	Glottis	Lacrimal gland L	Lacrimal gland R	Mandible	Oral cavity	Pituitary gland	Rectum	Seminal vesicle		
TotalSeg	-	-	-	-	-	-	-	-		
CADS	<b>60.27</b>	<b>11.48</b>	<b>14.36</b>	<b>2.93</b>	<b>4.34</b>	<b>31.75</b>	<b>37.90</b>	<b>11.98</b>		
$\Delta$	-	-	-	-	-	-	-	-		

Supplementary Table A.11: **Performance comparison between CADS and TotalSegmentator on real-world hospital data.** Evaluation using TPR and error volume across 35 anatomical structures from 2864 patients with various pathologies. Empty TotalSeg entries indicate structures uniquely segmented by CADS-model. Green values indicate CADS-model improvements over baseline ( $\Delta$  row) and unique anatomical targets (CADS-model row).  $\Delta$  in error volume table represents the difference between absolute values of two scores ( $|\text{CADS}| - |\text{TotalSeg}|$ ).